Università di Pisa

Dipartimento di Fisica

Corso di Laurea Magistrale in Fisica

Diamond detectors for proton Time of Flight in CT-PPS and TOTEM experiments

Tesi Magistrale

CERN-THESIS-2017-487
26/06/2017

Candidato
Tommaso Isidori

Relatore
Nicola Turini
Simone Donati

Anno Accademico 2017/2018

"Nothing is more important than education: The teaching of one virtuous person can influence many."

Jigorō Kanō

Acknowledgements

I would really like to thank my supervisor Nicola Turini who allowed me to work at these beautiful projects and always supported me, giving me the possibility to pursue my passion. I'm extremely grateful to him for the great experience I got at CERN Institute during my bachelor and master thesis work. Thanks also to Simone Donati, who really kindly accepted to help me with this report.

I would like to thank all the TOTEM and CT-PPS groups which created the perfected environment for me to grow as a student and learn as much as possible during my stay at CERN. I've been amazed by the trust and responsibilities the whole group gave me during the measurements and the installation of the detectors in the LHC.

Special thanks go to the people I closely worked with: Edoardo Bossini, Marco Bozzo, Mirko Berretti, Nicola Minafra and Lorenzo Pagliai. I'm really grateful for all yours suggestions, help, corrections, shouts, blaming and laughters. Without your help I wouldn't have lived the same great experience I had. Thanks to Mario Macrí, Frizzi (Frigyes Janos Nemes) and Valentina Avati for the coffee breaks: just another excuse to talk and ask you for some help and suggestions.

Thanks to all the beutiful people I met during this year, who became great friends. Thanks to Elena Graverini, Luca Gardi, Matteo Lupi, Andres Sanchez, Lorenzo Paolozzi, Michela Semeraro, Giulio Grossi, Enrico Gamberini, Mattia Barbanera, Jacopo Pinzino, Matthias Bonora, Elisa Busetto, Emanuele Ripiccini and Elisabetta Manca who introduced me to them. Thanks for all the great moments and all the support you gave me. Thanks to Mattia and Paolo who came to visit me in Geneva and always welcomed me back in Siena. Thanks to Davide De Nisi who worked hard to correct my English and allowed this thesis to be clearer and more readable. I'd like to give a special thanks to everyone who gave me a bed to sleep on: Jacopo, Matteo and Andres, Elena, Luca and Nicola. You're always welcome

to visit any time. Thanks to all my friends from the University of Pisa and especially thanks to Giacomo Scanavini, who shared with me his infinite optimism and great knowledge.

Last but not least I'd like to thank my whole family. You allowed me to follow my dreams, you supported me during my whole life and you always helped me. I love you all and I'll always do, anywhere my studies may bring me.

Contents

List of Figures iii

List of Tables x

Abbreviations xi

Introduction 1

1 The TOTEM and CT-PPS Experiments at LHC 3
- 1.1 The Large Hadron Collider . . . 4
  - 1.1.1 The transport matrix . . . 6
  - 1.1.2 The pile-up effect . . . 7
- 1.2 Diffractive physics . . . 8
- 1.3 The TOTEM experiment . . . 9
  - 1.3.1 Experimental apparatus . . . 10
- 1.4 CMS and TOTEM: two possible physics scenarios . . . 11
- 1.5 TOTEM upgrade: high-β^* runs . . . 13
- 1.6 The CMS-TOTEM Proton Precision Spectrometer . . . 15
  - 1.6.1 Timing detectors . . . 17
  - 1.6.2 Tracking detectors . . . 20
  - 1.6.3 A new physic's scenario: low-β^* runs . . . 22
    - 1.6.3.1 The LHC as a photons collider . . . 23
    - 1.6.3.2 QCD tests . . . 26

2 Characterization of a Diamond detector 28
- 2.1 Synthetic diamonds . . . 29
  - 2.1.1 Metalization . . . 32
- 2.2 Particle detection . . . 34
  - 2.2.1 Interaction of charged particles with matter . . . 35
  - 2.2.2 IV Curves . . . 37
  - 2.2.3 Charge collection . . . 38
  - 2.2.4 The Shockley-Ramo theorem . . . 39
- 2.3 Read out a diamond detector . . . 42
  - 2.3.1 Broadband amplifier . . . 42

2.3.2 Charge sensitive amplifier . . . 44
2.3.3 High input impedance . . . 46
2.4 Timing measurement . . . 48
2.4.1 Sampling the signals . . . 49
2.4.1.1 Constant fraction discriminator . . . 51
2.4.2 Collecting data with a TDC . . . 52
2.4.2.1 Time over threshold correction . . . 53

3 Front-End electronics for CT-PPS detectors 56
3.1 The electronic boards . . . 56
3.1.1 Hybrid boards for the diamonds . . . 59
3.1.2 Hybrid boards for the Ultra Fast Silicon Detectors . . . 60
3.2 The detector packages . . . 60
3.3 The NINO boards . . . 63

4 Tests on Diamond TOF detectors 66
4.1 The Test beam area . . . 66
4.2 Tests with an oscilloscope . . . 69
4.2.1 Noise and signals oscillations . . . 70
4.3 Tests with the CAEN TDC . . . 72
4.3.1 Threshold characterization . . . 75
4.4 The installation inside IP5 . . . 75
4.5 Tests after LHC . . . 77
4.5.1 Discharges effects . . . 78
4.5.2 Noise measurement . . . 83

5 Double layer diamond detectors 84
5.1 The prototypes . . . 85
5.2 Test beam at the North Area . . . 87
5.2.1 Set-up . . . 87
5.2.2 Measurement and results . . . 88

6 Radiation damage on diamond detectors 92
6.1 IRRAD facility at CERN . . . 93
6.2 Test at IRRAD . . . 94
6.2.1 Acquisition of the currents . . . 96
6.3 Test with a pion beam . . . 98
6.4 Test with a β^- source . . . 100

List of Figures

1.1 Scheme of LHC acceleration lines [3]. 4
1.2 On the left a representation of the diffraction processes, where the carriers result to be Pomerons [25]. On the right the QCD translation of the Pomeron into a two gluons exchange. The gluons have to be at least two, to guarantee the interaction to be colorless [11]. . 9
1.3 TOTEM experimental apparatus [11]. The RP are 220 m further in the forward zone and therefore they are not visible. 10
1.4 Pseudorapidity acceptance for the CMS and TOTEM experiments [13]. On the left some examples of ϕ distribution for diffractive events, plotted with respect to η. 11
1.5 Feynman diagram of a CD interaction between two protons. 12
1.6 Sketch of the TOTEM timing apparatus [49]. The protons' time arrival differences in the two arms are used to reconstruct the z-coordinates of the interaction vertices. 14
1.7 Layout of the CT-PPS apparatus after the first LHC long shutdown [13]. 15
1.8 Projects for the new CT-PPS cylindrical roman pots[13, 49]. 16
1.9 Horizontal distance of the tracking and timing detectors from the beam center [13]. The values are calculated for an approach of 15 σ_{beam}(x) and 20 σ_{beam}(x) of the Roman Pots and a simulated crossing angle of 142.5 μrad. 16
1.10 Simulated particle distribution for fixed values of $|t|$ and ξ, propagated to the CT-PPS detectors location [13]. The solid (dashed) lines represent the $15\sigma_{beam}(20\sigma_{beam})$ boundaries. 17
1.11 In the top row: plots of the CT-PPS acceptance with respect to the value of the mass generated in the central zone of CMS [13]. In the bottom row: resolution of the reconstructed masses produced in the entire spectrum in the CT-PPS acceptance.The plots were drawn studying two different CD events: a di-jet production and a WW production in the central zone. 18
1.12 Comparison between the occupancies of the TOTEM and the CT-PPS experiment [13]. On the left: the CT-PPS's horizontal timing detectors are displayed. On the right: TOTEM's timing detectors' occupancy in the vertical Pot. 19

1.13 On the left: Efficiency as a function of the position (reconstructed with the DESY DATURA Silicon tracker[15]) measured on two adjacent diamond strips. On the right: particle detection efficiency for one diamond sensor; the statistical error on each bin is 5 - 10%. 19
1.14 Time precision plotted with respect to the pixel capacitance[15] . . 19
1.15 Sketch of a LGAD sensor [13]. 20
1.16 Plot of the UFSD's resolution measured during the Test beam sessions at the CERN North Area [17]. The resolution shown in the bottom was measured acquiring the difference of the arrival time measured by an MCP (whose performance are described later, on this thesis 4.1.) and by a 2.2mm^2 UFSD pixel biased at 180V . . . 21
1.17 Simulated proton fluence in one of the CT-PPS tracking stations, with an integrated luminosity of 100 fb^{-1} [13]. 21
1.18 Sketch of a Silicon 3D detector [13, 55]. 22
1.19 The Feynman diagram for the WW production via the two photons' exchange is displayed on the left. On the right: diagrams contributing to the scattering amplitude, at the lowest order perturbation series with a coupling e^2 [32]. 24
1.20 Diagram of exclusive di-photon productions with intact protons in the final state predicted by the SM [13, 26]. 25
1.21 Integrated cross section as a function of the di-photon mass. The plot shows the various contributions to the coupling loop. W bosons, quarks and lepton loops (and their interference) have to be considered to reconstruct the cross section predicted by the SM [40]. . . . 25
1.22 Feynman diagram for an exclusive di-jet production. 26
1.23 Di-jet production recorded during a low pile-up (90 β^*) and $\sqrt{s}$ = 8 TeV by the CMS-TOTEM conjunct apparatus [11]. 27

2.1 Representation of the band gaps in the three different configurations. The forbidden band is the energy distance between the two bands. 29
2.2 Some examples of defects on the metalization layers. In the bottom right a picture of the set-up used in the sensors' electrodes quality check. 34
2.3 Energy loss as function of $\beta\gamma$ for different materials [50]. 36
2.4 On the top left a of the shielded box used during the acquisitions [36]; on the bottom a sectional drawing of the plastic frame. A detail of the spring probe can be found in the top right image. . . . 38
2.5 The picture shows a 5-strips diamond detector's leakage currents, as a function of the Voltages (bottom left) and Time (top left). On the right the measurement with a Sr^{90} are reported. 39
2.6 Representation of the particle passing trough the diamond detector [49]. The passive components are needed to apply the bias to polarize the sensor. 40

2.7 Current induced by the passage of a MIP through 500 μm of diamond. The plot is produced using Weightfield2 simulation software [30]. 41
2.8 Simulation of the SNR response as a function of the detector capacitance, using a broadband amplifier (with input impedance R_i = 50 Ω) to read a diamond sensor [49]. With the capacitance of the diamonds actually used, the SNR results to be below 1. 44
2.9 Schematic of a charge-sensitive amplifier. 44
2.10 Schematic of a charge-sensitive amplifier with our detector plugged (drawn as the parallel between the capacitor C_d and a current generator). 45
2.11 A resistor is added to the charge sensitive amplifier feedback, to discharge the capacitor more rapidly. On the left, a simulation of the response is shown [49]. 46
2.12 Scheme of the pre-amplifier designed by the CT-PPS and TOTEM experiment. In the sketch on the bottom, a simple π model is used to explain the transistor's functioning [49]. 47
2.13 The picture shows the trend of the time precision and SNR with respect to the input impedance. The plots have been drawn for several values of the detector capacitance [49]. 48
2.14 Image of a **Agilent DSO9254A**, the same oscilloscope used during all the tests performed during this work [2]. 50
2.15 Example of time walk effect for two gaussian pulses [59]. 51
2.16 Zero crossing obtained after implementing the CFD [39]. 52
2.17 The picture shows the phases the signals have to go through before being sent to a TDC. Once a threshold (Red line) is set, the discriminator produces a logic pulse (in Blue) whose leading and trailing edges activate the TDC response (Green square curves). . . 53
2.18 Time over threshold (Red line) for a gaussian pulse. 54
2.19 The curves shows two possible corrections for the time walk, using a time over threshold algorithm [49]. 55

3.1 Detail of the board, zoomed on the detector and pre-amplifier zone. On the right the schematic is provided [15]. 57
3.2 On the left: the position of one of the twelve Avago ABA-53563 is highlighted in red. On the right: the schematic of the second stage of amplification [15]. 58
3.3 In the picture the Shaper's position on the board and its schematic are shown [15]. 58
3.4 Comparison between TOTEM and CT-PPS bias voltage pads' geometry. The TOTEM board, on the left, has a single pad which covers the full detector zone. It can house up to 8 diamonds distributed on two columns. The CT-PPS configuration, on the right, is designed to have four $\sim$ 2.5 mm^2 pads in a single column. 59
3.5 Metalization pattern for the TOTEM and CT-PPS experiments. . . 60

3.6 The 15-pads UFSD timing detector glued on one of the TOTEM hybrid boards [22] and bonded with standard 25 μm wires. On the left a scheme of the pixels' size is provided. 61
3.7 Three different sketches of the 4-layers structure developed to arrange the hybrid boards inside the roman pots. In the central picture, the detectors are stored inside the aluminum "champignon" [13]. 61
3.8 Picture of the feedthrough board. 62
3.9 Schematic of the NINO ASIC. On the bottom: the discriminated signals, after being processed by the intrinsic Time over threshold correction and the pulse stretcher [26]. 63
3.10 The schematic block represents the circuit developed to operate the NINO with single-ended voltage signals [26]. The A1 component is the attenuator. 64
3.11 Characterization of the NINO pulse stretcher response. 65

4.1 The CERN north area exploits the 350 GeV/c protons extracted from the SPS accelerator making them collide in four different target, in order to produce secondary particles to be sent to the test beam area and to experiments situated in CERN Prevessin experimental area [1]. 67
4.2 Simulated spectrum of particle production on the T4 target [1]. Production rates are normalized per proton on target (pot) and the momentum acceptance is taken to be $\Delta p/p = 2\%$. 68
4.3 On the left: roman pot structure at the North area. On the top and bottom right: a detector package is install to be tested with the cooling and vacuum systems on. 68
4.4 Mounting the external support on one of the H8C table. On the right: diamonds alignment on the beam line. 69
4.5 Performance of a diamond timing detector (0.3 pF). In the top row the pulse height and rise time distribution are shown: the mean values are compatible with the expected one. The time precision (in the bottom) is taken to be the σ of the time arrival distribution, measured between two identical detectors: $\sigma_{t1} = \sqrt{\sigma_{tot}^2 - \sigma_{t2}^2} \approx 91$ ps. 70
4.6 The graph shows the trend of the noise v_{RMS} for the old and new generation of boards. From the error bars of the first and last channels, we can observe that these are generally the most problematic ones. 71
4.7 In the picture: the three ideas implemented to remove the oscillations from the diamonds' signals. 72
4.8 Electronic chain used during the relative efficiency of diamond detectors, using a CAEN TDC. 73
4.9 Plot of the relative efficiencies of the NINO chips' channels. The blank spots represent the dead channels. 74

4.10 Detail of one of the NINO board. In the bottom left we can observe the four potentiometers, one for each NINO chip. 75
4.11 Plot of the relative efficiencies of the NINO chips' channels. 76
4.12 Installing the packages in the CT-PPS horizontal roman pots, in the 4-5 sector. 77
4.13 The NINO boards of the 5-6 sector fully plugged. 77
4.14 Horizontal roman pots with the detector package installed. The vacuum bellow is plugged in and its valve can be observed in the middle of the picture. 78
4.15 On the left: assemblage of the support. On the right: set-up used during the tests at RD51. 79
4.16 On the left: data obtained with 600V and 25 mbar; the labels show where the X-ray gun were aiming. On the right: plot of the currents read at 650V and 15 mbar, aiming at the HV connector on the board. 80
4.17 On the upper row, on the left the plot the trend of the current studied at 800V and 40 mbar; it is possible to observe the effects of the charging up, generating the bumps and the consequent discharges. On the bottom row, the feedthrough has no time to charge up when we apply 700V and 20 mbar. Respectively on the top and bottom left, the pictures of the feedthrough. 81
4.18 In the picture the HV weak spots found during RD51 tests. In the top figure, the lightning symbols on the feedthrough represent the path of the sparks observed: from the HV pads to the ground's via on the pcb. The picture on the bottom shows two discharge effects: the first on the HV connector, the second in one of the HV pads, just under a diamond sensor. 82
4.19 The boards before the treatment (on the left) present air bubbles beneath the coating surface. On the right, the hybrids are heated to remove all the residual humidity. 82
4.20 Set-up for the noise measurement inside CMS buffer zone. 83
4.21 RMS noise measured on the board extracted from the LHC. 83

5.1 Comparison between a double diamond layer configuration and a thicker sensor. Doubling the sensor's thickness we obtained twice the charge generation by incident particles. However a larger drift zone increases the signal's induction time and consequently rise time. 84
5.2 Sketch of the configuration used in the double layer prototype. The highlighted strips are the ones used during the tests: the highlighted 4-strip (on the top) was chosen to have similar capacitance to the one used in the double diamond. 85
5.3 In the top picture a cross section of the prototype is shown. In the bottom, a sketch of the PCB with the detector's layout. The diamond in blue is the 4-strips sensor used as a comparison. 86

5.4 Left: Sketch of the PCB board with the 4-strip single diamond and the 5-strip double one. The drawing includes the representation of the connections and the actual scale. Right: MCP diamonds board's arrangement in the test beam area. The SPS pion beam, drawn in red, cross the detector such that the particles hit the diamond connected through the via first . This expedient minimizes the collection's delay time. 88
5.5 Channels mapping for the two diamond sensors. 89
5.6 Fourier transforms for the noise of the single (on the left) and double diamond (on the right) configurations, obtained using the Fast Fourier Transform (**FFT**) oscilloscope's feature. 89
5.7 Pulse height comparison: single and double diamond layout. The average values are 0.67 V for the single diamond and 1.03 for the double. 90
5.8 Plot of the time difference measured between the MCP and the double diamond detector. The small non-Gaussian tail at larger ΔT values contains 5% of the events in the plot. 91

6.1 IRRAD and CHARM facilities inside the Cern East Hall. The proton bunches are extracted from the PS and sent through the T8 beam line inside the area [8]. 93
6.2 Preparation of the hybrid before the installation on the moving support in IRRAD Zone 2. On the top right a detail of the board's front side; on the bottom right the picture shows the aluminum dose sensor. 95
6.3 On the left the set-up inside the control room. The power cables (two LV generators and the Keithley used for the HV) and the SMA connectors are plugged in the patch panel. On the right the detector is mounted on the moving support, inside the irradiation area. . . . 96
6.4 The plot shows the trend of the current absorbed from the diamond during the irradiation tests. All the fluences are labeled in the graph. During the whole test, the bias voltage was kept to 500 V. . 97
6.5 Superimposition of the data collected from the diamond (in red) already shown in plot 6.4 and the BPM counts (in black). The IRRAD spill profiles are reconstructed using the derivative of the signal increase (integral) on the central pad of BPM2, units of measurement are therefore arbitrary. The red line helps to highlight the trend of the current absorbed by the diamond, already shown in picture 6.4. 98
6.6 Comparison between the spill profiles acquired during different days. The red line represents the current absorbed by the diamond, the black one the BPM counts. 98
6.7 Pulse height acquired using the H8 pion beam passing through the irradiated board. The two distributions are acquired with different low voltage values. Red : PreAmp = Booster = 2V ; Blue : PreAmp = 2.1 V, Booster = 2.3 V. 99

6.8 Comparison between irradiated and non-irradiated diamond pulse amplitude distributions. Both the data sets were acquired with a bias high voltage of 500V and the same low voltage values. 100
6.9 Pulse height distribution acquired using the Sr^{90} source and the irradiated board. Due to the absence of a trigger system and the reduced SNR, the expected Landau distribution is not visible. . . . 101

List of Tables

1.1 Some of the LHC parameters for the $\sqrt{13}$ TeV running scenario [13]. 13
1.2 First results obtained wit the TOTEM - CT-PPS diamond timing detectors [16]. 20

2.1 Physical properties of silicon and diamond [49, 54]. 30
2.2 The table shows the synthetic diamond classification: the presence of impurities changes the crystal's behavior and aspect. The highlighted row represents the type of diamonds preferred for our applications. 32

4.1 Final mapping for the NINO boards installed in the LHC. The red squares indicates the board's dead channels. 74
4.2 The table lists the information obtained scanning the pressure and voltages values during the tests performed in the CMS buffer zone. Unfortunately, the red box represents a spot in the board with the new coating applied which still presented sparks occurrence 81

5.1 Table of the RMS noise voltage in the single and double layer configurations. 89
5.2 Table of comparison between the values measured in the single and double configuration. 91

6.1 Details for the IRRAD runs. 93
6.2 Results from RD42 tests performed on diamond detectors [18]. A and B are two different samples and are subjected to a different fluence. I_{ind} is the current monitored with a high impedance electrometer. 94

Abbreviations

APD	**A**valanche **P**hoto **D**iodes
AQGC	**A**nomalous **Q**uartic **G**auge **C**oupling
BPM	**B**eam **P**osition **M**onitor
BSM	**B**eyond **S**tandard **M**odel
CCD	**C**harge **C**ollection **D**istance
CCE	**C**harge **C**ollection **E**fficiency
CEP	**C**entral **E**xclusive **P**roduction
CSC	**C**athode **S**trip **C**hambers
CVD	**C**hemical **V**apour **D**eposition
DQC	**D**etector **Q**uality **C**ontrol
DQM	**D**ata **Q**uality **M**onitor
DUT	**D**evice **U**nder **T**est
EHP	**E**lectrons **H**oles **P**airs
FFT	**F**ast **F**ourier **T**ransform
GEM	**G**as **E**lectron **M**ultiplier
IP5	**I**nteraction **P**oint **5**
LGAD	**L**ow **G**ain **A**valanche **D**iode
LHC	**L**arge **H**adron **C**ollider
LVDS	**L**ow **V**oltage **D**ifferential **S**ignals
MCP	**M**ulti **C**hanel **P**late
MET	**M**issing **T**ransverse **E**nergy
MIP	**M**inimum **I**onizing **P**artycle
MPV	**M**ost **P**robable **V**alue
NIM	**N**uclear **I**nstrumentation **M**odule

PCB	**P**rinted **C**ircuit **B**oard
QCD	**Q**uantum **C**hromo**D**ynamic
QED	**Q**uantum **E**lectro**D**ynamic
R&D	**R**esearch **&** **D**evelopment
RMS	**R**oot **M**ean **S**quare
RP	**R**oman **P**ots
scCVD	**s**ingle **c**rystal **C**hemical **V**apour **D**iamonds
SM	**S**tandard **M**odel
SNR	**S**ignal **N**oise **R**atio
TDC	**T**ime to **D**igital **C**onverter
UFSD	**U**ltra **F**ast **S**ilicon **D**etectors

Dedicated to my family

Introduction

This thesis recounts my work during the period 04/16 - 04/17 at the CERN Institute, which involved the study, characterization and installation of diamond timing detectors in the LHC beam line in the TOTEM and CT-PPS experiments to measure the proton time of flight. Their apparatuses extend for ~ 220 m from the IP5, where the CMS experiment is placed. Even though the TOTEM experiment was designed to operate during dedicated LHC runs in a stand-alone configuration, its trigger compatibility with CMS allows their cooperation and data matching. The conjunct apparatus reaches the best *pseudorapidity acceptance* in the LHC. Particularly interesting for new physics scenarios are the studies on Central Diffraction (CD) events, where the two protons, collided in IP5, survive the interaction and scatter at low angles and are detected in the Roman Pots[1] (RP) while, in the central zone, decay products are generated. While the RP reconstruct the momentum loss from the protons scattered in the two arms (proportional to their displacement from their orbits), the CMS experiment reconstructs the mass generated in the central zone. The kinematic of these events is therefore closed and well defined. The central diffractions belong to a branch of physics called *diffractive physics* which, by definition, concerns the study of the interactions where no quantum numbers are exchanged. These events allow us to study important central exclusive production, sensitive to possible new physics such as anomalous quartic gauge couplings, new resonances (with definite J^{PC}), di-jet exclusive production and indirect research for dark matter. The search for such rare events will require to integrate as much luminosity as possible during the next LHC run. However, a high instantaneous luminosity results in a large number of pile-up events. In order to cope with the expected high rate of protons and to be able to discriminate between the primary proton-proton (p-p) vertices and the background, the TOTEM and the CT-PPS experiments decided to equip some of their RP units with radiation-hard timing detectors. The baseline solution have been single crystal diamond sensors: a 4-layers structure of diamond detectors read out by an electronic chain placed on the same board. Their timing information will be used in the reconstruction of the primary p-p interaction vertex, using the time of flight

[1] Vacuum chambers directly installed in the beam line, on both the forward zones of IP5. Inside them, the tracking and timing detectors of the TOTEM and CT-PPS experiments are installed. A stepper motor allows direct approach to the proton beam up to $15\sigma_{beam}$.

equation for the two survived protons tagged in the forward zones:

$$vertex\,position(z) = |t_{RP1} - t_{RP2}|\,c \qquad RP_{distance} = \frac{(t_{RP1} + t_{RP2})\,c}{2}$$

The vertex reconstruction's resolution is therefore proportional to the time precision. The first chapter of this thesis is dedicated to the TOTEM and CT-PPS experiments' description. Their experimental apparatuses are outlined and the reasons that led to a R&D project on the new timing and tracking detectors explained. Only the CT-PPS physics program (on which my work was focused) is treated in detail. The diamond sensors' proprieties and the read-out development will be detailed in chapter two. The Shockley-Ramo theorem will be explained and a brief introduction on the interaction of charged particle with matter will be given. The following sections give a detailed overview of the whole read-out chain, the hybrid boards and the detector packages. One of the sections is dedicated to the description of the Ultra Fast Silicon Detectors prototypes tested in parallel with the diamond ones. The tests done to measure their performance will not be explained in detail but the results obtained can be found in the article *"Test of UFSD Silicon Detectors for the TOTEM Upgrade Project"* we published. The following chapters include an account of my contributions to the Collaboration. My work concerned the tests and optimization of the CT-PPS diamond timing detectors and involved several topics. In chapter 4 I'll describe the diamond detectors' characterization and their installation in the LHC. Starting from their tests with the $\sim$ 180 GeV CERN North Area pion beam, I will describe all the procedures of evaluation of their functioning and performance that led to their installation in beam line. Moreover, a whole section will be dedicated to the study of the detectors once extracted from the LHC. Chapter 5 will describe the measurements performed during the Summer of 2016 test beam on a new technology of timing detectors, which explore the possibility of using two diamond sensors read out by the same amplification chain. This R&D project (funded by the INFN) was presented to the *5th Telescope and Test Beam Workshop* (organized by the IFAE of Barcelona, Spain) and the results obtained can be found in the article we published: *"Timing performance of a double layer diamond detector"*. The last chapter of the Thesis shows the results of the tests performed in Novemeber 2016, when a diamond detector install in a spare TOTEM board was brought to the IRRAD facility, to measure its functionality with high particle rates. After it had collected a fluence of more than 10^{15} n_{eq} and the current absorbed by the diamond was monitored, the detector was then brought to the CERN North Area to be tested on a pure pion beam.

Chapter 1

The TOTEM and CT-PPS Experiments at LHC

In this first chapter I will give an introduction about the TOTEM (**TOT**al and **E**lastic cross section **M**easurement) experiment, its apparatus and its placement in the Large Hadron Collider (**LHC**), the world's largest particle accelerator. I will focus on the collaboration between the TOTEM and CMS (**C**ompact **M**uon **S**olenoid) experiments, which led to the proposal of a new physics program. This Collaboration took advantage of the compatibility of the two experiments' triggers to allow them to cooperate, reaching the best *pseudorapidity* η[1] acceptance value inside the LHC.

The reconstruction of Central Diffraction (**CD**) events using proton tagging is one of the Collaboration's main goal. Using the TOTEM experiment's timing and tracking detectors to reconstruct the momentum loss $\xi_{1,2}$ from the protons that survived the interactions and matching this information with the mass M_X reconstructed by CMS central barrel detectors, would lead to a significant background rejection.

As shown in equation 1.1, CD events are characterized by closed and definite kinematics which also gives a significant advantage in indirect missing transverse energy (**MET**) events reconstructions.

$$M_X = \sqrt{\xi_1 \xi_2 S} \tag{1.1}$$

[1] In particle physics, the *rapidity* of a particle moving along the z-axis with Energy E and momentum p_z, can be written as y = $\frac{1}{2} ln(\frac{E+p_z c}{E-p_z c})$.
The pseudorapidity can be defined as η = - $\ln \tan(\frac{\theta}{2})$, where θ is the angle between the particle trajectory and the z-axis.

Where S is the the energy in the center of mass, $\xi_{1,2}$ the momentum loss reconstructed from the protons in the forward zone and M_X the decay product's mass reconstructed by CMS.

Additionally, the possibility of working during standard LHC runs will be explored, describing the CT-PPS (**C**MS - **T**otem **P**roton **P**recision **S**pectrometer) experiment which is going to install radiation-hard timing and tracking detectors to overcome the problems related to the high interaction rate in Interaction Point 5 (**IP5**).

1.1 The Large Hadron Collider

The Large Hadron Collider is presently the world's largest particle accelerator [27]. It was commissioned by the European Organization for Nuclear Research (CERN) and built near Geneva (CH), using part of the Large Electron Positron collider (**LEP**) tunnel, its predecessor.

The construction works lasted for over ten years (1998 - 2008) and the result is a 27 km long beam line in which the proton bunches, pre-accelerated by a Linear accelerator (**LINAC**) and two smaller synchrotrons (Proton Synchrotron (**PS**) and Super Proton Synchrotron (**SPS**)), reach energies up to 14 TeV. The beams, following the acceleration stages shown in fig. 1.1, collide in 4 different IP. During 2016, the standard high-luminosity run consisted in $\sim$ 2808 proton bunches (with a maximum of 1.5 10^{11} protons per bunch) colliding with a frequency of 40 MHz.

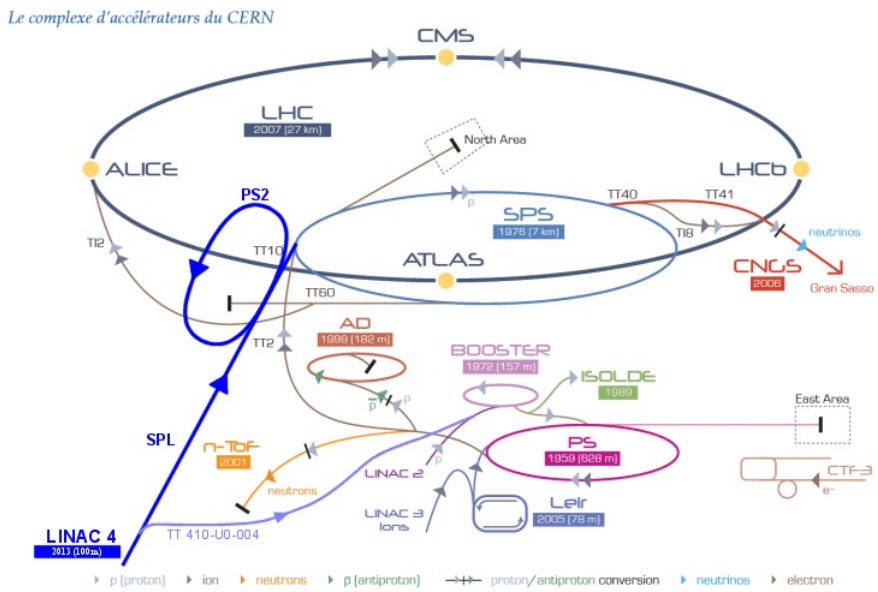

FIGURE 1.1: *Scheme of LHC acceleration lines [3].*

A basic interpretation of the accelerators' luminosity for two head-on bunches can be expressed with the equation:

$$\mathcal{L} = f \cdot \frac{n_1 n_2}{4\pi\sigma_x\sigma_y} \tag{1.2}$$

Where:

- f is the beam revolution frequency inside the accelerator.
- $n_{1,2}$ are the number of particles per bunch.
- $\sigma_{x,y}$ are the Root Mean Square (**RMS**) transverse beam sizes.

Several additional terms have to be added to equation 1.2 in order to obtain a more general formula for $\mathcal{L}$. The number N_b of total bunches accelerated and the *crossing angle* with which they interact have to be taken into account. Equation 1.2 can be rewritten as:

$$\mathcal{L} = f \cdot \frac{n_1 n_2 \, N_b}{4\pi\sigma_x\sigma_y} \, S \tag{1.3}$$

S is a geometrical term called *luminosity reduction factor* and involves the crossing angle of the bunches and their RMS longitudinal dimensions [42].
Finally, equation 1.3 can be recast in terms of *beam emittance* and *amplitude functions*:

$$\mathcal{L} = f \cdot \frac{n_1 n_2 \, N_b}{4\sqrt{\epsilon_x\beta_x^*\epsilon_y\beta_y^*}} \, S \tag{1.4}$$

Where $\epsilon_{x,y}$, the *beam emittance*, measures the average spread of particles' coordinates in position-and-momentum phase-space. Its relation with $\beta^*_{x,y}$, namely the *amplitude function* calculated at the interaction point, follows the formula:

$$\epsilon_{x,y} \equiv \pi \frac{\sigma^2_{x,y}(s)}{\beta_{x,y}} \tag{1.5}$$

The amplitude function β gives the relation, expressed in meters, with the transverse size of the particle beam along the nominal beam trajectory. The actual peak luminosity of the LHC reaches $\mathcal{L} \sim 10^{34}\ cm^{-2}\ s^{-1}$.

After a collision we can define the expected rate of occurrence of a given event as the product between the instantaneous luminosity and the *cross section*, which represents the probability of occurrence of that event:

$$\frac{dN}{dt} = \sigma \cdot \mathcal{L} \tag{1.6}$$

The formula, if integrated over time, gives the total number of expected events. In order to run with high-luminosity, the LHC uses pairs of focusing quadrupoles to shrink the proton beams in proximity of the interaction points, reducing the area of the bunches to ≈ 17 μm radius. This operation leads to a reduction of $\sigma_{x,y}$ and consequently affects the beams' coherence (an hence the $\beta_{x,y}(s)$ function).

1.1.1 The transport matrix

Knowing the magnets' effect on the protons inside the beam line, their transverse position (x*,y*) and angle (θ_x^*,θ_y^*) at the IP location can be reconstructed using the equation:

$$\vec{d} = T \cdot \vec{d^*} \tag{1.7}$$

Where $\vec{d} = (x, \theta_x, y, \theta_y, \xi)^T$ and $\xi = \frac{\Delta P}{P}$ is the fraction longitudinal momentum loss of the protons. T is called *transport matrix* and it depends on the accelerator's parameters. Equation 1.7 becomes:

$$\begin{pmatrix} x \\ \theta_x \\ y \\ \theta_y \\ \xi \end{pmatrix} = \begin{pmatrix} v_x & L_x & 0 & 0 & D_x \\ \frac{dv_x}{ds} & \frac{dL_x}{ds} & 0 & 0 & \frac{D_x}{ds} \\ 0 & 0 & v_y & L_y & D_y \\ 0 & 0 & \frac{dv_y}{ds} & \frac{dL_y}{ds} & \frac{D_y}{ds} \\ 0 & 0 & 0 & 0 & 1 \end{pmatrix} \begin{pmatrix} x^* \\ \theta_x^* \\ y^* \\ \theta_y^* \\ \xi^* \end{pmatrix} \tag{1.8}$$

Where:

- $v_{x,y} = \sqrt{\frac{\beta_{x,y}}{\beta^*}} \cos \Delta\Phi_{x,y}$ is the magnification.
- $L_{x,y} = \sqrt{\beta_{x,y}\beta^*} \sin \Delta\Phi_{x,y}$ is the effective length.
- $\Delta\Phi_{x,y} = \int_{IP}^{RP} \frac{ds}{\beta(s)_{x,y}}$
- $D_{x,y}$ is the Dispersion.

We observe that the elements of the matrix T depend on the amplitude function β which, in turn, depends on the beam emittance ϵ. These two quantities are already described in section 1.1.

Of particular interest is the term ϵ whose value decreases with the increase of the beam's energy.

We can define:

$$\epsilon_n = \beta \, \gamma \, \epsilon \tag{1.9}$$

as the *normalized emittance*, where β and γ are the relativistic functions. ϵ_n does not vary as a function of the beam's energy and is therefore used to measure the intrinsic uncertainty of the protons' direction before the collision. However, when β is close to one, the normalized emittance shows an inverse proportionality to the beam's energy and therefore (using equation 1.5) the bunches' transverse dimensions result to vary inversely to the square root of the energy.

1.1.2 The pile-up effect

The pile-up effect describes the probability of occurrence of more than one proton-proton collision per *bunch crossing*. The number of particle interactions follow the Poisson distribution and can be calculated using the equation:

$$P(\lambda) = \frac{e^{-\mu}\mu^{\lambda}}{\lambda!} \tag{1.10}$$

Whose mean value μ grows in parallel with the machine's luminosity. Their relation follows the equation:

$$\mu = \mathcal{L} \, \tau \, \sigma_{pp} \tag{1.11}$$

Where:

- $\mathcal{L}$ is the instantaneous luminosity of the machine 1.1.
- τ is the time distance between two consecutive bunches.
- σ_{pp} is the proton-proton total cross section.

1.2 Diffractive physics

Hadronic processes are divided into two main categories: soft and hard. The classification is based on their Energy scales: while the soft processes are characterized by energy scales of the order of the hadron radius ($\sim$ 1 fm) and $|t|^2 \sim$ MeV^2 [2], the hard ones are identified by higher energies and $|t| \gtrsim GeV^2$. Diffractive physics studies a branch of the hadronic processes, which includes both the soft and hard type, and concerns the interactions where no quantum number are exchanged.

Its name comes from the similarities between the trend of the hadronic diffraction cross section and the one of the optical phenomenons describing the angular distribution of the light diffracted passing trough an obstacle of radius R. In both cases plots show a pattern of minimums and maximums, with peaks followed by rapid decreases.

In hadronic diffraction reactions the fragmentation of one particle or both can occur. Their *dissociation* generates X_n products in the final states. The possible processes are:

- Single Diffraction (SD) $\quad p_1 + p_2 \longrightarrow p_1' \oplus X$
  Only one proton dissociates while p_1', the *leading* one, just loses a part of his momentum.
- Double Diffraction (DD) $\quad p_1 + p_2 \longrightarrow X_1 \oplus X_2$
  When both protons dissociate.
- Central Diffraction (CD) $\quad p_1 + p_2 \longrightarrow p_1' \oplus X \oplus p_2'$
  Both protons lose part of their momentum, while the final products are generated in the central zone.
- Elastic Scattering $\quad p_1 + p_2 \longrightarrow p_1' + p_2'$

The symbols $\oplus$ indicate the presence of a *Rapidity gap*, hence the presence of a large rapidity range in which the final products are forbidden. It is possible to find Rapidity Gaps even in non-diffractive physics events but their contribution is exponentially suppressed. Equation 1.12 shows the comparison between diffractive (on the left) and non-diffractive (on the right) Rapidity Gaps contributions :

$$\frac{dN}{d\Delta\eta} \sim constant \qquad\qquad \frac{dN}{d\Delta\eta} \sim e^{-\Delta\eta} \tag{1.12}$$

[2] At the the soft processes energy scales, it is not possible to use perturbative QCD theorethical framework.

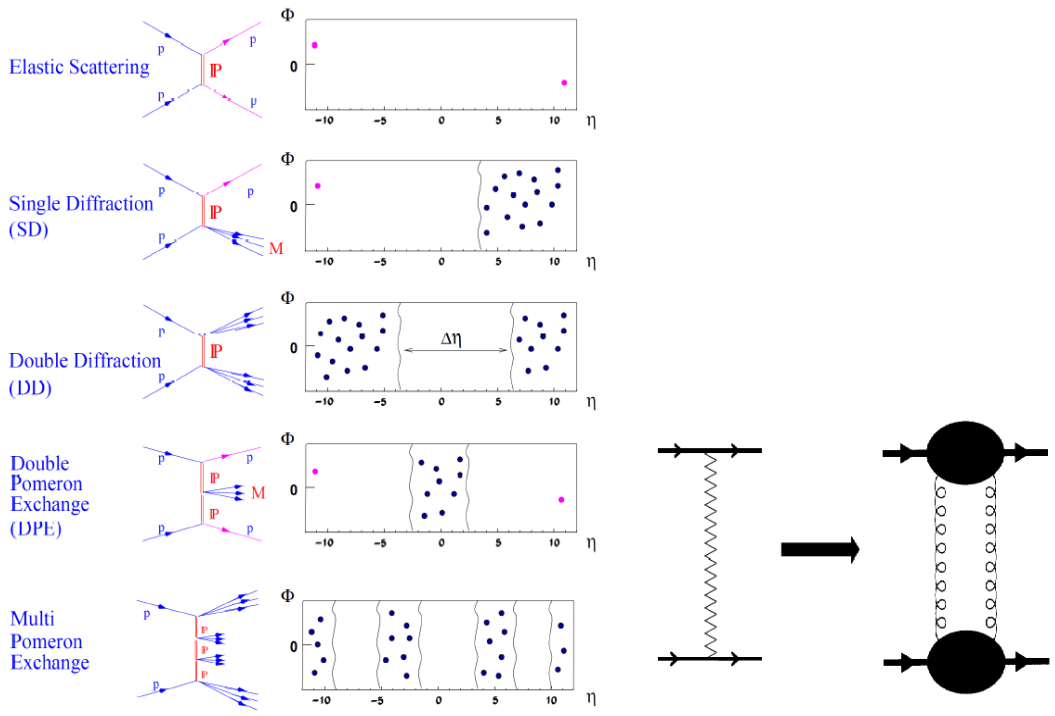

FIGURE 1.2: *On the left a representation of the diffraction processes, where the carriers result to be Pomerons [25]. On the right the QCD translation of the Pomeron into a two gluons exchange. The gluons have to be at least two, to guarantee the interaction to be colorless [11].*

For an interaction to be correctly defined as diffractive, both the presence of Rapidity Gaps and the exchange of no quantum numbers are required. Neither of the two condition is individually sufficient. During the 60's, Tullio Regge proposed a theory which satisfied both the prerequisites with the introduction of the exchange of a universal trajectory with vacuum quantum number called *Pomeron* [35]. In order to describe it in a more modern framework, the Pomeron has been translated into a t-channel two gluon exchange, to fit into the Quantum Chromodynamics (**QCD**) theory.

1.3 The TOTEM experiment

The TOTEM experiment was originally designed to measure the proton-proton total cross section with a precision of 1% - 2%[3], to study the nuclear elastic p-p cross section over a wide range of the squared four-momentum transferred ($10^{-3}GeV^2 < |t| < 10GeV^2$) and perform measurements of diffractive dissociation phenomena [20]. Its program aims to complete and explain the phenomenological

[3]The experiment uses a luminosity-independent method, computing the inelastic and elastic cross sections using the *optical theorem*, to measure the total p-p cross section [20].

models on which the non-perturbative QCD theory is based and give a more precise interpretation of strong hadron interactions in collisions with high energy and low transferred momentum.

1.3.1 Experimental apparatus

The TOTEM experiment is located in IP5, outside the CMS end-caps and its facilities extend for 220 m on both sides of the interaction point. The experimental apparatus, shown in fig. 1.3, consists of two gas detector telescopes called T1 and T2, which study the inelastic processes, and the roman pots (**RP**): vessels containing silicon strips detectors whose job is to detect the protons surviving the interactions and scattered at low angles.

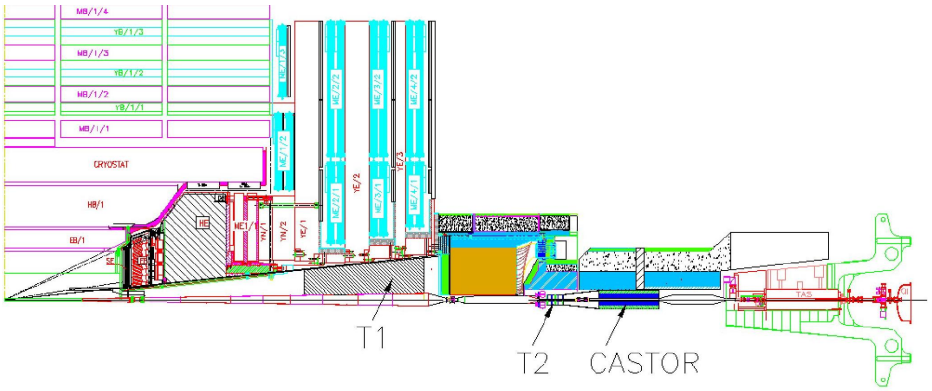

FIGURE 1.3: *TOTEM experimental apparatus [11]. The RP are 220 m further in the forward zone and therefore they are not visible.*

An overview of the apparatus is detailed below:

- **T1**
  T1 is the TOTEM tracker nearest to the interaction point. The telescope houses two groups of five planes of Cathode Strip Chamber (**CSC**) [9] detectors installed around the beam pipe. The T1 tracker with a spatial resolution of 0.8 mm and its tracking acceptance covers a range of pseudorapidity of $3.1 < |\eta| < 4.7$ (similar to the one covered by the CMS end-caps calorimeter).

- **T2**
  T2 [51] is the second tracker of the experiment and consists of two 40 cm long symmetrical supports which house a group of 10 gas electron multiplier (**GEM**) [57] detectors each. Each detector covers an angle of 192° creating an overlapping region of 12° with the one in the opposite support, covering the entire 360° in ϕ. This tracker covers a $5.3 < |\eta| < 6.5$ range of pseudorapidity and provides a fully inclusive trigger, whose function is to

minimize the loss of events in the study of the inelastic cross section, vertex reconstruction and measurement of the forward process topology.

- **Roman pots**
  To detect the protons scattered at very low angles (μrad) but still traveling inside the LHC vacuum beam pipe, tracking detectors are placed inside the Roman pots' (RP) vacuum chambers. The RP are vessels which can be directly inserted into the beam pipe and therefore allow the detectors to approach the particle beam within a working range of 10 - 15 σ_{beam}. The stepper-motor ensures a resolution of 400 steps per tour (1 step = 0.9°) and an accuracy of $\approx \pm 3\%$ [25]. In order to minimize the *material budget* the enclosures are equipped with a 150 μm *thin window*. Its flatness and mechanical deformation characteristics limit the inefficient region to be $\leq$ 50 μm. 10 layers of Silicon strips detectors ensure a tracking resolution of $\sim$ 20 μm. Two RP units 4 meters apart make a *station* and the TOTEM experimental apparatus includes two of them for each arm: one 147 m and one 220 m far from IP5.

1.4 CMS and TOTEM: two possible physics scenarios

TOTEM experiment was not conceived only to work as a stand-alone apparatus and its cooperation with CMS was planned during the experiment's design. Although the two projects are uncorrelated and they study different processes, the compatibility of the two triggers allows for their cooperation during the acquisitions. As shown in fig. 1.4, their data matching ensures the conjunct apparatus to have the best pseudorapidity η acceptance values inside LHC.

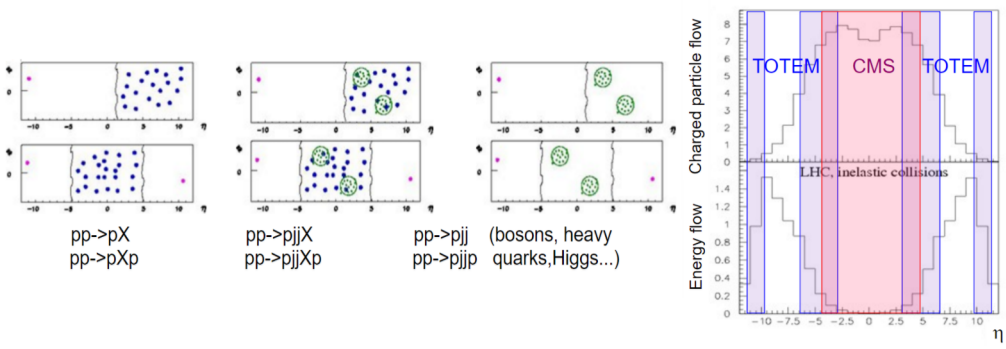

FIGURE 1.4: *Pseudorapidity acceptance for the CMS and TOTEM experiments [13]. On the left some examples of ϕ distribution for diffractive events, plotted with respect to η.*

Of particular interest for the Collaboration are the Central diffraction events, namely when the protons don't dissociate, interacting via photon or colour-singlet gluon exchange to produce a system X in the central region ($p_1 + p_2 \longrightarrow p_1' \oplus X \oplus p_2'$). fig. 1.5 shows the Feynman diagram for a CD event.

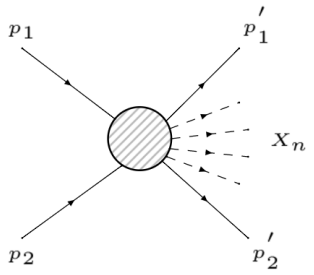

FIGURE 1.5: *Feynman diagram of a CD interaction between two protons.*

Central Exclusive Productions (**CEP**)[4] are characterized by closed and well defined kinematics since they allow the reconstruction of both the interaction (momentum lost from the protons, detected by the Roman Pots) and the production (mass reconstructed by CMS central detectors) vertex.
A simple interpretation is provided by the equation:

$$M_X = \sqrt{\xi_1 \xi_2 S} \tag{1.13}$$

In our apparatus, the mass created in the CD event can be reconstructed using the CMS central barrel. The two surviving protons are detected in the IP5 forward zone by the RP stations placed in the two arms of the TOTEM experiment.

However, the two experiments work with completely different conditions: while the TOTEM stand-alone runs need low luminosity and large beam coherence (high β^*, as explained in section 1.1), CMS needs to work with the LHC high-luminosity optics configuration (low β^*). A description of the LHC parameters for the $\sqrt{13}$ TeV runs is provided in table 1.1.

The table predicts large pile-up values during high-luminosity runs and therefore a large number of interaction vertices produced for each bunch crossing. 10 % of these interactions are expected to be diffractive. Since single diffractions represent the main contribution in this subsample, discriminating between two protons surviving a CD event and two protons belonging to different vertices is not trivial. A detailed study of the p-p induced background has been pursued subtracting

[4]Central diffraction events with exclusive production channels.

β^* [m]	cr. angle [μrad]	ϵ_N [μm rad]	N [10^{11} p/b.]	k [bunches]	μ	Luminosity [$cm^{-2}\ s^{-1}$]	
2500	0	2	0.7 ÷ 1.5	2	0.004 ÷ 0.02	(1.2 ÷ 5.6) 10^{27}	= (0.1 ÷ 0.5) nb^{-1} /24h
90	0	2	0.5 ÷ 1.5	156	0.06 ÷ 0.5	(1.3 ÷ 12)10^{30}	= (0.1 ÷ 1) pb^{-1} /24h
90	100	2	0.5 ÷ 1.5	1000	0.06 ÷ 0.5	(0.9 ÷ 7.7) 10^{31}	= (0.8 ÷ 7) pb^{-1} /24h
0.5	310 ÷ 390	1.9 ÷ 3.75	1.15	2520 ÷ 2760	19 ÷ 34	(0.8 ÷ 1.3)10^{34}	= (0.7 ÷ 1.1) fb^{-1} /24h

TABLE 1.1: *Some of the LHC parameters for the $\sqrt{13}$ TeV running scenario [13].*

a simulated sample of clean events from a *zero-bias*[5] sample of data collected during TOTEM 2012 run ($\sqrt{s}$ = 8 TeV). The process is explained in reference [21]. To cope with this pile-up the Collaboration developed a new project, the CMS-TOTEM Proton Precision Spectrometer, designed to operate during standard LHC-optics runs.

The possibility to work in these two configurations (high β^* and low β^* runs) would allow the study of a wide range of diffractive CD phenomenons, better describing some already known effects and exploring the possibility to discover new physics.

1.5 TOTEM upgrade: high-β* runs

Since the special high-β^* can be scheduled only a few days per year, during those periods the luminosity provided by the LHC must be as high as possible to collect the highest number of events. However the TOTEM experimental apparatus is not designed to cope with the pile-up expected for this configuration and, in view of the exceptional energy and luminosity foreseen for the new runs, the experiment decided to upgrade its equipment.

Using only the Silicon tracking information on the scattered protons detected by the RP is not enough to properly assign the two particles to their primary vertex of interaction. The pile-up events lead to the collection of multiple simultaneous tracks in the Silicons, resulting in grave issues in matching them with the data collected in the other TOTEM arm. During the 2012 TOTEM-CMS conjunct run, a $\mu \approx 0.05$ led to several difficulties in the selection of a clean sample of CD events.

The project of Installing new RP equipped with precise timing detectors could lead to a significant background rejection and to the possibility to reconstruct (and match them with the CMS data) the primary interaction vertices. The difference of the protons' arrival time in the two arms timing RP stations ($t_{RP1} + t_{RP2}$) and the z-coordinates are related by the equation:

[5] A zero-bias trigger includes all the events, from both background and physics processes.

$$vertex\,position(z) = |t_{RP1} - t_{RP2}|\,c \qquad RP_{distance} = \frac{(t_{RP1} + t_{RP2})\,c}{2} \tag{1.14}$$

The resolution needed to obtain a proper rejection during the high-β^* runs is $\sigma_t \approx$ 50 ps[6]. The timing detectors developed are the same used for the CT-PPS Collaboration and they will be described in detail in section 1.6.1. Their electronics will be discussed in chapter 3. The upgrade also included the development of an optical fiber-based precise clock distribution system to match the timing information between the stations installed in the two arms. The whole timing apparatus is shown in fig. 1.6.

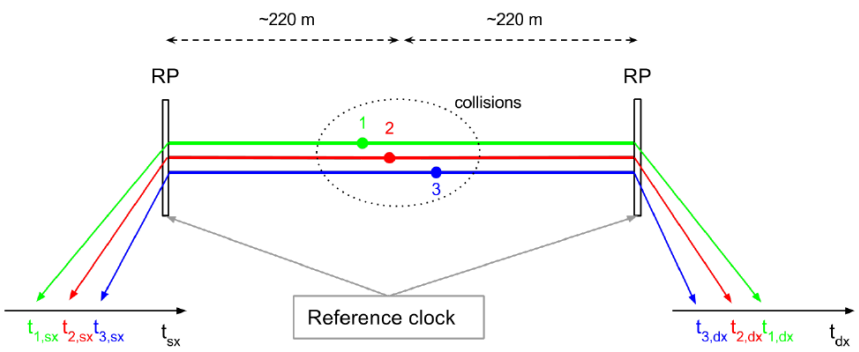

FIGURE 1.6: *Sketch of the TOTEM timing apparatus [49]. The protons' time arrival differences in the two arms are used to reconstruct the z-coordinates of the interaction vertices.*

The introduction of precise ($\sigma_t \sim 100$ ps, as will be described in the next sections) timing detectors will lead to an expected background rejection from 22% to 8.5% of the total events [10]. The high-β^* will therefore result a perfect environment for the search of rare CD events: search for Glueballs candidates, low-mass resonances, exclusive central diffractive $c\bar{c}$ and jet productions. Moreover, observing channels with missing mass in the central zone and studying the rapidity gaps detected using T2, the apparatus can be used to measure the reconstructed mass difference (M_X - $M_{central}$) to search for new particle productions. The TOTEM-CMS collaboration physics program is better discussed in reference [11].

[6]The RMS of the vertex longitudinal position for the high-β^* runs is $\sim$ 7 cm, hence a z-coordinate resolution of at least $\sim$ 1 cm is required [11].

1.6 The CMS-TOTEM Proton Precision Spectrometer

The possibility of the conjunct apparatus to work during standard high-luminosity runs led the Collaboration to develop a new project. The CT-PPS experiment employs the optics of the LHC, using the beam line as a spectrometer: with the low-β^* optics, the bending dipole magnets ensure that the displacement on the X-Y axis of the scattered surviving protons will be proportional to the momentum loss in the interaction. The $\sim$ 210 m RP stations are equipped with timing and tracking detector units. fig. 1.7 shows the layout of the beam line in the 210 m region.

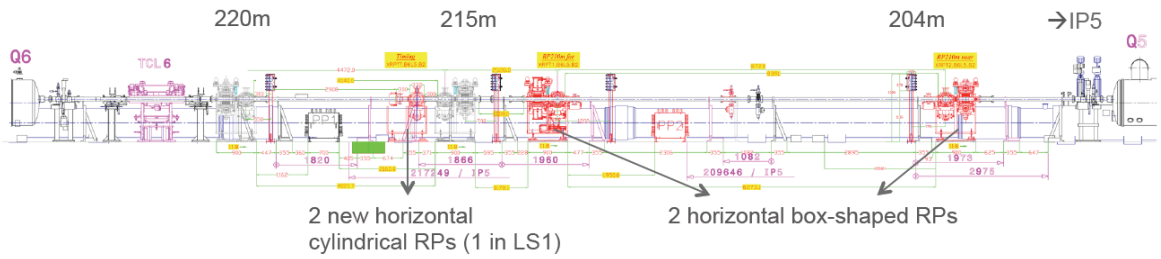

FIGURE 1.7: *Layout of the CT-PPS apparatus after the first LHC long shutdown [13].*

Since the expected pile-up for the high-luminosity optic is $\mu = 30 \div 50$, the timing resolution required to match the RP track with the central products X, is higher than the one previously reported for the TOTEM experiment 1.5. A $\sigma_t \sim 10$ ps would lead to a vertex position resolution of $\sigma_z \sim 2.1$ mm and consequently to a background rejection factor of ≈ 25.

The expected high rate of protons in the RP locations during the standard runs, led to an R&D project on a radiation hard technology for tracking and timing detectors and a new design for the RP vessels to house them. After several simulations on the beam-induced heating and the longitudinal and transverse beam instability, a new cylindrical horizontal RP shape has been preferred to minimize the impedance coupling of the vacuum chamber with the beam, while the old "box shaped" chambers were equipped with cylindrical radio frequency shields and a new geometry of ferrite rings. These alterations are well explained in reference [49]. fig. 1.8 displays the new RP geometry.

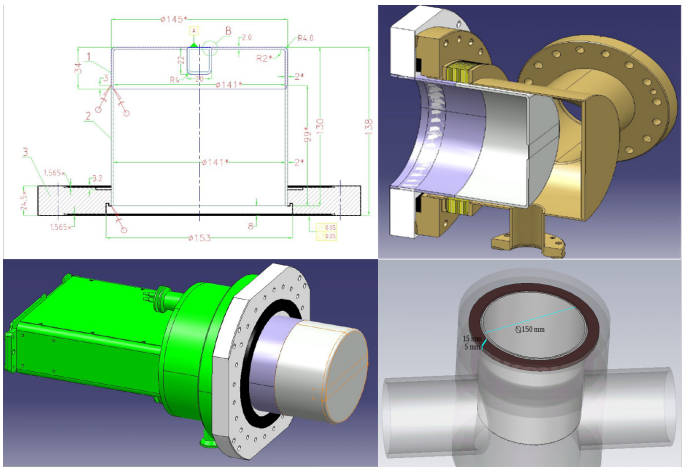

FIGURE 1.8: *Projects for the new CT-PPS cylindrical roman pots[13, 49].*

The beam line simulations, using the well known IP5 transport matrix 1.7, allowed the extraction of the optics parameters. Taking the amplitude function (during high-luminosity runs) to be $\beta^* = 0.6$ m, the normalized emittance results to be $\epsilon_n \approx 3.75{\cdot}10^{-6}$ m. Using the vertex resolution of $\sigma_{x,y}* = 15\mu$m and an angular beam divergence of $\sigma_\theta*$, the Collaboration managed to plot the expected distance from the beam center of the detectors as a function of the RP location. Plot 1.9 shows the results.

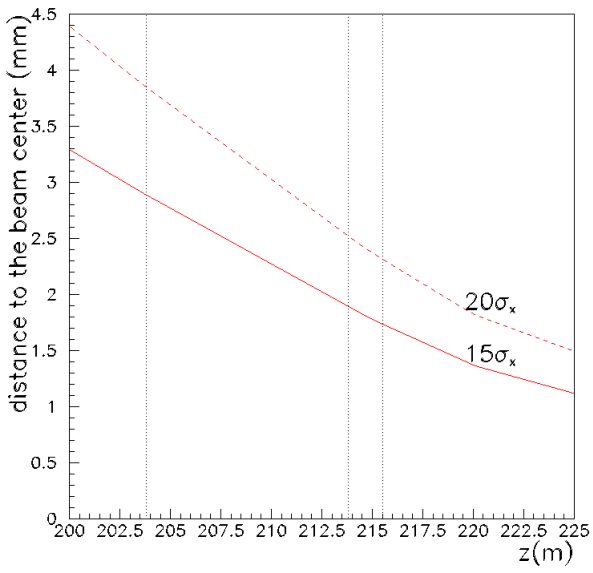

FIGURE 1.9: *Horizontal distance of the tracking and timing detectors from the beam center [13]. The values are calculated for an approach of 15 $\sigma_{beam}(x)$ and 20 $\sigma_{beam}(x)$ of the Roman Pots and a simulated crossing angle of 142.5 μrad.*

The dimensions of the detectors (constrained by the inner volume of the RP) determine the $|t|$ and ξ coverage. Using ellipses centered in y = 0 that reflect the

effect of the quadrupole magnets at the RP location, the Collaboration simulated the scattered protons' distribution, for fixed values of $|t|$ and ξ. Plot 1.10 was obtained supposing 15(20) σ_{beam} of distance from the beam center and the detectors to be 0.3 mm far from the thin window's edge.

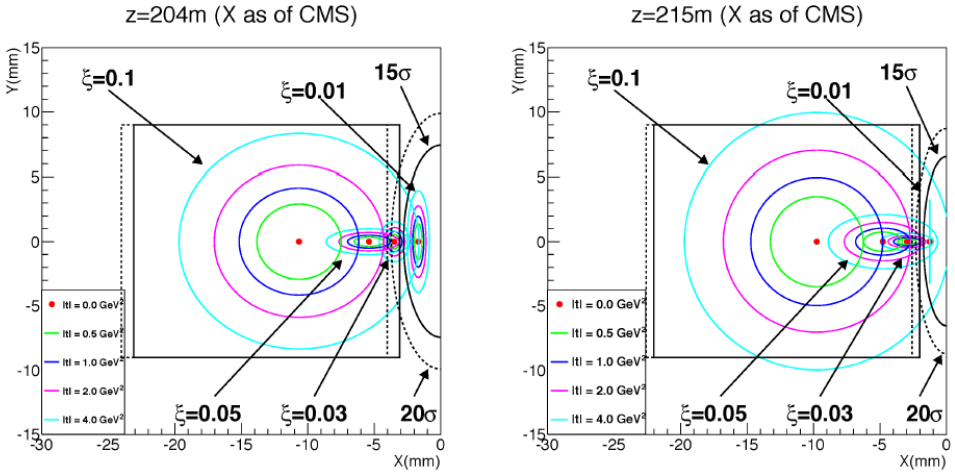

FIGURE 1.10: *Simulated particle distribution for fixed values of $|t|$ and ξ, propagated to the CT-PPS detectors location [13]. The solid (dashed) lines represent the $15\sigma_{beam}$ ($20\sigma_{beam}$) boundaries.*

The mass acceptance (which reflects the ξ one, given the proportionality between the two) depends on the detectors' maximum proximity to the beam and therefore on the LHC optics. Simulating the acceptance behavior with the already mentioned LHC optics and a detectors' distance of $15\sigma_{beam}$, the reconstructed values of masses by the RP fall in a 350 - 1700 GeV/c^2 range, with an acceptance of at least 5%. The plots in fig. 1.11 display the mass acceptance and reconstructed resolution results obtained with the simulations.

1.6.1 Timing detectors

During the development of a precise radiation hard timing detector for the horizontal CT-PPS Roman Pots, the Collaboration took into account several different solutions. After a first R&D on *Quartic* Čerenkov detectors which did not achieved the expected performance, the baseline of the project focused on the use of diamond sensors (explained in-Chapter 2). The results obtained with the Quartic detectors and their use for other timing purposes are reported in references [13, 14].

The diamond timing detectors were developed to fulfill both the TOTEM's and the CT-PPS's requests. The difference between the two configurations is only due

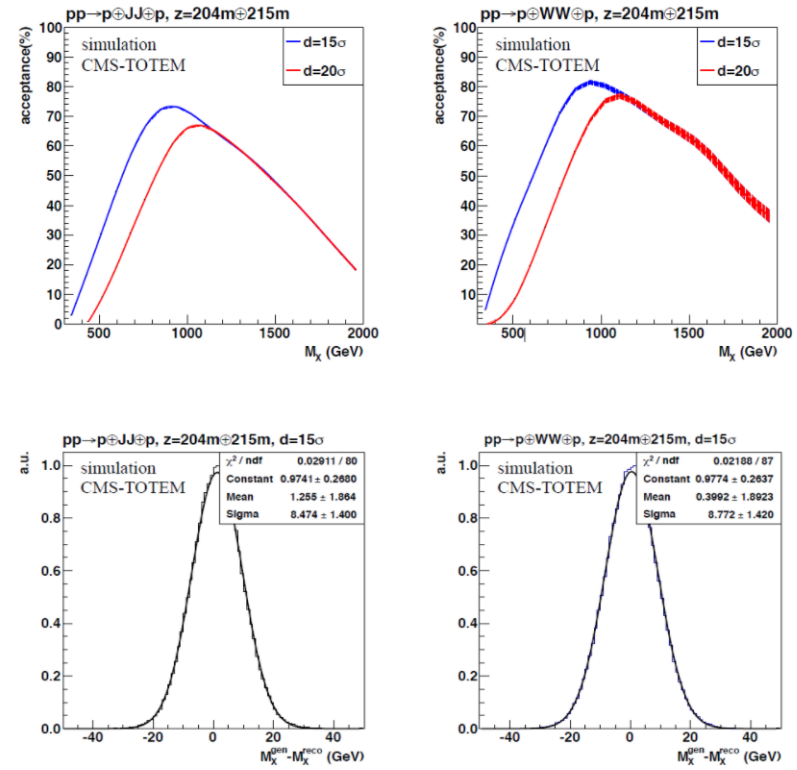

FIGURE 1.11: *In the top row: plots of the CT-PPS acceptance with respect to the value of the mass generated in the central zone of CMS [13]. In the bottom row: resolution of the reconstructed masses produced in the entire spectrum in the CT-PPS acceptance.The plots were drawn studying two different CD events: a di-jet production and a WW production in the central zone.*

to the different proton occupancies (caused by the different optics in high-β^* and low-β^* runs) and will be explained in section 3.1.1. The simulated occupancies are shown in fig. 1.12.

The diamond detectors' performance were initially tested on an ion-electron mixed beam at DESY [16, 24]. In plot 1.13 the spatial efficiency, calculated for a 2-strips 3.1.1 diamond detector (with a spacing between the electrodes of 0.1 mm), slowly decreases approaching the strip's edge.

Time precision measurement of the detectors was performed first in a test beam of 5.6 GeV/c electrons at DESY, and repeated later in a 180 GeV/c pion beam at CERN North Area 4.1. Measuring it for different pixels, the time precision results to cover an interval between $80 < \sigma_t < 108$ ps and correlates with the pixel capacitance that ranges between $0.29 < C < 2$ pF. Their relation is displayed in plot 1.14

The CT-PPS diamond timing detector's characterization will represent one of the main goals of this thesis, therefore a more accurate description will be provided in

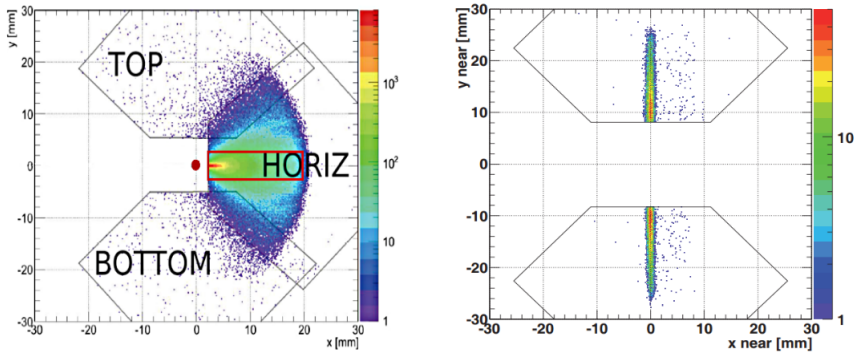

FIGURE 1.12: *Comparison between the occupancies of the TOTEM and the CT-PPS experiment [13]. On the left: the CT-PPS's horizontal timing detectors are displayed. On the right: TOTEM's timing detectors' occupancy in the vertical Pot.*

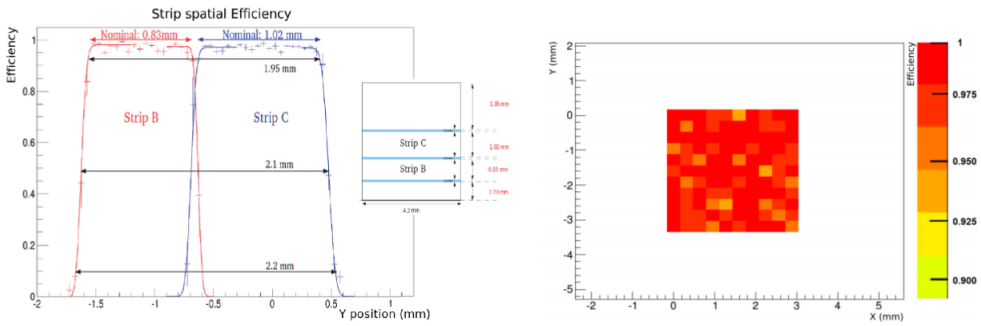

FIGURE 1.13: *On the left: Efficiency as a function of the position (reconstructed with the DESY DATURA Silicon tracker[15]) measured on two adjacent diamond strips. On the right: particle detection efficiency for one diamond sensor; the statistical error on each bin is 5 - 10%.*

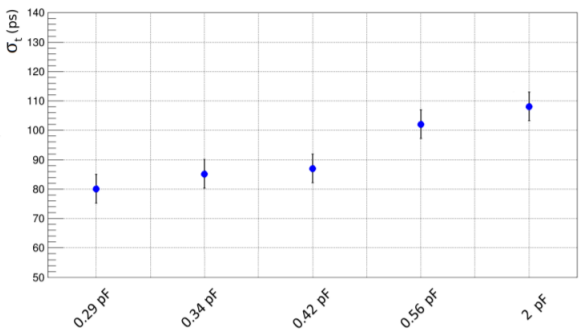

FIGURE 1.14: *Time precision plotted with respect to the pixel capacitance[15]*

the next chapters. Table 1.2 summarizes the results achieved during the diamonds' time precision studies:

Sensor	Pixel area [mm^2]	C [pF]	σ_t	Ampl. [V]	Rise Time [ns]	S/N
Strip A	0.7 × 4.2	0.29	80	0.74	1.48	30
Strip B	0.83 × 4.2	0.34	85	0.70	1.51	31
Strip C	1.02 × 4.2	0.42	87	0.70	1.48	30
Strip D	1.35 × 4.2	0.56	102	0.62	1.49	28
One pixel	4.2 × 4.2	2	108	0.39	1.56	18

TABLE 1.2: *First results obtained wit the TOTEM - CT-PPS diamond timing detectors [16].*

In concurrence with the diamond detectors' production, the Collaboration has pursued an R&D project on a new promising technology for timing detection: the Ultra Fast Silicon Detectors (**UFSD**). These detectors are Low-Gain Avalanche Diodes (**LGAD**) developed by the RD50 at CNM with an n-p-n silicon sensor with a high ohmic p-bulk. As shown in fig. 1.15, inside the bulk a p$^+$-implant extends for several microns underneath the n-implant.

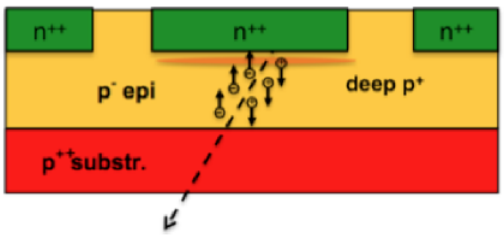

FIGURE 1.15: *Sketch of a LGAD sensor [13].*

The p$^+$ region grants a gain of 10-100, generating a local field at a depth of 1 -5 μm. The LGAD gain is significantly lower than a normal Avalanche Photo-Diode's (**APD**) and, like for APD, the charge multiplication for the holes is negligible, hence the dead time after the avalanche process is drastically reduced and the induced signal faster [29]. However, the noise affecting the LGADs is significantly lower than the APDs' one which reflects in a lower number of electron-hole pairs (**EHP**) generated from thermal noise excitations. The resulting SNR will therefore be higher. fig. 1.16 shows the timing precision measured and a complete description of the results obtained testing the UFSD performance during this thesis' work were published and can be found in reference [22].

1.6.2 Tracking detectors

The CT-PPS Collaboration developed a new tracking detector system to be housed inside the RP vessels. The need of a much more radiation-hard technology determined the substitution of the edgeless Silicon sensors in use by the TOTEM

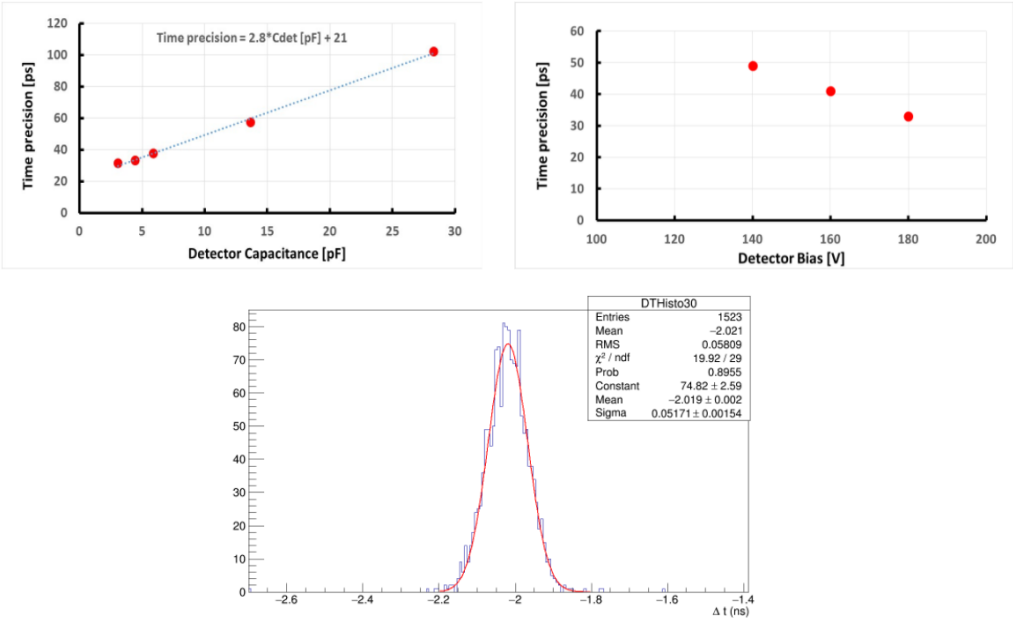

FIGURE 1.16: *Plot of the UFSD's resolution measured during the Test beam sessions at the CERN North Area [17]. The resolution shown in the bottom was measured acquiring the difference of the arrival time measured by an MCP (whose performance are described later, on this thesis 4.1.) and by a 2.2mm^2 UFSD pixel biased at 180V*

experiment. The standard TOTEM Silicon detectors would not be able to cope with the luminosity predicted for the low-β^* runs as they are expected to survive only a few months in these conditions. In plot 1.17, the distribution of protons simulated for an integrated luminosity of 100 fb^{-1} is shown.

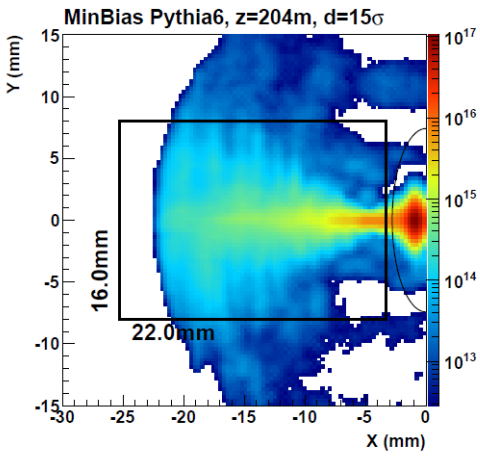

FIGURE 1.17: *Simulated proton fluence in one of the CT-PPS tracking stations, with an integrated luminosity of 100 fb^{-1} [13].*

The new tracking detectors are based on 3D Silicon sensors [13]. An array of columnar electrodes with a radius r $\sim$ 5 μm and doped with both p and n types are inserted in a Silicon p-type bulk. Ohmic p-type electrodes are connected to the sensor's bottom to apply the bias voltage while, in its front side, n-type electrodes are read out. This technology disentangles the substrate thickness from the inter-electrode distance allowing the reduction of the carriers' drift time without affecting the quantity of charge generated. A sketch is provided in fig. 1.18.

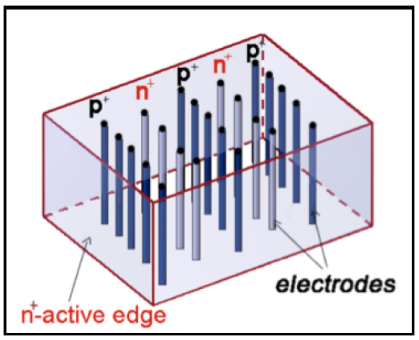

FIGURE 1.18: *Sketch of a Silicon 3D detector [13, 55].*

The packages to be inserted in the RP will be composed of six 3D Silicon detector layers read out by a PSI46dig read-out chip ROCs [45] (which reads 52×80 pixels with dimensions 150×100 μm^2). The front-end electronics were designed to fit inside the RP volume and to be compatible with the readout chain of the CMS pixel detectors [37]. The sensors' sizes are 1.6×2.4 cm^2 and their resolution on the x-z plane is about 10 μm while the one measured on the y axis is $\sim$ 30 μm.

The 3D sensors were tested with a 25 MeV proton beam at Karlsruhe Institute of Technology (KIT) to monitor their effective radiation hardness. The results measured at a maximum fluence of $\sim 1{\cdot}10^{16}$ n_{eq}/cm^2 are explained in reference [13] and show the 3D Silicons' correct functioning during the successive characterization tests. The sensors' production has been carried on by the FBK (Trento, Italy) and CNM (Barcelona, Spain) [52, 60].

1.6.3 A new physic's scenario: low-β* runs

The capability of CT-PPS to operate during standard LHC high-luminosity conditions will open a new physics scenario for the conjunct apparatus of CMS and TOTEM. The electroweak sector and subtle QCD events will be investigated in a high-Q^2 framework and the experiment's unique sensitivity to Beyond the Standard Model (**BSM**) physics will be advantageous to study the CEP with missing transverse energy in the central zone of CMS p + p $\longrightarrow$ p $\oplus$ $\not{E}_T$+ X $\oplus$ p as well

as to improve the previously set limits on Anomalous Quartic Gauge Coupling (**AQGC**)[7] (or possibly find a deviation from the Standard Model).

The CEP are $|t|$-channel processes where the carrier exchanged must be neutral in flavour, electric charge and color. The possible carriers predicted by the Standard Model (**SM**) are therefore photons, Z-bosons and gluons (if their color is neutralized).

1.6.3.1 The LHC as a photons collider

The LHC also functions as a photon collider. Even if the luminosity is lower than the one of an electron-positron accelerator, its accessible energies are unique: $\sqrt{s_{\gamma\gamma}}$ up to $\sim$ 1 TeV. The detection of the photons' energies is ensured by the reconstruction of the central products and the tagged protons in the forward zone. Since the high pile-up doesn't allow for the discrimination of hadronic final products ($\gamma\gamma \longrightarrow q\bar{q}$), the main detected final states are X = e^+e^-, $\mu^+\mu^-$, $\tau^+\tau^-$ and W^+W^-. Requiring both the mass reconstructed by the central and the forward zone to be the same and exploiting the z-coordinate timing information, the background affecting the di-lepton states can be strongly suppressed.

While the cross sections for the di-lepton production are equal (lepton universality) and for M($\ell\ell$) $\geq$ 350 GeVc^2 $\sigma_{\gamma\gamma\longrightarrow\ell\ell} \sim$ 1.5 fb [13], the W^+W^- production cross section grows with the increase of energy. It becomes a factor $\approx$ 20 larger than the previous one at large $\sqrt{s_{\gamma\gamma}}$ due to the spin in the t-channel exchange: J = 1 instead of J = 1/2.

In the SM, fermions and gauge bosons couplings are constrained by the symmetries of the Lagrangian. The possibility to study these channels, sensitive to triple and quartic gauge boson coupling, opens a new window on BSM effects. While the non-abelian gauge nature of the SM predicts the existence of the channel $\gamma\gamma\longrightarrow$WW, the neutral quartic couplings $\gamma\gamma\longrightarrow$ZZ and $\gamma\gamma\longrightarrow\gamma\gamma$ are only allowed in the SM through loops. Studying the AQGC would provide a stringent test of one of the least understood mechanism in particle physics, namely the electroweak symmetry breaking [38].
A closer look at two of these channels is provided below:

- $\gamma\gamma\longrightarrow$WW
  It is a pure Quantum ElectroDynamic (**QED**) process where a couple of W bosons are generated in the central zone and the protons surviving the interaction are scattered at low angles. Since no proton remnant is expected, it can be considered an exclusive channel. fig. 1.19 shows the Feynman diagram of the interaction.

[7] Processes which involve the interaction between four gauge bosons in the same vertex.

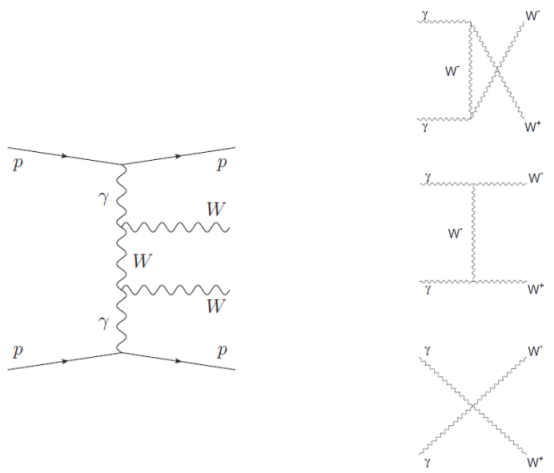

FIGURE 1.19: *The Feynman diagram for the WW production via the two photons' exchange is displayed on the left. On the right: diagrams contributing to the scattering amplitude, at the lowest order perturbation series with a coupling* e^2 *[32].*

A proper selection of the products in the central zone can be achieved reconstructing the z-coordinate of the interaction vertex using the information from the leptonic decay of the W bosons and matching it with the reconstruction using the two surviving protons (timing and tracking detectors in the CT-PPS forward zone). Moreover, requiring missing energy in the central zone $e^+e^-\not{E}_T$ ($\mu^+\mu^-\not{E}_T$), the background coming from the $\gamma\gamma \longrightarrow \ell^+\ell^-$ interactions, which has a p_t of a few GeV and cross sections an order of magnitude smaller than the $\gamma\gamma \longrightarrow W^+W^-$, can be rejected. CMS has observed two candidate events with large missing energy and $e^\pm\mu^\pm$, without any other track [13]. The data, acquired with a luminosity of 5.05 fb^{-1}, resulted to be consistent with the SM prediction (2.2 ± 0.4 events with a 0.84 ± 0.15 background) and set a new limit for the AQGC coupling (1.5×10^{-4} GeV^{-2} for $a^W_{0(c)}/\Lambda^2$ [33]). Tagging the protons with the CT-PPS apparatus, collecting an integrated luminosity of 100 fb^{-1}, an expected improvement of a factor of 2 on these limits (or perhaps a deviation from the SM prediction) could be achieved.

- $\gamma\gamma \longrightarrow \gamma\gamma$
  Contrary to most of the LHC experiments, CT-PPS aims to measure the four photon couplings in a model-independent way, since any new electrically charged particle[8] could contribute to the light-by-light scattering loops

[8]Most of the BSM theories predict the existence of new heavy particles with exotic electric charges.

[40]. The scattering amplitude will be completely defined by these particles' masses, spins and electric charge. The SM di-photon exclusive production with intact protons in the final state occurs through several contributions, however, these can be decomposed in two main instances: the QCD di-photon exclusive production via gluon exchange (with a third gluon exchanged, to maintain the interaction colorless), and via photon exchange. The respective Feynman diagrams are shown in fig. 1.20.

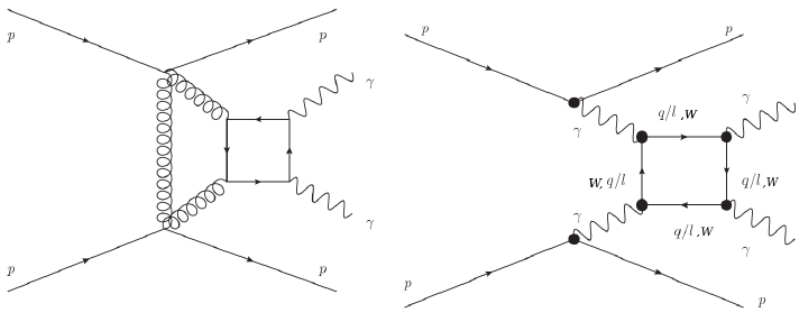

FIGURE 1.20: *Diagram of exclusive di-photon productions with intact protons in the final state predicted by the SM [13, 26].*

However, plot 1.21 shows that, increasing the cut on the di-photon mass, the dominant contribution to the integrated cross section is provided by the light-by-light scattering (its contribution starts getting over the QCD one at a di-photon mass of $\sim$ 100 GeV/c^2). Both photons are required to have $p_t(\gamma) \geq 10$ GeV/c.

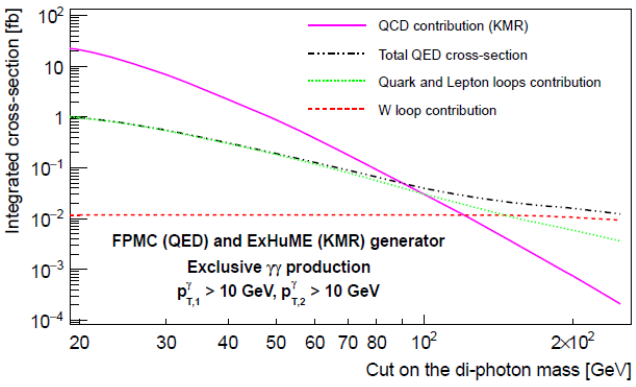

FIGURE 1.21: *Integrated cross section as a function of the di-photon mass. The plot shows the various contributions to the coupling loop. W bosons, quarks and lepton loops (and their interference) have to be considered to reconstruct the cross section predicted by the SM [40].*

Since the final state will be composed only by neutral particles, the primary vertex of interaction has to be reconstructed using the scattered protons. The two photons are required to have similar transverse momentum and a back-to-back angular distribution. Moreover, allowing one of the two photons to be converted in an e^-e^+ couple, the protons' vertex can be matched with the photons' and therefore a better background rejection can be achieved.

1.6.3.2 QCD tests

The color exchange in gluon-gluon interactions normally results in multi-hadron production processes. When the final products studied are multi-jets[9] exclusive productions, however, an opposite-color third gluon is produced in the interaction. The Feynman diagram is shown in fig. 1.22.

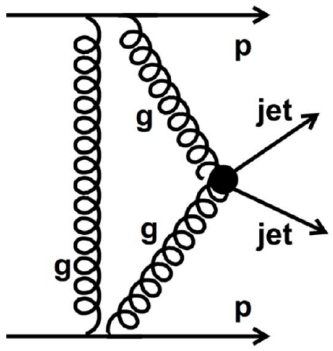

FIGURE 1.22: *Feynman diagram for an exclusive di-jet production.*

Exclusive multi-jet productions are hard diffractive events, characterized by typical rapidity gaps (if no other parton interaction occurs). The studies on the *rapidity gap survival probability*, namely the probability that the rapidity gaps do not happen, give a new way to analyze the multiple soft parton interactions [26]. The two gluon proton vertex will also provide a perfect framework to study, in a range never explored yet, the gluon parton distribution function of the proton. Moreover, the final states obey a $J_z = 0$ (with J_z projection of the total angular momentum along the z-axis), C-even, P-even selection rule [31] and therefore the quantum numbers ($J_z^{PC} = 0^{++}, 2^{++}$) of any new resonance are constrained.

The diffractive di-jet production channels are of great interest since the resulting products are pure gluon jets $\sim 90\%$ of the time [50] and therefore almost without parton jets contribution. fig. 1.23 displays the reconstruction of a di-jet event recorded by the TOTEM-CMS conjunct apparatus.

[9]Production of narrow cones of hadrons generated by the hadronization of partons or gluon after the interaction. Particles carrying a color charge cannot exist in free form because of the confinement predicted by the QCD theory.

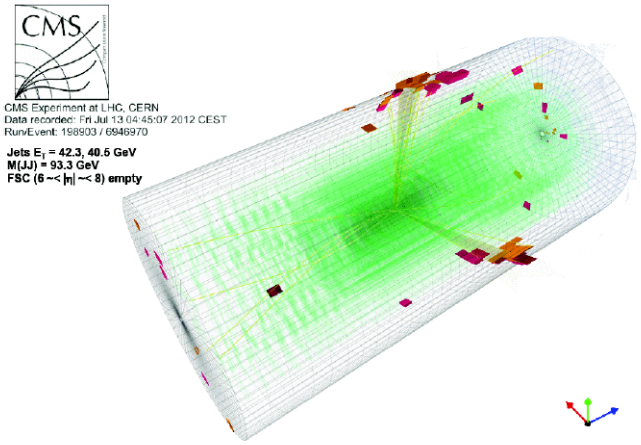

FIGURE 1.23: *Di-jet production recorded during a low pile-up (90 β^*) and $\sqrt{s}$ = 8 TeV by the CMS-TOTEM conjunct apparatus [11].*

Hard exclusive processes with two scattered protons and two or three jets produced in the central region are however a small subsample of the possible central productions and most of the time the final states will contain additional particles. The high pile-up expected affects the reconstruction capability, since the CMS calorimeters cannot be used to detect the rapidity gaps, instead the track-gaps information will be studied. The selection criteria are:

- $\mathbf{M(X) = M(pp)}$
  The central mass must be equal to the missing one reconstructed using the information from the leading protons (with a resolution of $\sim$ 10 GeV/c^2)
- $\mathbf{p_z(X) = -\ (p_z(p_1) + p_z(p_2))}$
  Longitudinal momentum balance
- $\mathbf{p_t(X) = -\ (\vec{p}_t(p_1) + \vec{p}_t(p_2))}$
  Transverse momentum balance

Integrating 100 fb^{-1} CT-PPS Collaboration expects to reach M(jj,jjj) $\sim$ 700-800 GeV/c^2 and using the selection requirements listed above the experiment aims to achieve a unified description of this area of physics which, at low Q^2, represents a significant portion of pp inelastic cross section.

Chapter 2

Characterization of a Diamond detector

Semiconductors aren't only widely exploited for technological and engineering applications. As a matter of fact, particle physics experiments strongly rely on their proprieties, using them as detectors or sensors. A particle, when passing through them, releases a part of its energy that can be converted in a current signal and read out.

Diamonds are indeed more expensive than the more common semiconductors (such as silicon) but present some really intriguing characteristics that convinced TOTEM and CT-PPS to take them into account during the experiments upgrade. The high mobility of their carriers, their drift velocities and their band gap make them good candidates to fulfill the two experiments requirements.

This chapter will detail the considerations that led to the research and development (**R&D**) of a diamond timing detector, first describing their structure and method of production, then exploring the way they interact with ionizing particles.

The last sections will address different ways to read out the sensor. I will also introduce some of the off-line methodologies taken into account to compute the time of arrival of the particles in our timing detectors. The device and the software used will be explained in detail.

2.1 Synthetic diamonds

The electrons, grouped inside a crystal's lattice, tend to occupy the lowest energy levels allowed by the Pauli exclusion principle, distributing themselves in discrete energy ranges called bands. Studying the system at absolute zero temperature, we can define the *valence band* as the highest energy range which the electrons can normally be present at. The maximum energy level is also called *Fermi Energy* and the first band higher than the Fermi one is defined as the *conduction band*.

In solids, to distinguish conductors from semiconductors and insulators we have to study the energy difference between valence and conduction bands, namely the *Band Gap*. In other word, the quantity of energy an electron should have in order to migrate from one band to the other.

While the definitions given are easily applicable to insulators and conductors where the two bands are respectively "distant" and completely overlapped (fig. 2.1), semiconductors have an electrical conductibility halfway between the two.

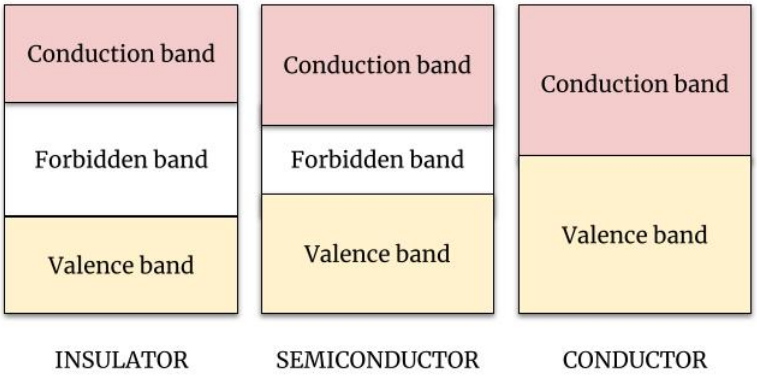

FIGURE 2.1: *Representation of the band gaps in the three different configurations. The forbidden band is the energy distance between the two bands.*

Another configuration can be achieved doping[1] the semiconductor. Changing the crystal's structure we can modify the band gap, hence the material electronic proprieties.
This result can be obtained in two opposite ways:

- **n-type** (majority of negative carriers): adding states close to the conduction band *donors* (e.g. adding Phosphorous or Arsenic to Silicon) we increase the probability of electrons jumping into the conduction band via thermal excitation.

[1] Adding appropriate impurities to the lattice e.g. using two materials with different Fermi energy.

- **p-type** (majority of positive carriers): adding states close to the valence band *acceptors* (e.g. adding Boron or Gallium to Silicon) we let the electrons jump to these new levels, increasing the number of holes (a lack of electrons that can be considered as positive charges) in the valence band.

Diamonds are less exploited than the most common semiconductor on the market, however their characteristic make them good candidates for high energy physics applications.

		Silicon	**Diamond**
E_g	Band Gap (eV)	1.12	5.47 (7.5 eV direct)
E_b	Breakdown field ($\frac{\mathrm{V}}{\mathrm{cm}}$)	3×10^5	10^7
ρ_{el}	Resistivity ($\Omega\,\mathrm{cm}$)	2.3×10^5	$> 10^{15}$
ρ	Density ($\frac{\mathrm{g}}{\mathrm{cm}^3}$)	2.33	3.52
$E_{e/h}$	Energy to create e/h pair (eV)	3.6	13
E_{MIP}	Most probable energy released by MIP ($\frac{\mathrm{MeV}}{\mathrm{cm}}$)	3.21	4.69
$E_{e/h}$	Most probable number of e/h pair created by MIP ($\frac{\mathrm{N}}{\mu\mathrm{m}}$)	89	36
μ_e	Electron mobility ($\frac{\mathrm{cm}^2}{\mathrm{V\,s}}$)	1350	4551
μ_h	Holes mobility ($\frac{\mathrm{cm}^2}{\mathrm{V\,s}}$)	480	2750
v_e	e saturation velocity ($\frac{\mathrm{cm}}{\mathrm{s}}$)	$\sim 10^7$	$\sim 2.6\,10^7$
v_h	h saturation velocity ($\frac{\mathrm{cm}}{\mathrm{s}}$)	$\sim 7.5\,10^6$	$\sim 1.6\,10^7$
ϵ_r	Relative permittivity	11.9	5.7
T_d	Displacement threshold energy (eV)	36	37.5 - 47.6

TABLE 2.1: *Physical properties of silicon and diamond [49, 54].*

As shown in table 2.1, the diamonds' band gap is significantly larger than the silicon's one, thus the energy required to create electron-hole pairs is much higher ($\sim$ 13 eV for diamonds, compared to 2.4 eV for silicon). The charge generated by a particle passing trough the diamond will therefore be lower, for the same amount of energy released in the crystals. However this property guarantees lower *dark current* (better explained in section 2.2.2) as well as the possibility to operate without the necessity to shield the sensors from visible light. No visible photon[2] could create free EHP in the diamond.

[2] $\lambda_{visible} = 380 \div 750$ nm for a resulting mean energy of $\lesssim 3$ eV.

The *drift velocity* v_d, namely the speed electrons can reach inside a conductor or a semiconductor when subjected to an external electric field E, is determined by the carrier mobility μ for a given material. However, plotting the drift velocity as a function of E, the curve starts to saturate when v_d reaches a certain value, called *saturation velocity* v_s. Their relation can be expressed with the equation:

$$v_d = \frac{\mu E}{1 + \frac{\mu E}{v_s}} \tag{2.1}$$

It's therefore easy to understand that large mobilities and saturation velocities, such as the diamonds' ones (table 2.1) mean faster carrier motion, hence a faster collection of charges. The effects of lower *permittivity* ϵ_r and higher *Displacement threshold energy* will be discussed in the next sections.

All these proprieties refer to a perfect crystal, as any defect will influence the detector's optical and electrical proprieties. The imperfections act as traps for electrons, resulting in an increasing probability of electron-hole recombinations which can drastically reduce the output current on the read-out 2.2.3. Moreover the presence of impurities could also create leakage currents inside the sensors 2.2.2.

Therefore the diamonds used for particle detection must be synthesized through complicated and expensive chemical processes to obtain a lattice as free of impurities as possible.
The defects can be classified as:

- *Planar defects*
  Occur when two crystals grow next to each other with an imperfect alignment. The external layers are, by definition, planar defects since the atoms can adjust their position without any impediment.

- *Line defects*
  Also called dislocations, line defects are anomalous arrangements of entire rows of atoms.

- *Point defects*
  The lattice is modified by adding or removing one or two atoms from the crystal, leading to the neighbors' displacement. When an atom is added the potential changes depending on the element that substitutes the carbon. Point defects are called self-interstitial if the new atom is a carbon one and foreign-interstitial if it is not. The defects that mainly interest us are the ones generated when an atom leaves his place in the lattice and a neighbor fills the vacancy created, namely the Frenkel defects. This effect increases with the radiation collected by the diamond.

- *Grain defects*
  Occur when a diamond presents a large number of defects or external contaminations (such as graphite).

It is possible to divide synthesized diamonds in two large branches: **single-crystal** and **polycristalline**. While the first are composed by a single, ordered lattice, the latter are formed by multiple non-ordered single-crystal micro structures and they are, therefore, more prone to defects and imperfections.

The diamond growth technique for the sensors used for this thesis, better explained in reference [26], is called Chemical Vapour Deposition (**CVD**). It uses a ionized gas mixture composed by methane CH_4 and molecular hydrogen H_2, subjected to low pressures and heated with a microwave generator. Once the H_2 strips the hydrogen from the methane, free carbon atoms are created and they can then settle on a pre-built single-crystal substrate.

Once the diamond crystal is created, it can be classified according to the amount of impurities. Table 2.2 shows the variety of synthetic diamonds available on the market.

Type Ia	Nitrogen presence <3000 ppm, non-transparent to UV light
Type Ib	Nitrogen presence <500 ppm, characterized by a yellow or brown color
Type IIa	Small amount of nitrogen impurities, trasparent to UV light
Type IIb	Small amount of nitrogen impurities, the presence of Boron makes the diamond behave like a p-type semiconductor. Characterized by a light blue color

TABLE 2.2: *The table shows the synthetic diamond classification: the presence of impurities changes the crystal's behavior and aspect. The highlighted row represents the type of diamonds preferred for our applications.*

The scCVD used for CT-PPS and TOTEM have been produced by *ElementSix*™[4] which, collaborating with the Uppsala university [43], offered the diamonds with the best quality (boron < 1 ppm, nitrogen < 5 ppm), with a maximum size of 4,5 $mm^2 \times$ 4,5 mm^2 and a thickness of 500 μm.

2.1.1 Metalization

Afte the synthesis a layer of conductive overlay have to be deposed on the diamond crystals surfaces, to provide the sensor a bias voltage and read out the inducted signals. However, non trivial procedures are performed in order to create a good ohmic contact between the diamond's surface and the layers of metalization.

An imperfect deposit of metallic components would create a junction that could act as a diode, not letting current pass through the two materials and, in turn, reduce the sensor performance. For instance one consequence, called *polarization of the Diamond* [58], could result in the accumulation of charge on the electrodes which would decrease the electric field inside the sensor.

The choice of metal and the techniques to deposit it on the crystal surface are indeed crucial. Concerning the electrodes materials, the most efficient choice was proven to be carbide-forming elements (such as Titanium and Chromium) directly laid on the crystal surface, pre-treated in order to create an upper layer of graphite, much more reactive than diamond. Some examples of metalization used are: CrAu, TiPtAu, TiW.

Two main techniques are used to deposit the electrodes: *evaporation* and *sputtering*. During the evaporation method the diamond is kept inside a vacuum chamber to let the evaporated metallic atoms settle on the surface, while sputtering involves ejecting atoms from the metal bombing it with high energy electrons (or ions) which will hit the diamond's surface. During these procedures, different metallic patterns or shapes can be obtained using metal masks. The same results can be achieved later, using a chemical etching technique.

While GSI (CrAu) provided the metalization of the prototype detectors, the final version has been produced by *PRISM* (TiW) [7].

The search for defects in the metalization will be performed during the sensors' quality control: any scratch on the electrodes or imperfection on the layers edges (fig. 2.2) can influence the performance of the detector.

Before gluing and bonding the diamonds on the CT-PPS electronic boards, we checked the quality of the metalizations observing them with the aid of a microscope and its camera-control software. After carefully picking them out of their boxes and cleaning them with isopropyl alcool, we laid the sensors under the lenses and photographed and measured all the edges and imperfections spotted. fig. 2.2 shows some examples for a CrAu metalized diamond.

After the whole procedure, more than 90 % of the detectors were found to be in good condition (or with minor defects) and therefore ready to be glued and bonded. The remaining diamonds were selected to be shipped back in order to be cleaned and re-metalized.

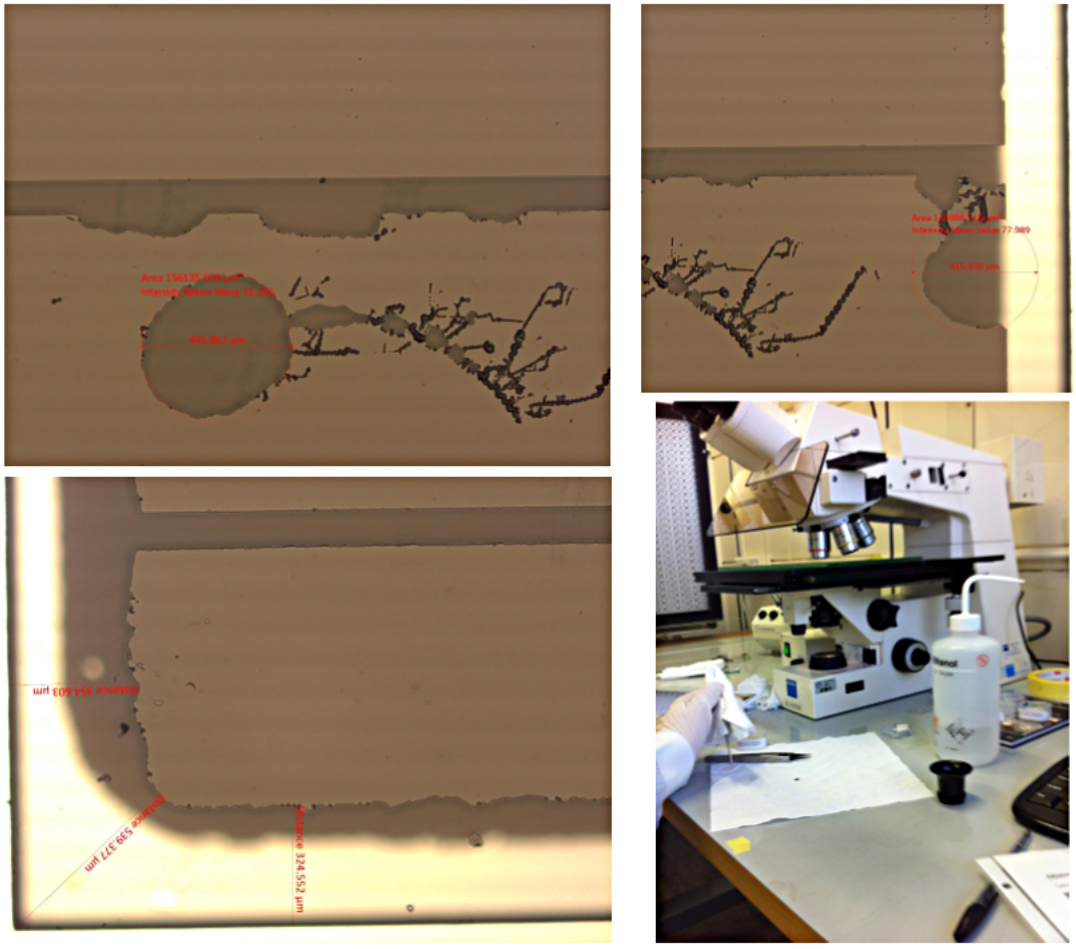

FIGURE 2.2: *Some examples of defects on the metalization layers. In the bottom right a picture of the set-up used in the sensors' electrodes quality check.*

2.2 Particle detection

The above mentioned properties make the scCVD a good candidate for particle detections. Once the surfaces are metalized (section 2.1.1) and the bias voltage is applied, the EHP generated during the passage of a particle can be collected. However, despite their high purity, single crystal diamonds are nevertheless contaminated by some imperfections (like shown in table 2.2) which generate flowing of leakage currents inside them.

The next sections of this chapter will describe the interaction between ionizing particles and diamond detectors, the energy released inside their volume and the effects that bring to signal generation and its collection.

2.2.1 Interaction of charged particles with matter

When a charged particle passes through matter, it loses kinetic energy releasing it into the material via two main effects: *excitation* of bound electrons and *ionization* (gas).

The Bethe-Bloch formula (equation 2.2) approximates with a precision of a few percent (up to several hundreds GeV) the energy lost by heavy particles considering both the mentioned effects (for negligible material thickness).

$$-\frac{dE}{dx} = 4\pi N_a r_e^2 m_e c^2 \rho \frac{Z}{A}\frac{z^2}{\beta^2}\left[\frac{1}{2}\ln\left(\frac{2m_e c^2\beta^2\gamma^2 T_{max}}{I}\right) - \beta^2 - \frac{\delta}{2}\right] \tag{2.2}$$

Where:

- $N_a = 6.022 \cdot 10^{23}\, mol^{-1}$ is the Avogadro number, the number of atoms per gram atom.
- $r_e = \frac{1}{4\pi\epsilon_0} \cdot \frac{e^2}{m_e c^2}$ is the electron classical radius.
- $m_e = 0.511\, MeV$ is the electron mass.
- Z, A are respectively the atomic number and the atomic weight of the material.
- z is the charge of the incident particle (units of elementary charge)
- ρ is the density of the absorber. In our case, for the diamond $\rho_d = 3.52\, g/cm^{-3}$
- $T_{max} = \frac{2m_e p^2}{m_0^2 + m_e^2 + 2m_e E/c^2}$ is the maximum kinetic energy transferable to a bound electron. If the mass of the incident particle is greater than the electron's one $m_0 \gg m_e \Longrightarrow T_{max} \approx 2m_e c^2\beta^2\gamma^2$
- I is the mean excitation of the absorber material's atoms. When Z > 1, it approximately follows the equation:

  $$I = 16\, Z^{0.9}\, eV \tag{2.3}$$

  For a diamond $I_d = 75.3\, eV$ [44].
- δ is a relativistic parameter; it depends on $\beta\gamma$ and it's called *density effect*. The energy lost decreases increasing $\beta\gamma$ until it reaches a minimum for $\beta\gamma \approx 4$; the energy loss is $-\frac{dE}{dx}\Big|_{\beta\gamma\approx 4} \approx 2\, \frac{\text{MeV}}{g/cm^{-2}}$.

When a relativistic particle has an energy loss corresponding to this minimum, it is called *minimum ionizing particle* (**MIP**). As shown in fig. 2.3, different materials (Z, A, ρ...) have different values of energy deposit in correspondence of the minimum value.

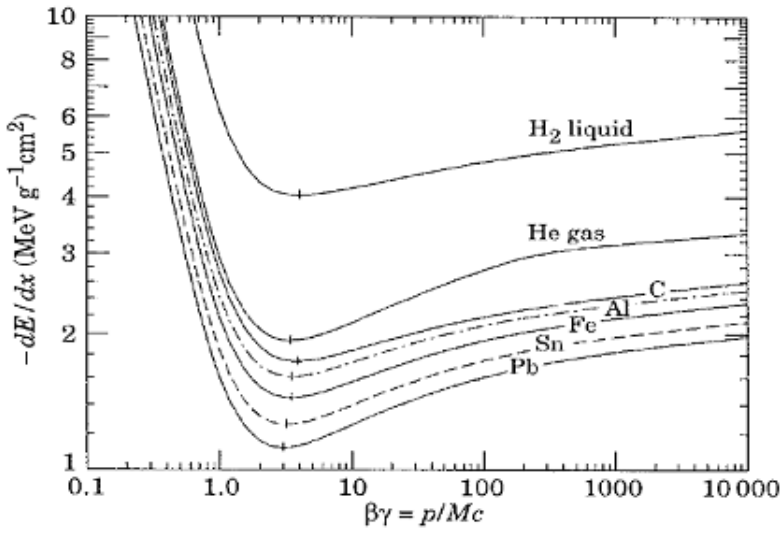

FIGURE 2.3: *Energy loss as function of $\beta\gamma$ for different materials [50].*

However, when the absorber's thickness is not negligible, other effects contribute and the distribution becomes strongly asymmetric and the energy loss can be parametrized by a *Landau distribution*. A reasonable approximation is given by equation:

$$L(\lambda) = \frac{1}{2\pi} e^{-\frac{1}{2}(\lambda + e^{-\lambda})} \tag{2.4}$$

The Most Probable Value (**MPV**) deviation is characterized by λ as:

$$\lambda = \frac{\Delta E - \Delta E^W}{\xi}, \quad \begin{cases} \Delta E = \text{energy loss in an absorber of thickness x} \\ \Delta E^W = \text{MPV of energy lost in an absorber of thickness x} \end{cases} \tag{2.5}$$

with:

- $\xi = 4\pi N_a r_e^2 m_e c^2 \rho \frac{Z}{A} \frac{z^2}{\beta^2} x = k\rho x$; ($x$ is the absorber thickness expressed in cm).

A more realistic formula for the MPV of a particle passing through an absorber of thickness x can be written as

$$\Delta E^W = \xi \left[\ln\left(\frac{2m_e c^2 \beta^2 \gamma^2 c^2}{I^2} \right) + \ln \frac{\xi}{I} + 0.2 - \beta^2 - \delta \right] \tag{2.6}$$

Computing the equation 2.6 for a MIP passing through 500 μm of diamond:

$$-\frac{dE}{dx} \approx 1.3 \frac{\text{MeV}}{g/cm^{-2}} \cdot \rho_d \cdot 500\mu m \approx 230 KeV \tag{2.7}$$

2.2.2 IV Curves

Inside semiconductors, electron and hole pairs are continuously randomly generated and generate a charge flow in the sensors. Even without a bias voltage the carriers can move through the insulating region, producing a quantum phenomenon called *Leakage Currents* (Dark currents). Leakage increases exponentially as the thickness of the insulating region decreases and it constitutes the intrinsic noise of a sensor. It is therefore important to monitor this value to check the performance of our sensors.

In our Set-up the bias Voltage was provided by a Keithley 24100 Sourcemeter while a Keithley 6485 PicoAmmeter read the currents from the strips. Testing the samples again using a radioactive Source (Sr^{90})[3] , allowed us to figure out the ratio between the leakage currents and the actual signal.

fig. 2.4 shows the acquisition set-up. The work done in order to shield the system and provide the best ground connection, allowed us to reduce the noise and self leakage (the set-up intrinsic dark current) of the setup below 10 fA at ± 1 kV, with a standard deviation < 15 fA (comparable to the Keithley 6487 picoammeter lower sensitivity). In reference [36], the whole project is explained better.

A script in C was used to control the bias voltage scan and to read the current data collected while the **GPIB** [4] connection using SCPI communication protocol allowed the communication between the pc and the two Keithley.

Plot 2.5 shows the trend of the current collected from the strips as a function of the bias provided to the diamond. Since the leakage current exclusively depends on the bulk, it can increase with the radiation collected from the sensor and consequent lattice displacements.

Additional contributions to this effect could come from an imperfect metalization. Defects on the metallic surface deposit and more complicated issues could be the cause for surface currents or discharge effects.

[3] $\sim$ 36 MBq β^- emitter. Half life 28.79 y, electron energy: 0.546 MeV.

[4] General Purpose Interface Bus. Originally called IEEE-488, it is a short-range digital communications 8-bit parallel multi-master interface bus specification created in the late '60s.

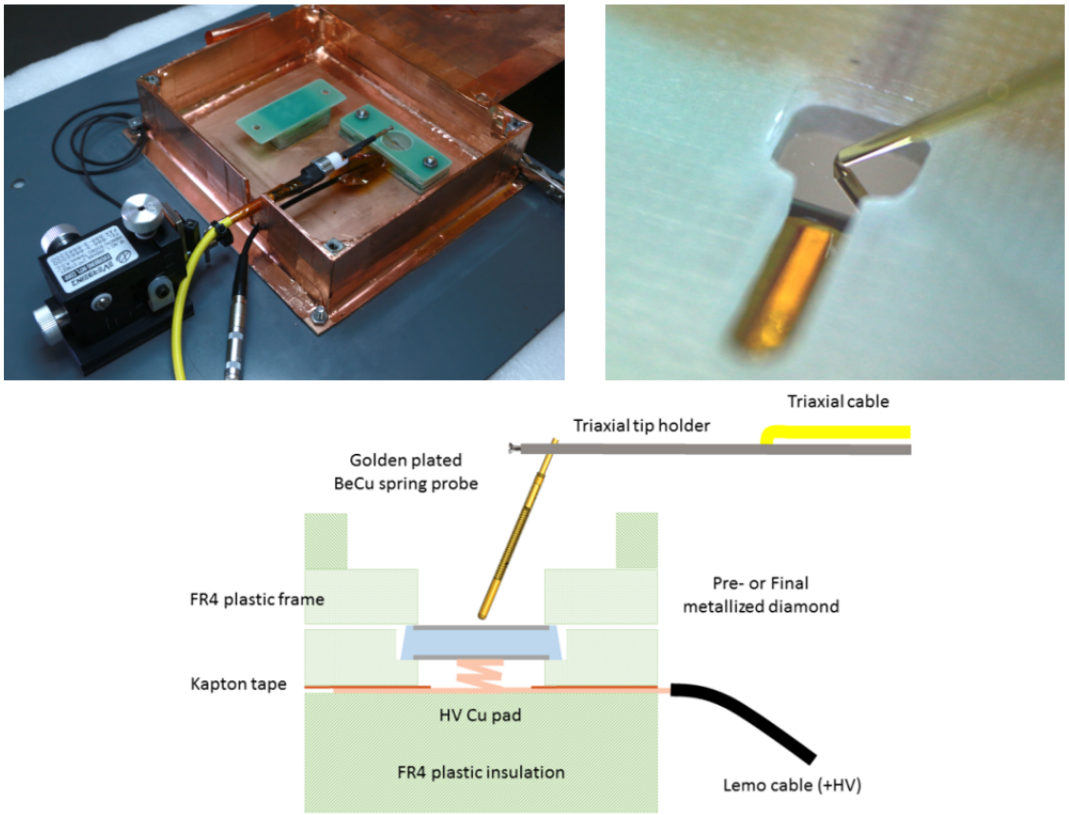

FIGURE 2.4: *On the top left a of the shielded box used during the acquisitions [36]; on the bottom a sectional drawing of the plastic frame. A detail of the spring probe can be found in the top right image.*

2.2.3 Charge collection

We now have to calculate the expected signal induced on the electrodes as well as the charge collected from the read-out circuit. The energy lost from an MIP inside a diamond is about $\frac{dE}{d\xi} \sim 1.3\ Mev\ cm^2\ g^{-1}$ (for a $\beta\gamma \sim 4$) (already explained in section 2.2.1). Knowing the thickness of the sensor, its density and the excitation energy for electron - hole one could define the number of charges generated inside the crystal:

$$N_{eh} = \frac{dE}{d\xi} \cdot \frac{\rho \cdot W}{E_{e,h}} \tag{2.8}$$

Computing the equation with the thickness of our sensor (500 μm) and using the other values listed in table 2.1, we obtain $N_{eh} \sim 18700$. The total collected charge is expected to be $\sim$ 3 fC. However, due to the defects already listed in paragraph 2.1, the collection efficiency cannot be 100%. It is useful to define the *Charge Collection Efficiency* (**CCE**) and the *Charge Collection Distance* **CCE** as:

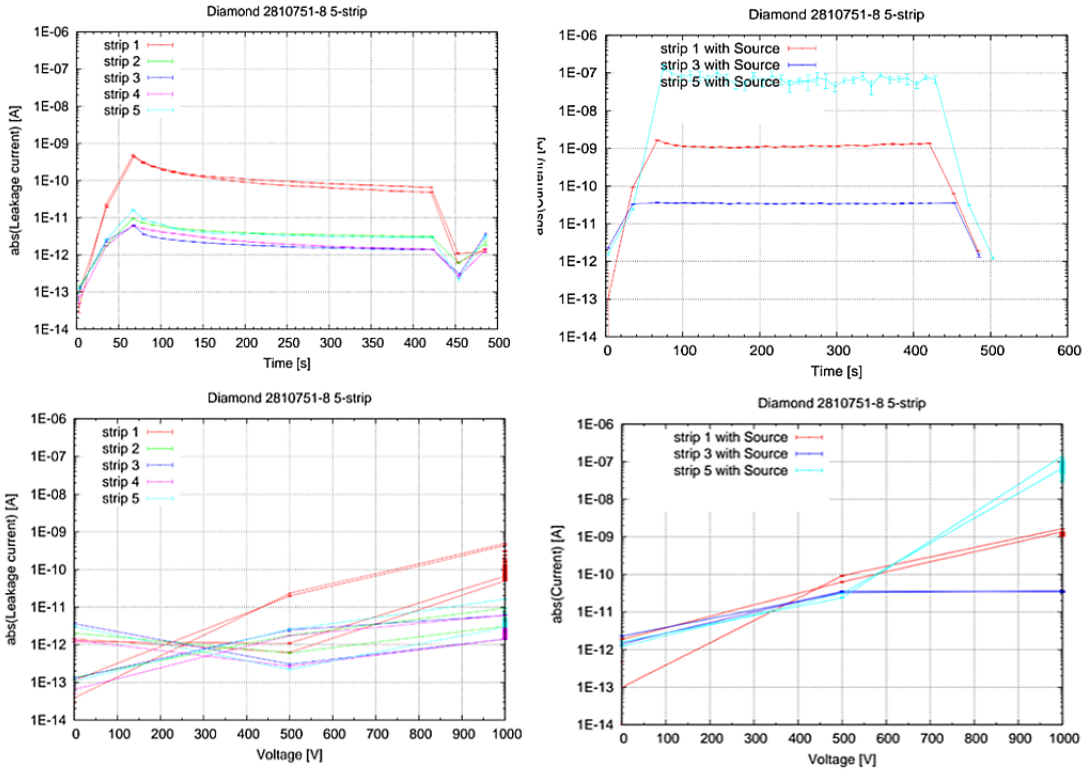

FIGURE 2.5: *The picture shows a 5-strips diamond detector's leakage currents, as a function of the Voltages (bottom left) and Time (top left). On the right the measurement with a Sr^{90} are reported.*

$$CCE = \frac{N_{eh}(collected)}{N_{eh}(0)} \quad , \quad CCD = \frac{N_{eh}(collected)}{N_{eh}(0)} \cdot d \tag{2.9}$$

2.2.4 The Shockley-Ramo theorem

As shown in fig. 2.6, a charged particle passing through the detector creates electron-hole pairs and, if an electric field is present inside the sensor, they can be collected by the electrodes.

The inducted signal amplitude and its shape can be derived using the Shockley-Ramo Theorem [46].

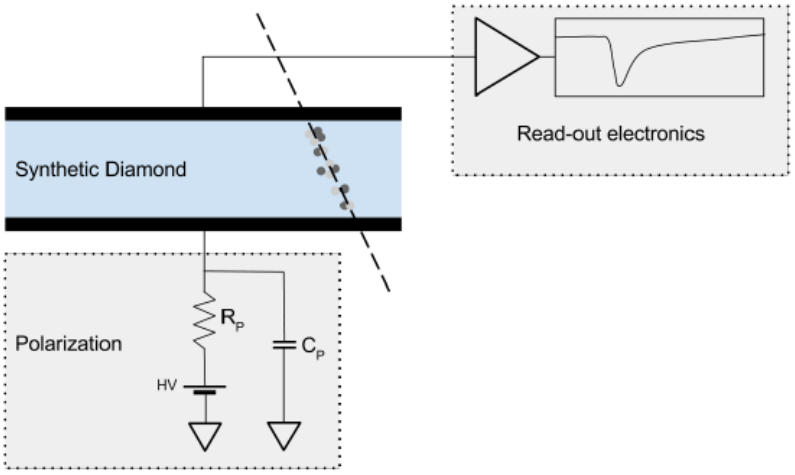

FIGURE 2.6: *Representation of the particle passing trough the diamond detector [49]. The passive components are needed to apply the bias to polarize the sensor.*

$$\begin{cases} I(t) = q\nabla\Phi_w \frac{d}{dt} r(t) = -qE_w v(t) \\ E_w = -\frac{d}{dt}\Phi_w \end{cases} \tag{2.10}$$

Where Φ_w is the weighting potential, v(t) is the particle's instantaneous velocity, and E_w the weighting field.

For a parallel plane configuration, this becomes $E_w = -\frac{1}{d}$, with d being the distance between the two electrodes. Assuming a uniform electric field inside the crystal[5], the induced current can be expressed as in equation 2.11.

$$i(t) = i(t)_e + i(t)_h = q_{drift} E_w (N_e(t) v_e(E) + N_h(t) v_h(E)) \tag{2.11}$$

$N_e(t)$ and $N_h(t)$ are the numbers of electrons and holes created, v_e and v_h their drifting velocities. Finally v_s represents the saturation velocity of the carriers.

Replacing:

$$Q_{drift} = N_e(t) q_{drift} = N_h(t) q_{drift} \qquad and \qquad E_w = -\frac{1}{d} \tag{2.12}$$

[5]This condition is reached when the electrode's width is larger than the detector thickness or comparable to it.

and assuming the electrons and holes velocity to be the same, we can rewrite 2.13 as:

$$i(t) = i(t)_e + i(t)_h \simeq \frac{Q_{drift} v_{e,d}(E)}{d} \tag{2.13}$$

Considering electrons and holes lifetime to be $\tau_e = \tau_h \gg t_{coll}$ *(collection time)*, we can expand the terms, using $t_{max} = \frac{d}{v_{e,h}(E)}$ as maximum particle transit time trough the sensor. Being $\theta(t)$ the Heaviside step function:

$$i(t) \sim \frac{2Q_{drift}}{t_{max}} \theta(t - t_0)\theta(t_{max} + t_0 - t) \tag{2.14}$$

For the diamonds used in our tests (500 μm thick, with a bias voltage of 800 V - 1000 V) , we can expect typical values of:

- $Q_{drift} \sim 2.9$ fC
- $t_{max} \sim 5$ ns

Using the value of expected generated charge inside the diamonds it is possible to simulate the contribution of electrons and holes to the total induced current. The results are displayed in fig. 2.7.

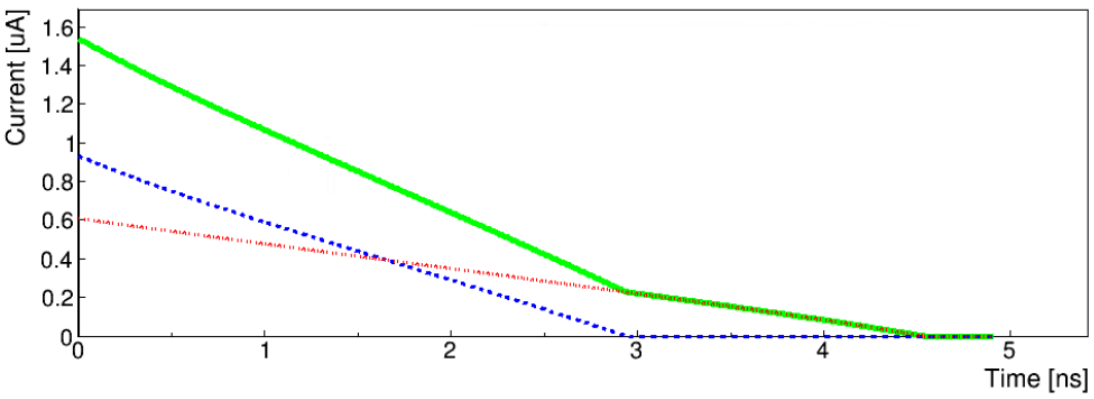

FIGURE 2.7: *Current induced by the passage of a MIP through 500 μm of diamond. The plot is produced using Weightfield2 simulation software [30].*

2.3 Read out a diamond detector

From equations 2.8 and 2.14 we can expect the current signal produced by a MIP passing through our detector to be $\sim \mu A$. On the other hand, section 2.2.2 shows diamonds dark currents (for a detector biased with HV $\sim$ 800 V) to be $\sim$ *O(pA)*. The expected Signal to Noise Ratio (**SNR**), namely the ratio between the signal generated by the MIP and the intrinsic diamond's noise, will be large enough to neglect the effect of the thermal fluctuations (and shot noise[6]).

The situation changes when the sensors are bonded to the read-out since the choice of a pre-amplifier drastically affects the detector response. Three approaches are taken into account: a *Charge amplifier*, a *Broadband amplifier* and an amplifier with *High input impedance*.

2.3.1 Broadband amplifier

The current pulses generated from the detectors can be read out by amplifiers with low input impedance and large bandwidth. As will be better explained in section 2.4, this corresponds to faster rise time which directly affects the timing performance of the detector. However, a larger bandwidth implies a wider noise spectrum which in turn decreases the SNR.

$$SNR = \frac{V_{max}}{\sigma_V} \tag{2.15}$$

σ_V can be analyzed defining the *Jhonson-Nyquist* (or *Thermal*), which express the thermal agitation of the charge carriers inside a conductor. Since the spectral density is almost constant over the whole frequency spectrum, it can be considered White noise. Considering an impedance, we can express the power dissipated using both the voltage and the current:

$$P = \frac{V^2}{R} = I^2 R \tag{2.16}$$

If the only source of current (or voltage) are the thermal fluctuations of the carriers, the variation of the spectral density over the frequency can be expressed as

[6]It is the noise produced from the charge carriers crossing a potential barrier, such as a p-n junction.

$$\frac{dP_{noise}}{df} = 4k_b T \tag{2.17}$$

Where k_b is the Boltzmann constant and T is the Temperature. Using 2.17 and 2.16 we can compute the voltage noise density;

$$\frac{dv_n^2}{df} = 4k_b TR \quad \Longrightarrow \quad v_n^2 = \int 4k_b TR\, df \tag{2.18}$$

The same result apply to the noise voltage calculation measured at the output of an amplifier with input impedance R and a frequency-dependent gain of $A(f)$.

$$v_n^2 = \int 4k_b TR\, A^2(f)\, df \tag{2.19}$$

Hence, the term σ_V can be written as:

$$\sigma_V = A(f)\sqrt{4k_b TRBF} = \sqrt{\frac{k_b TF}{C}} \tag{2.20}$$

Where B, the bandwidth can be written as B = 1/4RC for circuit with only one pole. F is the noise figure[7] of the amplifier; Empirically, the input noise of broadband amplifier follows the relation $\sigma_V \approx \mathrm{nV}/\sqrt{Hz}\cdot\sqrt{B} \propto \sqrt{B}$ [26]. Equation 2.15 then becomes:

$$SNR = \frac{V_{max}}{A(f)\sqrt{\frac{k_b TF}{C}}} \tag{2.21}$$

As pointed out with the equation 2.21, the SNR grows with the increasing of the detector capacitance. As shown in fig. 2.8 these amplifiers cannot be exploited with the capacitance typical of our diamond sensors.

[7] It is defined as the ratio between the total output power of a circuit and the portion attributed to the thermal noise (in the input termination) calculated at T = 290 K and expressed in dB.

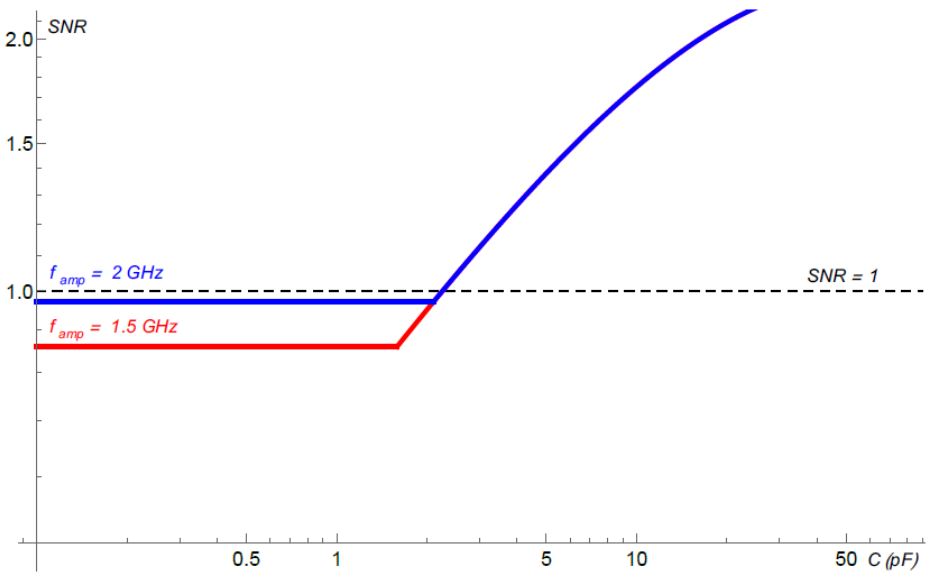

FIGURE 2.8: *Simulation of the SNR response as a function of the detector capacitance, using a broadband amplifier (with input impedance $R_i = 50\ \Omega$) to read a diamond sensor [49]. With the capacitance of the diamonds actually used, the SNR results to be below 1.*

2.3.2 Charge sensitive amplifier

Another approach involves the use of an amplifier which integrates the signals, providing a voltage output proportional to the integrated value of the input current. The easiest circuit we can design uses an ideal operational amplifier (infinite input impedance and open loop gain, zero output impedance) and a feedback capacitor. The scheme is provided in fig. 2.9.

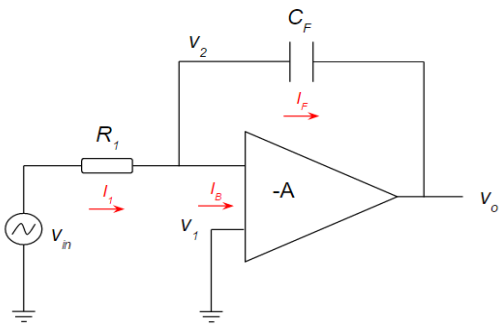

FIGURE 2.9: *Schematic of a charge-sensitive amplifier.*

Solving the circuit, we find:

$$I_1 = I_B + I_F. \tag{2.22}$$

However, since we are considering the input impedance of the amplifier to be infinite, $I_B = 0$ and hence $I_1 = I_F$. Additionally ,the capacitor has a voltage-current relation which follows the equation:

$$I_F = C_F \frac{dV_c}{dt} \qquad \longrightarrow \qquad \frac{V_{in} - V_2}{R_1} = C_F \frac{d(V_2 - V_o)}{dt} \tag{2.23}$$

Since the nodes V_1 and V_2 are kept to the same potential (no current is absorbed by the amplifier) and the V_1 pin is grounded, V_2 presents a virtual ground. Therefore $V_1 = V_2 = 0$ and the equation 2.23 becomes:

$$\frac{V_{in}}{R_1} = -C_F \frac{dV_0}{dt} \tag{2.24}$$

Integrating the two terms we obtain:

$$\int_o^t \frac{V_{in}}{R_1} dt = -\int_o^t C_F \frac{dV_0}{dt} dt \qquad \longrightarrow \qquad V_0 = -\frac{1}{R_1 C_F} \int_o^t V_{in} dt \tag{2.25}$$

The variation of the output signal's amplitude with respect to the input charge is controlled by the choice of C_F. The circuit slightly changes when we consider a real application. In fig. 2.10, the detector is plugged to the charge sensitive amplifier input.

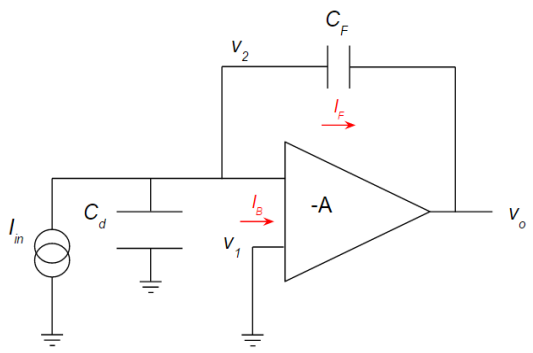

FIGURE 2.10: *Schematic of a charge-sensitive amplifier with our detector plugged (drawn as the parallel between the capacitor C_d and a current generator).*

In this case, the amplifier gain will be determined by the ratio between the detector and feedback capacitance:

$$V_o = -\frac{C_d}{C_F} \cdot \frac{1}{1 + \frac{C_d}{C_F}} Q_d \tag{2.26}$$

Where Q_d is the charge generated from the particle passing through the detector. The exact calculations made to achieve this result can be found in reference [49]. This scheme, however, cannot be used for our purposes. Even considering the circuit to be not "ideal", the time needed to discharge the feedback (and detector) capacitance would be too large and the read-out would end up adding all the followings signals to the first pulse and therefore rapidly reaching the saturation of the amplifier.

Adding a resistor on the amplifier feedback allows for a much more rapid discharge of C_F but reduces the expected gain. The final circuit is shown in fig. 2.11.

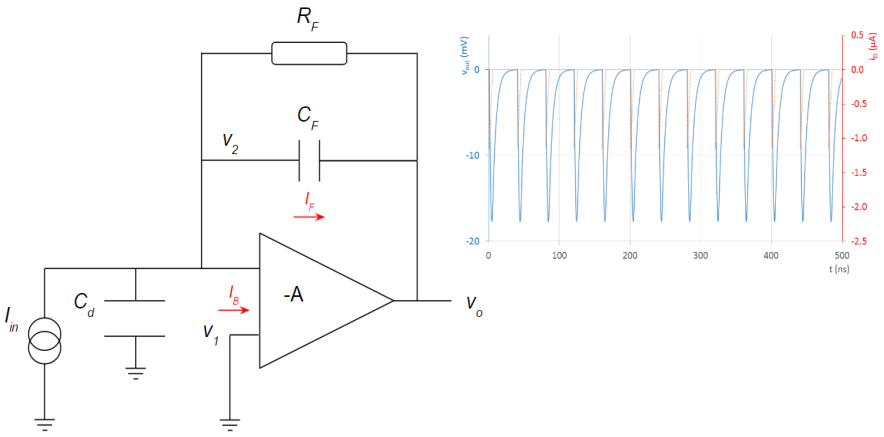

FIGURE 2.11: *A resistor is added to the charge sensitive amplifier feedback, to discharge the capacitor more rapidly. On the left, a simulation of the response is shown [49].*

2.3.3 High input impedance

None of the previous circuits have been chosen as pre-amplifier for TOTEM and CT-PPS boards. The circuit selected (re-adapted from a HADES work [47]) present an higher input impedance than the scheme previously shown in section 2.3.1 in order to maximize the SNR [49].

The circuit, described in fig. 2.12, uses a fast and low-noise SiGe transistor in common emitter configuration.

The SNR can be computed using the same ratio:

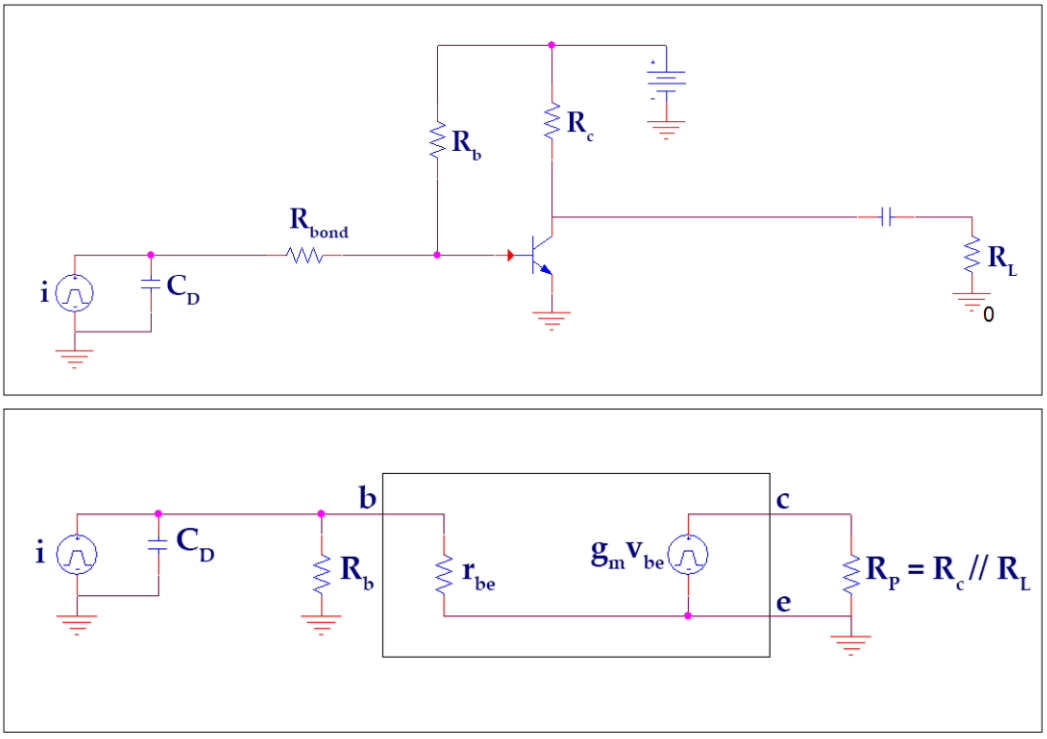

FIGURE 2.12: *Scheme of the pre-amplifier designed by the CT-PPS and TOTEM experiment. In the sketch on the bottom, a simple π model is used to explain the transistor's functioning [49].*

$$SNR = \frac{V_{max}}{\sigma_V} \tag{2.27}$$

Where:

- $V_{max} \propto \frac{R_P}{R_B \| r_{be}} \sim \frac{R_P}{r_{be}}$. The approximation is possible because R_B is chosen to be such that $R_B \parallel r_{be} \sim r_{be}$.
- the thermal noise (2.20) can be rewritten as:

$$\sigma_V = \sqrt{4k_b T R_P B F} = \sqrt{\frac{k_b T F R_P}{r_{be} C}} \tag{2.28}$$

Hence the SNR becomes:

$$SNR \propto \sqrt{\frac{1}{F}} \sqrt{\frac{r_{be}}{R_P}} \tag{2.29}$$

After several simulations, shown in plots 2.13, the best results were reached choosing a value of R $\sim$ kΩ (for detectors with a capacitance of $\sim$ 1 pF).

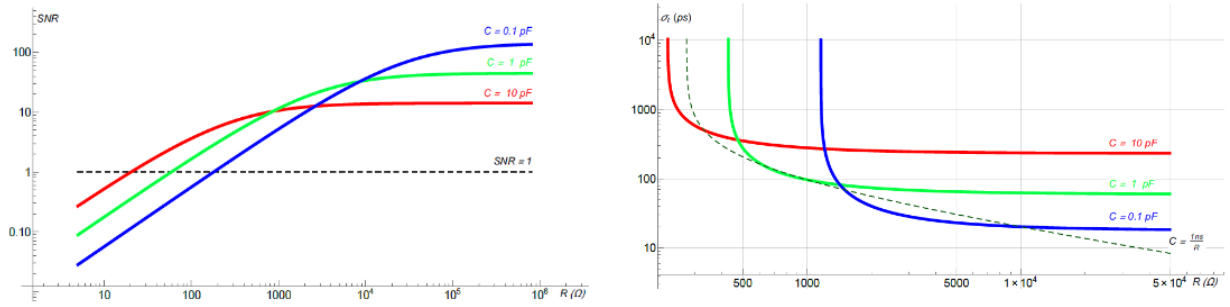

FIGURE 2.13: *The picture shows the trend of the time precision and SNR with respect to the input impedance. The plots have been drawn for several values of the detector capacitance [49].*

2.4 Timing measurement

To measure the time precision of a detector, one method implies the study of the time arrival difference distributions measured by two independent detectors: the one under test and another one used as a time reference. It is therefore essential to know some important parameters, such as their SNR (section 2.2) and signal rise time (defined by the pre-amplifier bandwidth as explained in section 2.3).

The time precision σ_t will not be defined solely by the detector's intrinsic characteristic and the front-end electronics, since the devices used to collect the signals and the off-line data analysis drastically affect the results. The effects introduced by these factors will sum together quadratically, defining the actual detector precision [13].

$$\sigma_t^2 \approx \sigma_{TW}^2 + \sigma_J^2 + \sigma_{TDC}^2 + \sigma_{drift}^2 = \left(\frac{V_{th}}{s/t_r}\right)^2 + \left(\frac{\sigma_v}{V_{max}/t_r}\right)^2 + \left(\frac{TDC_{bin}}{\sqrt{12}}\right)^2 + \sigma_{drift}^2 \quad (2.30)$$

Where:

- n and s stand respectively for the rms noise and signal amplitudes.

- t_r is the signal rise time[8]. Its approximated value can be extracted from the inverse of the amplifier bandwidth, using a conversion factor:

$$t_r|_{10\%-90\%}[ns] \approx \frac{0.35}{BW[GHz]} \tag{2.31}$$

- V_{th} is the comparator threshold. $\sigma^2_{TW} = \left(\frac{V_{th}}{S/t_r}\right)^2$ is the uncertainty introduced by the *time walk effect*, described in section 2.15.
- $\sigma^2_{TDC} = \left(\frac{TDC_{bin}}{\sqrt{12}}\right)^2$ takes into account the TDC precision (if used).
- the *drift* term represents the errors attributed to electronic components defects and aging, as well as thermal drifts of the electronic parameters.

However, since the effects related to the data processing can be overcome (as will be explained in section 2.15) or neglected, a good approximation is given by considering only the effect of the *jitter*[9]. A rule of thumb is given by the equation:

$$\sigma_t \approx \frac{\sigma_v}{V_{max}/t_r} \tag{2.32}$$

If we consider more than one detector, which collect data independently, the resulting uncertainties sum up as shown in the equation:

$$\sigma_{tot} = \frac{1}{N} \cdot \sqrt{\sigma^2_{det1} + \sigma^2_{det2} + ..} \tag{2.33}$$

If n detectors are expected to have the same time precision, the formula can be simplified as:

$$\sigma_{tot} = \frac{1}{N} \cdot \sqrt{\sigma^2_{det1} + \sigma^2_{det2} + ..} \approx \frac{1}{\sqrt{N}} \cdot \sigma_{det} \tag{2.34}$$

In this thesis two approaches have been used during the tests on the timing detectors, which are the *Sampling* and the use of a *TDC*.

2.4.1 Sampling the signals

The best way to acquire large amount of information from a signal is sampling. Sampling means recording, within the device acquisition rate and precision, the

[8]The rise time is defined as the time required for the signal to rise from a certain percentage of its amplitude to another. In this thesis the rise time will always be intended as the time in which the signal grows from the 10% to the 90% of its total amplitude.

[9]The *jitter* effect indicates the time variance for crossing the threshold, due to the thermal and the shot noise.

whole waveform for every particle passing through the detector. Once acquired, with an off-line analysis we can measure every parameter and value needed, minimizing the loss of information.

Moreover, sampling a signal typically gives the opportunity to monitor the waveform in real time and therefore adjust the thresholds, re-align the detectors and instantly check their correct functioning. However, this is not always feasible, since sampling a signal requires a non-negligible amount of computing power and data transfer bandwidth. The expected hit rate is too large to allows the use of a sampler, since with the actual technology any device could not be fast enough to properly process every waveform.

During all the tests done to characterize our detectors, before the installation in IP5, we used the a digital oscilloscope. An **Agilent DSO9254A** oscilloscope [2], shown in fig. 2.14, was selected mainly to provide a large enough sampling rate.

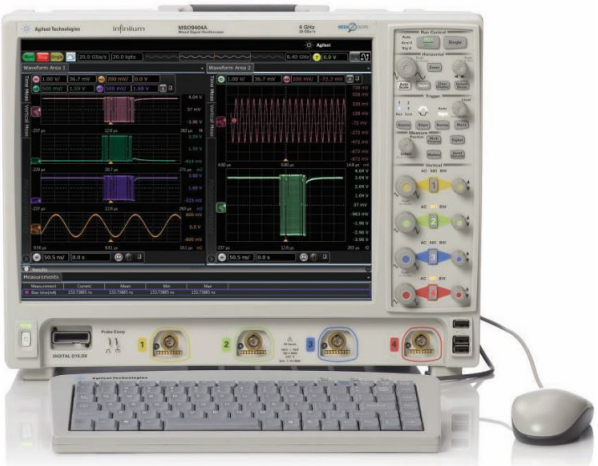

FIGURE 2.14: *Image of a **Agilent DSO9254A**, the same oscilloscope used during all the tests performed during this work [2].*

With a sampling rate of 20 GSa/s and 2.5 GHz of bandwidth it has a maximum memory depth of 20 Mpts using all the 4 channels at the same time but it can reach 1 Gpts using only two of them. The Windows operating system offers a friendly interface and the ability to easily remote control the acquisition.

To decrease dead time after every acquisition, it is possible to set the system in *segmented* mode. This mode allows the acquisition of up to 8000 events, storing them in the oscilloscope memory, and the browsing of the waveforms individually. Using a PYTHON script, the segments can also be saved as binary files.

Once saved, the data are processed with a C++ code which classifies the information into branches of a TTree object of the ROOT library: *FileNumber*, *HitNumber*, *Channel*, *StartTime*, *TimeSamples*, *DataSamples*. Different algorithms were used to analyze the .root files created to extract the needed information.

2.4.1.1 Constant fraction discriminator

One of the most typical electronic signal processing method used to estimate the arrival time of different waveforms is called *constant fraction discriminator*. It consists of a dynamical choice of the threshold depending on the signal amplitude.

As a matter of fact, choosing a static value as a threshold would mean distinct crossing times for signals with different pulse height. As shown in fig. 2.15, two simultaneous waveform with different amplitude, pass through a common V_{th} at different instants. This error on the arrival time due to a non constant amplitude of the input signals is called *time walk*.

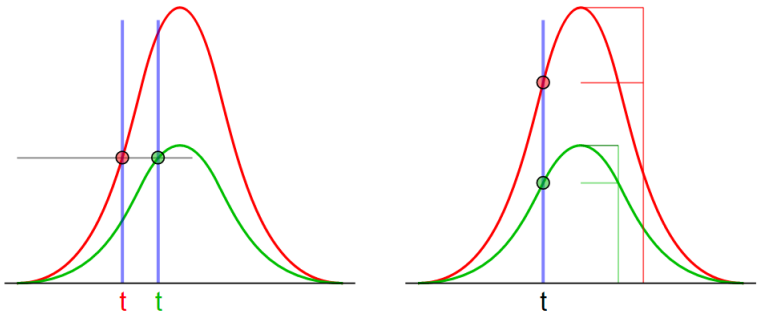

FIGURE 2.15: *Example of time walk effect for two gaussian pulses [59].*

a possible implementation of the CFD consists in splitting the waveform in two lines:

- the first line is delayed by a time $0 \leq t_{delay} \leq t_M$ and sent to the non-inverting input of a comparator. t_M is the time needed to reach the maximum amplitude.
- the second line, after being multiplied by a fraction f of the signal amplitude, is sent to the inverting input of the comparator.

The two lines are then added together and the resulting sum crosses the zero at a time independent from the signal amplitude (fig. 2.16). It provides the starting time for an output logic pulse.

Constraining the sum of the two signals, the inverted and reduced one $V_F = f \cdot V_0$ and the delayed one V_D, to be 0 we can find the value for the zero crossing time t_{cross}:

$$f \cdot \frac{V_0}{t_M} t_{cross} = \frac{V_0}{t_M} (t_{cross - t_{delay}}) \tag{2.35}$$

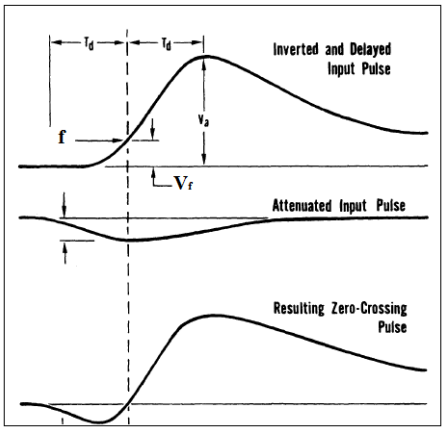

FIGURE 2.16: *Zero crossing obtained after implementing the CFD [39].*

We finally obtain :

$$t_{cross} = \frac{t_{delay}}{1 - f} \tag{2.36}$$

Equation 2.36 shows that using a constant fraction discriminator we remove the dependency on the signal's amplitude. However, working with real waveforms, the choice of the constant f, as shown, for instance in fig. 12 of [48]. In effect, the slope of the leading edge, cutting through the V_{th}, should be maximized in order to reduce the uncertainty due to the jitter effects.

A software implementation of the constant fraction discriminator was used to analyze the data collected with the oscilloscope.

The code extrapolates the particles' arrival time differences between the device under test (**DUT**) and the time reference, using a CFD to correct the threshold crossing time. Moreover, it is designed to scan different values of f, namely the fraction of the signal amplitude. After choosing the signals to be analyzed from the input files, the number of segments to use and the polarity of the signals, a quality monitor feature shows the reconstructed waveforms. With the data quality monitor (**DQM**) we can monitor the range where where to expect the peaks that we need as an input for the code in order to compute the rise time distribution. The output is a list of plots such as the pulse height, the rise time and finally the time resolutions for different values of f.

2.4.2 Collecting data with a TDC

The amount of data required to sample all waveforms at the rates expected inside the LHC cannot be handled by the present system. Another way to read pulses

from a timing detector is to use a Time to Digital Converter (**TDC**).

A TDC produces a start (stop) signal whenever a leading (trailing) edge of a digital pulse crosses its threshold. Therefore, the analog detectors signals have to pass through a discriminator before being connected to a TDC input.

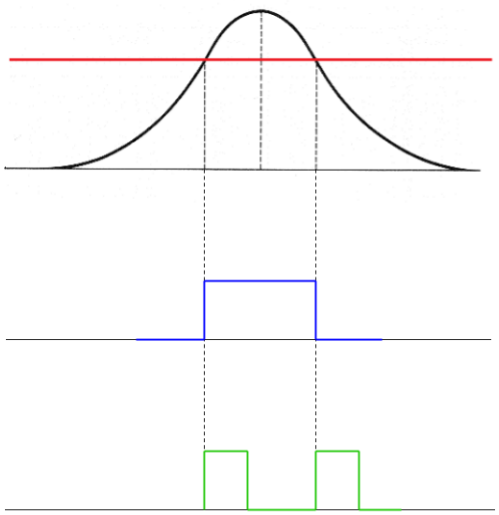

FIGURE 2.17: *The picture shows the phases the signals have to go through before being sent to a TDC. Once a threshold (Red line) is set, the discriminator produces a logic pulse (in Blue) whose leading and trailing edges activate the TDC response (Green square curves).*

The resolution of such object is determined by the binning of the converter:

$$\sigma_{TDC} = \frac{Bin_{\,width}}{\sqrt{12}} \tag{2.37}$$

The time walk is the main issue to overcome, since the crossing time of the discriminator's threshold is strongly related to the signal amplitude (section 2.4.1.1). However, as explained in the next section, this effect can be corrected using the analog pulses width information.

2.4.2.1 Time over threshold correction

Choosing to discriminate our analog signals using a statical threshold, we can process the information provided by the waveform leading and trailing edge crossing to correct the measurement. The parameter we need to obtain is called *time over threshold* t_{TOT} and it is shown in fig. 2.18.

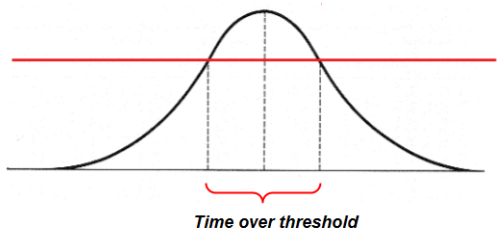

FIGURE 2.18: *Time over threshold (Red line) for a gaussian pulse.*

We can always define a function $\Phi(t_{tot})$ so that the crossing time can be corrected by this value, removing the time walk effects.

$$t_{real} = t_{th} + \Phi(t_{tot}) \tag{2.38}$$

Where t_{th} represents the threshold crossing time before the correction. Even though finding the function $\Phi(t_{tot})$ while working with real signals can be analytically impossible, we can minimize the time walk effect using two independent measurements.

$$\Delta t = t_{real2} - t_{real1} = t_{th2} + \Phi_2(t_{tot2}) - (t_{th1} + \Phi_1(t_{tot1})) \tag{2.39}$$

If $\Delta t \to 0$:

$$\Phi_1(t_{tot1}) = t_{th1} - t_{th2} - \Phi_2(t_{tot2}) \tag{2.40}$$

Averaging t_{tot2}, $\Phi_2(t_{tot2})$ is a constant:

$$\langle \Phi_1(t_{tot1}) \rangle_{t_{tot2}} = t_{th1} - t_{th2} - const \tag{2.41}$$

Fitting the plot of the difference $t_{th1} - t_{th2}$ with respect to t_{tot}, we find the value of the constant. One example is shown in fig. 2.19.

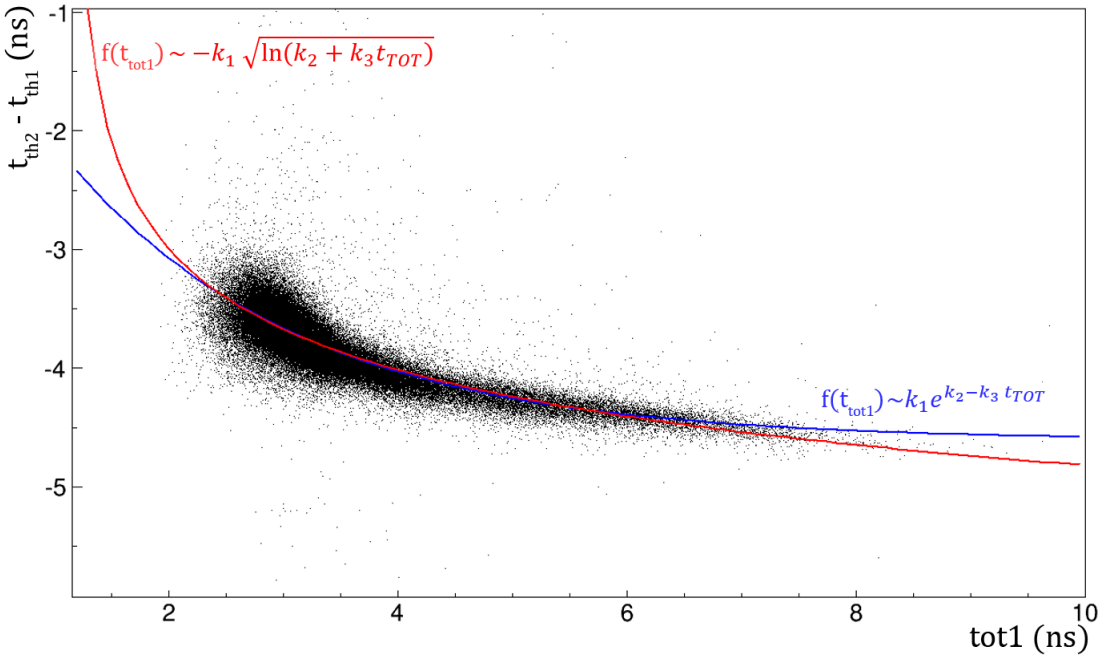

FIGURE 2.19: *The curves shows two possible corrections for the time walk, using a time over threshold algorithm [49].*

Chapter 3

Front-End electronics for CT-PPS detectors

This chapter will be dedicated to the description of the CT-PPS timing detectors, explaining in detail their front-end electronics and their features. The hybrid boards used to house both the sensors and the amplifiers will be the main subject of the first sections, explaining the technical and electronic changes we had to make in order to adapt them to different type of detectors. The last sections will identify the NINO boards, namely the boards discriminating and processing the particles' time of arrival.

3.1 The electronic boards

In this section, I will provide an accurate description of the electronic boards developed by the TOTEM and CT-PPS experiment. These boards, built with 4 layers of substrate Rogers RO4350B and RO4450F (very good insulators and low loss materials, ideal for radio frequency applications) are designed to house both the detectors and the whole amplification chain. For this reason they are called "*Hybrid boards*".

Each of the hybrid boards has 12 channels and three stages of amplification, listed below:

- **Pre-Amplifier**
  Re-adapted from a HADES work [47], the device consists of a transconductance preamplifier placed as close as possible to the diamond ($\sim$ 1 cm), in order to minimize the input capacitance. It uses a SiGe BJT with low-capacitance in a common emitter configuration (as shown in fig. 3.1). The

sum of the capacitances of the diamond, the wire used to connect the electrode to the BJT base and the transistor is the total capacitance of the pre-amplifier. In order to be optimized for timing purposes ($\sigma_t < 100ps$ for all the pixels), TOTEM and CT-PPS carefully chose the feedback and collector impedances, obtaining an input impedance of few kΩ and a high SNR. The preamplifier has a maximum current gain of 45 dB at low frequency with a drop of -20 dB/decade and it reaches 0 dB at 4 GHz. The RMS noise on the output is about 78 μV.

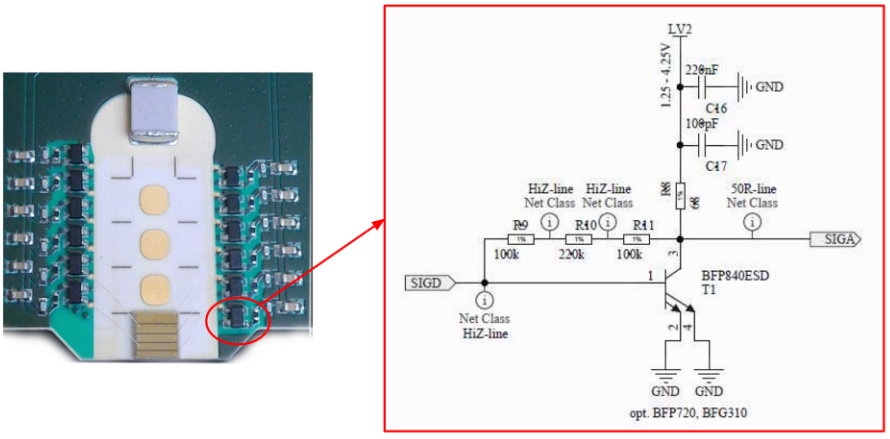

FIGURE 3.1: *Detail of the board, zoomed on the detector and pre-amplifier zone. On the right the schematic is provided [15].*

- **ABA**
  The main part of th second stage, as shown in fig. 3.2, is a broadband Avago ABA-53563, a commercial amplifier with an almost flat power gain over the frequency of about 21 dB and a noise figure of 3.5 dB. This component has been chosen mainly for its constant group delay which grants low shape distortion of the input signal. The ABA inputs and outputs are matched to 50 Ω. This stage is followed by a 10 dB attenuator on the output to prevent saturation of the larger signals.

- **Booster&Shaper**
  The last stage, displayed in fig. 3.3, is a shaper consisting of two wide-band BJT transistors NPX BFG425W. It has a power gain of 53 dB at 200 MHz with an effective noise bandwidth of about 425 MHz.

The whole amplification chain reaches a maximum gain of ≈ 84 dB at about 200 MHz. Each of the 12 channels dissipate about 0.3 W. SMP connectors were preferred for sending the detectors signals to the read-out due to their frequency range (up to 40 GHz) and their 50 Ω impedance.

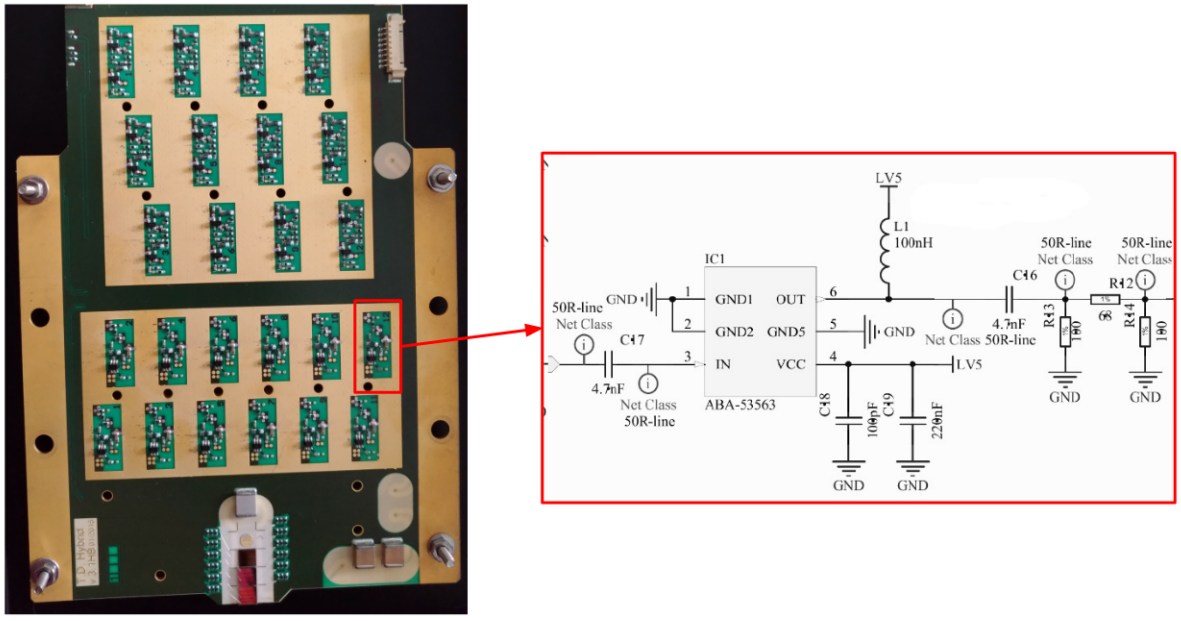

FIGURE 3.2: *On the left: the position of one of the twelve Avago ABA-53563 is highlighted in red. On the right: the schematic of the second stage of amplification [15].*

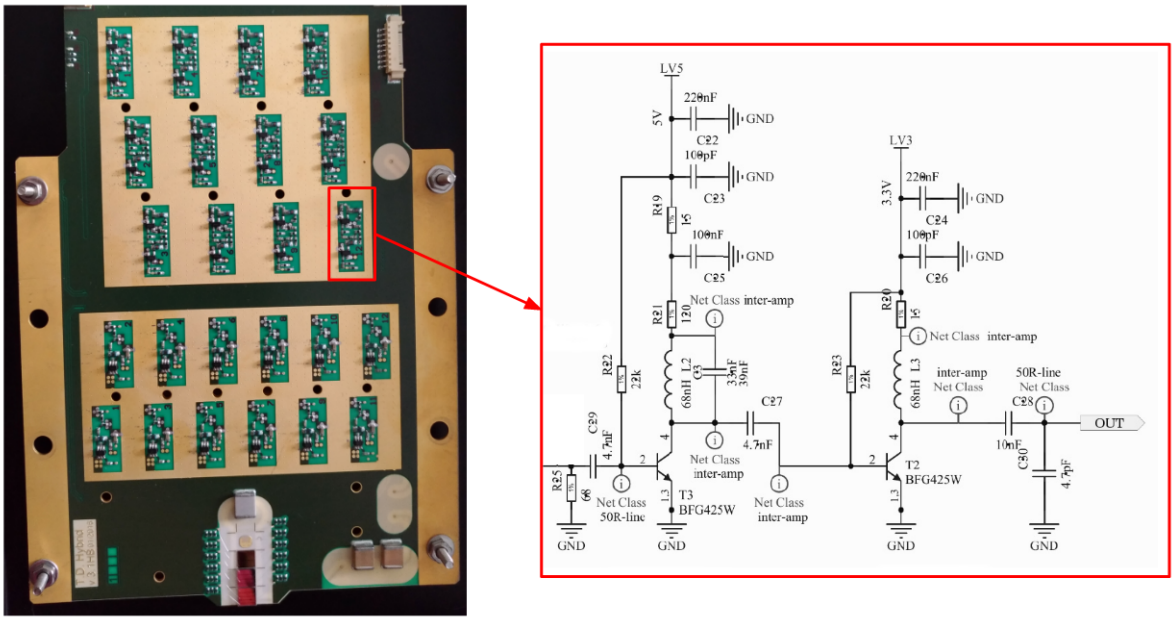

FIGURE 3.3: *In the picture the Shaper's position on the board and its schematic are shown [15].*

A two-pin flat connector soldered on the boards' back brings the bias voltage to the HV pads on which the detectors are glued. Another two flat connectors (7 and 8 pins) are used respectively to provide the low voltages to the amplifiers and to monitor the temperature and pressure information.

The board's shape is designed to fit inside the Roman pots' volume, substituting the silicon detectors, still used in the TOTEM experiment. Their 4-layer arrangement inside the pots is better explained in section 3.2.

3.1.1 Hybrid boards for the diamonds

The boards were originally optimized to house the 4.5 mm^2 and 500 μm thick diamond timing detectors. The Hv pads' surfaces and their positions on the board change between the TOTEM and CT-PPS configurations, to maximize the particles' occupancy expected by the simulations. The two arrangements are compared in fig. 3.4.

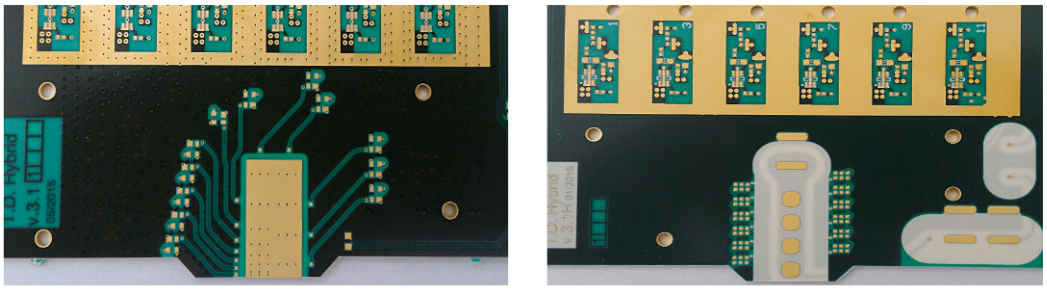

FIGURE 3.4: *Comparison between TOTEM and CT-PPS bias voltage pads' geometry. The TOTEM board, on the left, has a single pad which covers the full detector zone. It can house up to 8 diamonds distributed on two columns. The CT-PPS configuration, on the right, is designed to have four $\sim$ 2.5 mm^2 pads in a single column.*

The metalization patterns have been selected to maximize the granularity in order to cope with the density of particles in the detectors' zones closest to the beam. Indeed, while the more distant diamonds have a single-pad metalization, the crystals glued near the bottom of the boards have their surfaces divided into 5 electrodes, which get smaller to the board's end.

As shown in fig. 3.5, the dimension of the pixels are:

- Pattern 1: 4.2 mm ($\times$ 4.2 mm)
- Pattern 2: 1.75 mm, 2.35 mm ($\times$ 4.2 mm)
- Pattern 3: 0.81 mm, 0.91 mm, 1.02 mm, 1.16 mm ($\times$ 4.2 mm)
- Pattern 4: 0.550 mm, 0.650 mm, 0.750 mm, 0.850 mm, 1.00 mm ($\times$ 4.2 mm)

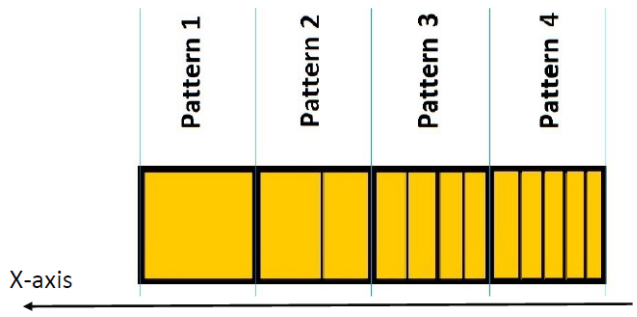

FIGURE 3.5: *Metalization pattern for the TOTEM and CT-PPS experiments.*

The Al bond wires which connect the sensors to the pre-amplifiers were chosen to be 150 μm, thicker than the standard 25 μm bonding wire, in order to minimize the discharge effects since the probability of sparks on the conductor's surface is inversely proportional to its radius of curvature.

3.1.2 Hybrid boards for the Ultra Fast Silicon Detectors

Recently, during the YETS (Year-End Technical Stop) 2016, CT-PPS Collaboration decided to install a modified board housing an UFSD detector in one of the packages. The goal of this operation is to measure the radiation hardness of this technology and find if these silicon sensors might perform better than the diamond detectors presently used.

In order to fit the boards, a prototype with 15 pixel has been glued and tested to one of the TOTEM hybrids, as shown in fig. 3.6. However, during the tests only 5 of the pixels available were connected, the ones which presented breakdown voltages greater than 180 V and leakage current lower than 0.1 mA.

Due to their intrinsic gain, the signals' amplitudes are expected to be $10 - 100$ times greater than the diamonds'. It was decided to bypass the second stage of amplification (ABA 3.1), using only the pre-amp and the Booster (Shaper). Nevertheless, the larger capacitance of the 50 μm thick silicon detectors (which scales linearly with the pixels area, as ~ 2 pF/mm^2) would have resulted in a larger rise time of the signals. For this reason, the pre-amp feedback impedance has been reduced to 1 k$\Omega \div 300\ \Omega$, accordingly to the pixel size.

3.2 The detector packages

Once the hybrids were tested, they had to be installed inside the roman pots. Since adding stages of detection improves the precision of the timing measurement (σ_n

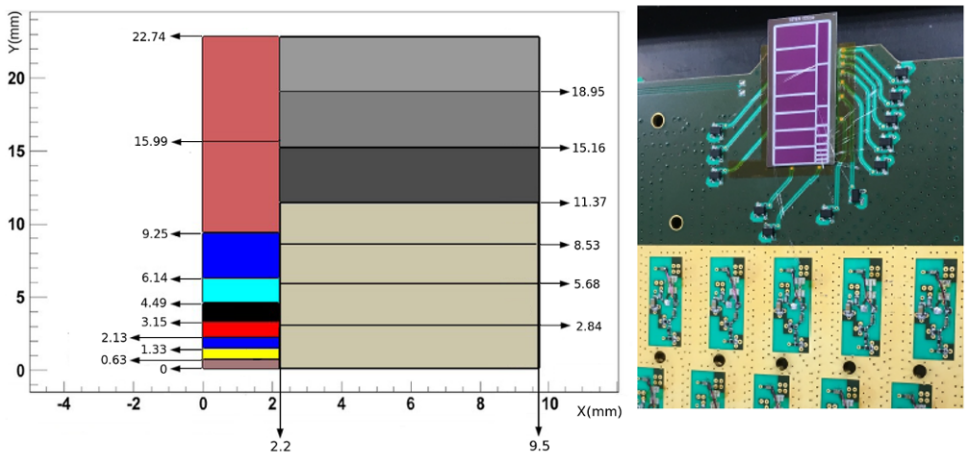

FIGURE 3.6: *The 15-pads UFSD timing detector glued on one of the TOTEM hybrid boards [22] and bonded with standard 25 μm wires. On the left a scheme of the pixels' size is provided.*

$\propto 1/\sqrt{N}$), a structure with four layers of detection was chosen.

The 4-layers structure developed by the Collaboration shown in fig. 3.7 is designed to host the cooling system, the signal cables flange and the feedthrough board. In the same sketch 3.7 the outer hermetic container, called "champignon" (named after its particular shape), on which the vacuum bellow can be attached.

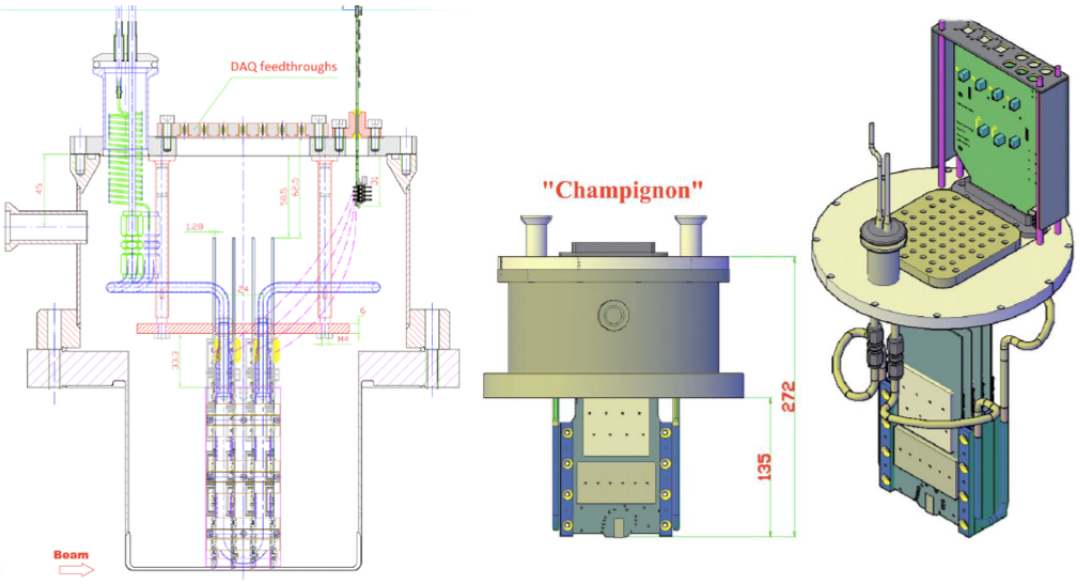

FIGURE 3.7: *Three different sketches of the 4-layers structure developed to arrange the hybrid boards inside the roman pots. In the central picture, the detectors are stored inside the aluminum "champignon" [13].*

The SMP signals' cable pass through a flange, while all the remaining external and internal connections are interfaced through the feedthrough board (shown in fig. 3.8):

- a 12-pins connector provides the low voltages to the feedthrough board which then powers the hybrids. The board is provided with potentiometers to manually set the amplifiers' voltage.
- 4 SHV connectors, one for each layer are used to sent the hv to the hybrids with 2-pins flat connectors whose wires are soldered to the feedthrough's bottom.
- a mezzanine houses the I^2C controllers used to monitor the temperature and pressure as well as to remotely define the voltage values for the amplifiers on the hybrids.
- the boards are equipped with a radiation monitor, to check the dose received inside the inner volume.

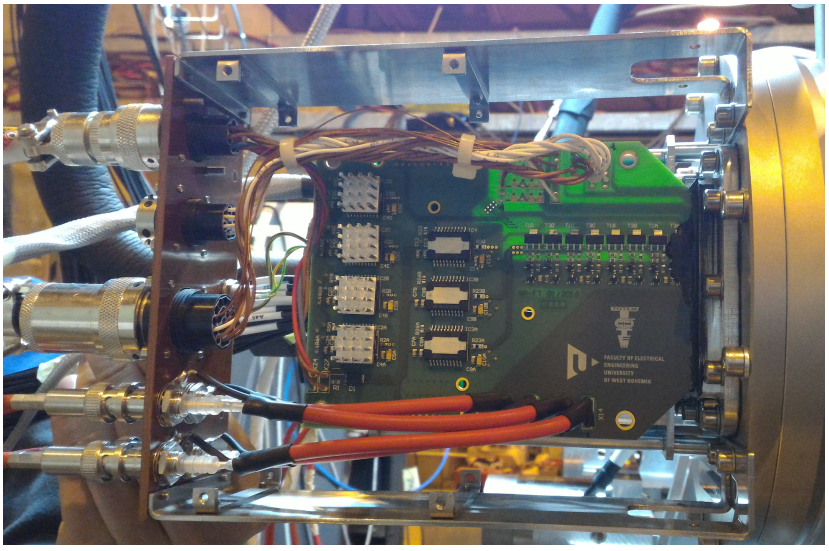

FIGURE 3.8: *Picture of the feedthrough board.*

The hybrid boards are installed in an aluminum structure to form a 4-layer package. The cooling capillaries are fixed outside this frame, under two copper wings, which are used to keep the package separated from the roman pot's cylinder as well as to dissipate the heat. At the same time, the contact between the pot and the wings ensures that the two system have the same ground reference.

The frame's bars are equipped with adjustable springs, to ensure that the detectors glued to the boards' do not stress mechanically the thin window 1.3.1 during the installation in the roman pot.

3.3 The NINO boards

As explained in section 2.4.1, the signals collected by the detectors cannot be analyzed using a sampler. The Collaboration decided to develop an electronic board to rapidly discriminate the analog signals and record their leading and trailing edges, in order to compute the particles' arrival time.

This board is named after the chip used for the discrimination: the NINO Asic. It is an 8 channel ultra-fast fixed threshold discriminator (as well as a low-power differential amplifier), originally designed for the time of flight system of the ALICE experiment [12]. The chip is composed of a first discriminator followed by four identical amplification stadiums after which the signals are sent to the Low Voltage Differential Signal (**LVDS**) output. The device jitter is about 25 ps.

The input stage (discriminator) is a common gate differential amplifier, charge-sensitive in a range of 0.01 - 2 pC and its threshold can be modified by changing the differential voltages applied to the respective pin, with a range of 10 - 100 fC. The most important feature for timing purposes is however the possibility to enlarge the width of the discriminated output using a constant W (which varies in the range 2 - 8 ns) proportional to the original input charge. The importance of this information, called time over threshold, has already been explained in section 2.19. Nevertheless, the width has to be processed again with the use of a pulse stretcher, in order to create signals wide enough to be digitized by the TDC. The chip's schematic is explained in fig. 3.9.

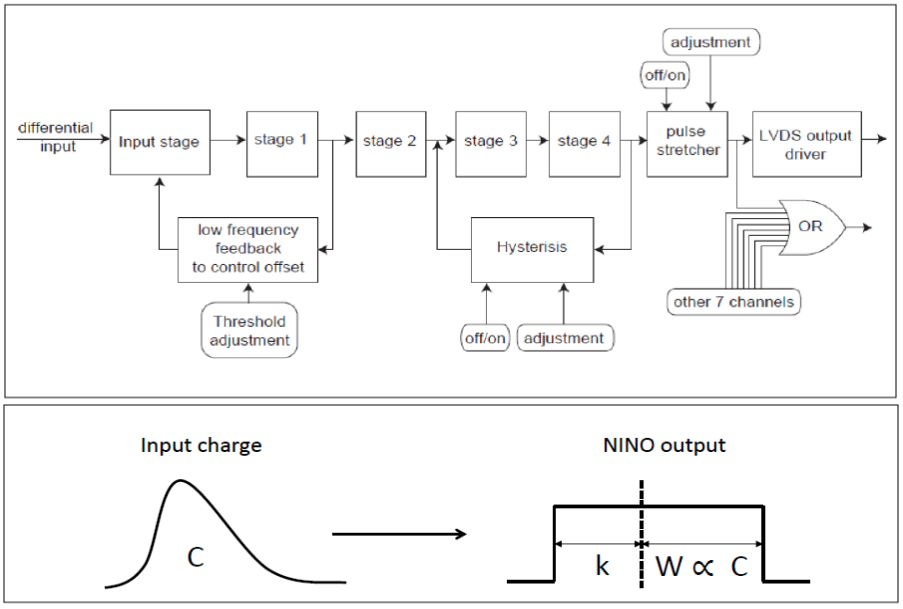

FIGURE 3.9: *Schematic of the NINO ASIC. On the bottom: the discriminated signals, after being processed by the intrinsic Time over threshold correction and the pulse stretcher [26].*

The NINO can also generate a global trigger signal applying the logic "OR" to all the outputs. Each board is equipped with 4 NINO chips, to discriminate the 32 signals, hence two boards for each package are required.

The NINO requires two values to be set to decide the threshold level. Its maximum level can be set manually operating a potentiometer, then using an I^2C controller we can decide the second value, that is subtracted from the level previously chosen. The tests done to calibrate them are explained in section 3.3.

Since the NINO chip works with differential inputs, the signal produced by the diamond detectors has to converted. The circuit designed to operate with the NINO standards handles negative single-ended signals and is shown in fig. 3.10.

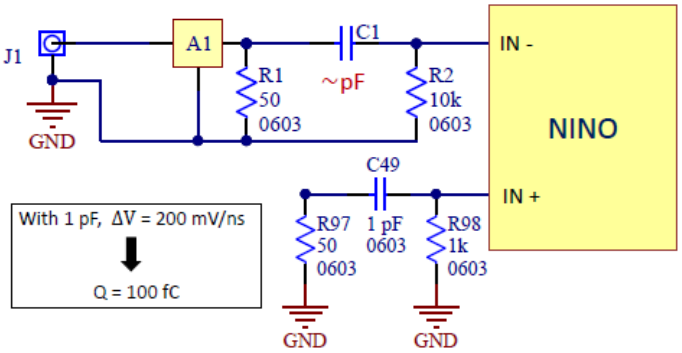

FIGURE 3.10: *The schematic block represents the circuit developed to operate the NINO with single-ended voltage signals [26]. The A1 component is the attenuator.*

Since the NINO is charge sensitive, choosing the right value for C1 3.10 is crucial to properly convert the voltage pulses in charge signals. The injected charge follows the relation:

$$Q = C \cdot \frac{\Delta V}{\Delta t} \cdot \tau \tag{3.1}$$

Where $\tau \approx 550$ ps is the circuit characteristic input time [26].

The input signal is first attenuated by A1 to avoid the use of a capacitance C1 too small (< 1 pF), which could cause the input parasitic capacitance to be dominant. In that case the amplifications of possible fluctuations would drastically affect the response from channel to channel. The 50 Ω resistor ensures that the NINO input are properly terminated.

In order to characterize the NINO response to an injected voltage signal, we used a waveform generator to simulate our detectors. Using this device we sent gaussian pulses with different amplitudes to the NINO, while, with an oscilloscope we monitored the NINO outputs width. The measurements have been performed using two different values for C1 (2.2 pF and 12 pF) and the results are plotted in graphs 3.11.

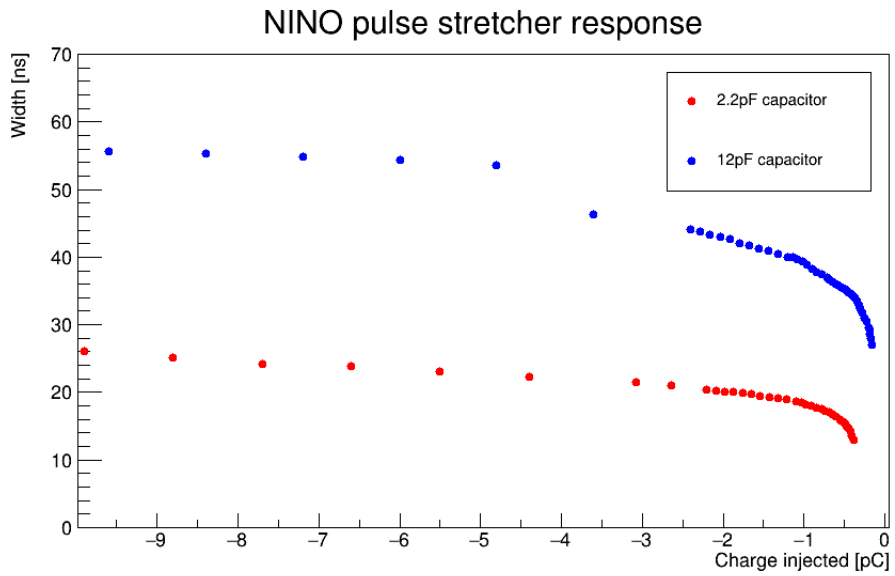

FIGURE 3.11: *Characterization of the NINO pulse stretcher response.*

The TDC chosen for CT-PPS was developed at CERN for high energy physics experiment and it is called HPTDC [34]. Its resolution varies with the number of channels used simultaneously, with a maximum of 32. In the high-resolution mode, used by CT-PPS boards, each HPTDC use 8 channel, therefore each NINO board is connected to 4 HPTDC chip.

Chapter 4

Tests on Diamond TOF detectors

This chapter will be dedicated to the tests performed on the CT-PPS TOF detectors, before and after installing them in the LHC.

Since the detectors timing performance had already been tested before the start of this thesis, I will mainly focus on some other technical aspects and issues we had to overcome before the installation, such as the noise removal or the trial to interface the hybrid boards with a TDC.

One of the crucial improvements we had to perform dealt with the discharge and sparks effects we discovered inside the detector packages. This problem led to a detailed study which fully occupies one of this chapter's sections.

4.1 The Test beam area

After being extracted from the SPS, some of the proton bunches are sent to the CERN North area, where they are used for fixed target experiment such as COMPASS, NA61/SHINE and NA62. However, as shown in 4.1, some of them are collided (T2 and T4) and the outgoing particles are deflected into the four beam lines that constitute the Test beam area.

The SPS (super proton synchrotron) test beam provides particle beams in the energy range from a few GeV/c up to $\sim$ 350 GeV/c. Upstream, bending dipoles allow the selection of the type, charge and energy of particles as well as beam intensity. Once selected, the particles cross a piece of vacuum beam pipe to enter the first experimental area where they move through the air, therefore drastically altering the beam dimension and intensity. However, every area is furnished with a Beam Position Monitor (**BPM**) (the BPM used are wire chamber detectors) which provides the X-Y beam's displacement from the detector center, as well as its dimensions.

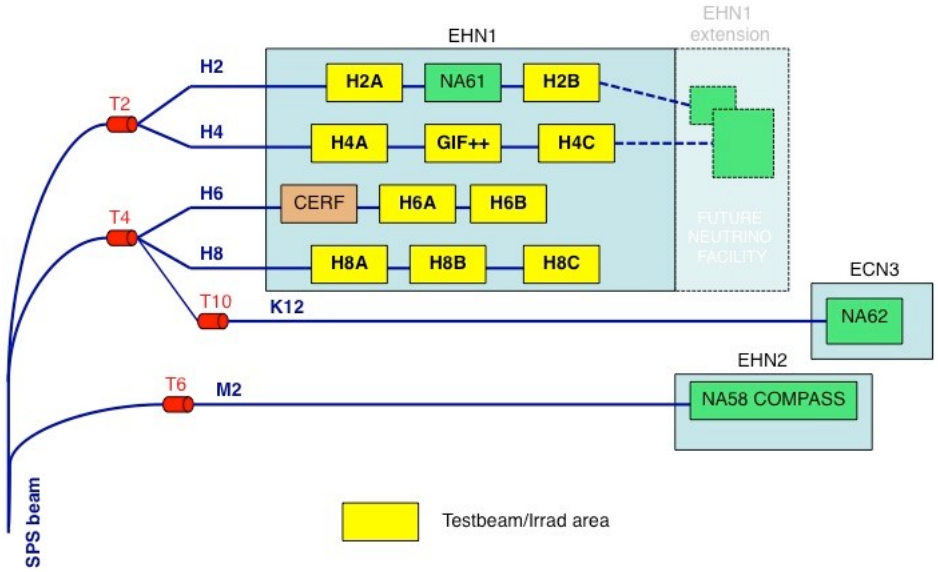

FIGURE 4.1: *The CERN north area exploits the 350 GeV/c protons extracted from the SPS accelerator making them collide in four different target, in order to produce secondary particles to be sent to the test beam area and to experiments situated in CERN Prevessin experimental area [1].*

All the zones are shielded by concrete block and are completely independent from each other. A security door locks the passage when the beam is on and, before unlocking, a control software ensures that the concrete beam dump is placed upstream, preventing particle passage. With the same software used to control the access and monitor the beams, it is also possible to change the current provided to some of the bending magnets in the line, modifying the particles' path.

The TOTEM and CT-PPS equipments are placed in the H8 line, precisely downstream, in the H8C zone. The spills are extracted from the T4 target; graph 4.2 shows the yield of particles production on the target. During this work all the tests were performed with a continuous 180 Gev/c Pion beam. The spills, $7{\cdot}10^7$ ($2{\cdot}10^8$) of 180 GeV/c $\pi^-(\pi^+)$ with a duration of 4.2 s, provided a measured rate of $\approx$ 1 KHz/mm^2 on the diamonds.

In the area, two remote controlled moving tables can be used to align the devices under test. One of them was occupied by a whole roman pot aluminum structure where two packages could be installed to perform cooling and vacuum tests. The structure before and after the detectors insertion is shown in fig. 4.3.

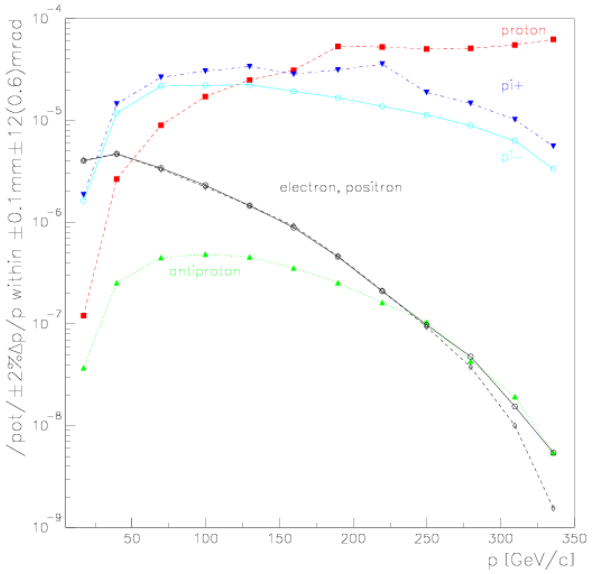

FIGURE 4.2: *Simulated spectrum of particle production on the T4 target [1]. Production rates are normalized per proton on target (pot) and the momentum acceptance is taken to be $\Delta p/p = 2\%$.*

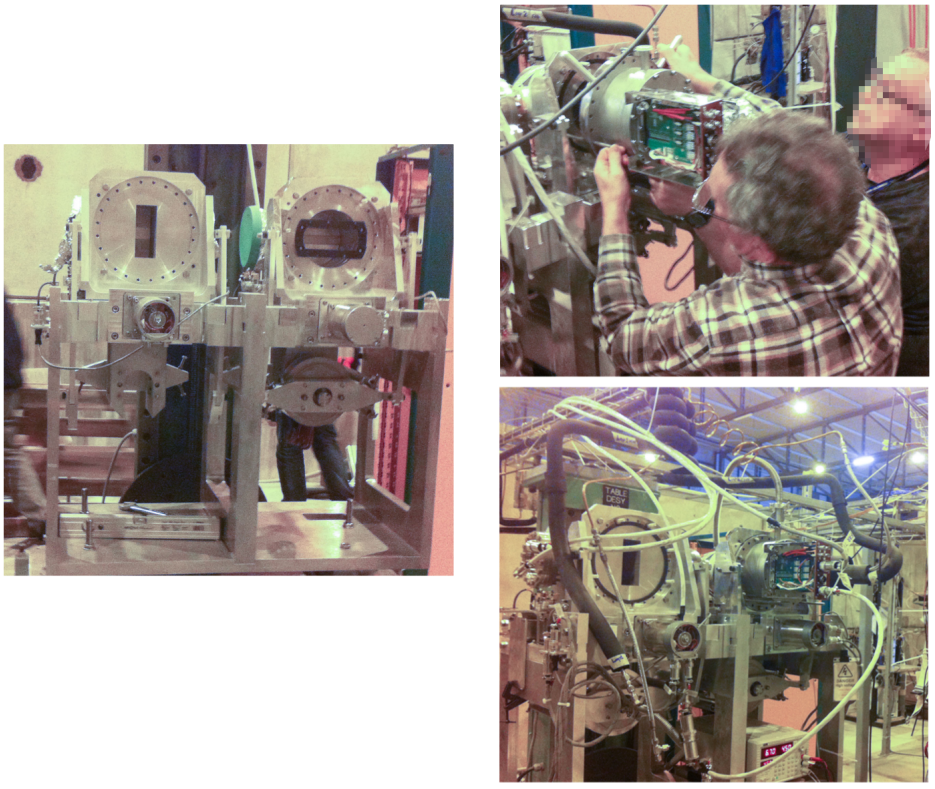

FIGURE 4.3: *On the left: roman pot structure at the North area. On the top and bottom right: a detector package is install to be tested with the cooling and vacuum systems on.*

The other table hosted the detectors placed on an external support, to be allow for an easy individual connection and alignment with the beam line, like shown in fig. 4.4. For the alignment of the detectors a cross-line laser was used, keeping the beam pipe and the wire chamber BPM as reference for the detectors' height and position.

FIGURE 4.4: *Mounting the external support on one of the H8C table. On the right: diamonds alignment on the beam line.*

A Micro Channel Plate (MCP) PLANACON 85011-5011 detector was aligned with the hybrid boards and used as a time reference. From previous measurements with a UFSD [17] the time precision of the MCP was confirmed to be 40 ps.

4.2 Tests with an oscilloscope

The TOF detectors characterization started with the signal analysis, collecting the waveform with an oscilloscope. We first checked every channel noise, comparing them with the expected values for the CT-PPS hybrid boards, described in section 3.1.

Once the oscilloscope thresholds were chosen and the Landau peaks distribution for MIP pions (using the oscilloscope modes) were observed, we started to acquire data files (using the same methodologies explained in section 2.4.1) and analyzed them to produce the plots for monitoring the detector performance. The results were compared with the ones previously obtained by the Collaboration during the R&D phase.

The graphs shown in fig. 4.5 were produced using the standard low voltage values for the amplifiers (ABA = 5 V, PreAmp = 2.1 V, Booster = 2.3 V) and a bias voltage of HV = 800 V. The pixel under study had a capacitance of $\approx$ 0.3 pF.

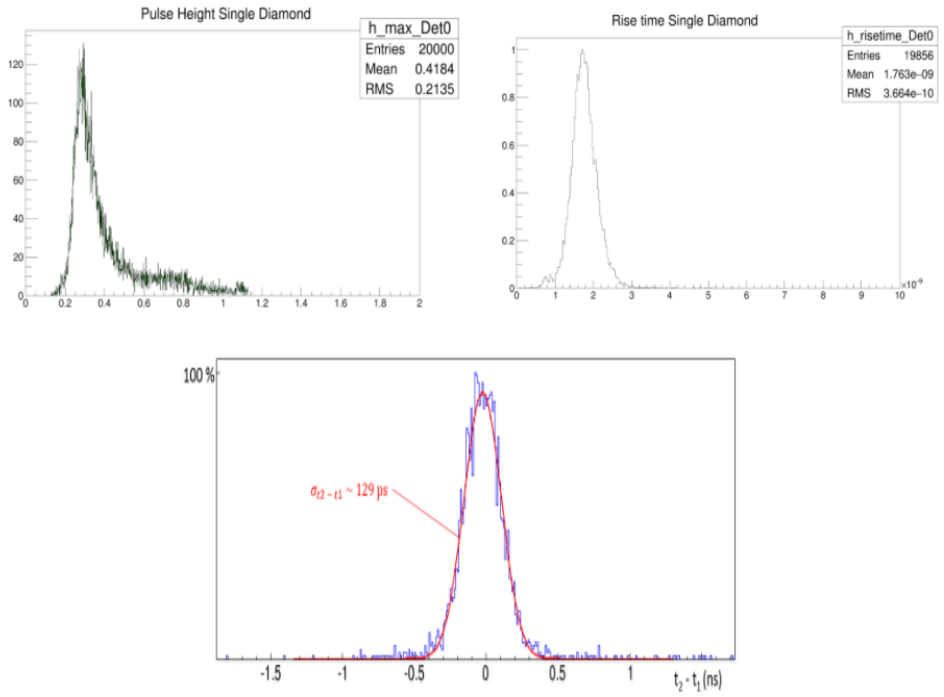

FIGURE 4.5: *Performance of a diamond timing detector (0.3 pF). In the top row the pulse height and rise time distribution are shown: the mean values are compatible with the expected one. The time precision (in the bottom) is taken to be the σ of the time arrival distribution, measured between two identical detectors: $\sigma_{t1} = \sqrt{\sigma_{tot}^2 - \sigma_{t2}^2} \approx 91$ ps.*

The time precision, measured using two identical diamonds detectors, can be extracted from the $\sigma_{(tot)}$ of the time arrival distribution:

$$\sigma_{(tot)} = \sqrt{(\sigma_{t1})^2 + (\sigma_{t2})^2} = \sqrt{2} \cdot \sigma_t \qquad \longrightarrow \qquad \sigma_t = \frac{\sigma_{(tot)}}{\sqrt{2}} \approx 91ps \tag{4.1}$$

which is compatible with the expected value.

4.2.1 Noise and signals oscillations

As already explained in the previous section, before starting to test the detectors timing precision, we had to monitor all the channels noise in order to verify their proper functioning. Powering the single detectors with the standard LV values (Pre = 2.1 V, Booster = 2.3 V, ABA = 5 V (3.1)) and plugging one channel at the time to the Agilent Infiniium DSO9254A Oscilloscope, we used its voltage RMS calculation feature to evaluate the noise levels.

However, since the boards are designed to get their ground reference exploiting the structure of the package to be inserted in the roman pots, obtaining a clean measurement was not trivial. The first plots, shown in fig. 4.6, was only used as comparison between the new and old generation (I'm referring to the boards tested in 2015 and installed in the vertical pots) of boards production.

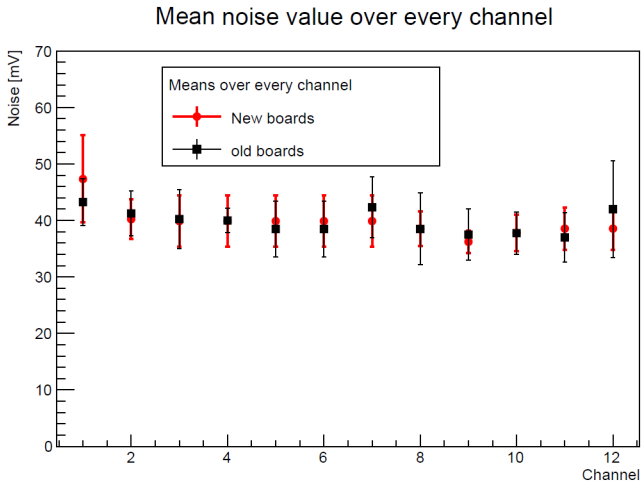

FIGURE 4.6: *The graph shows the trend of the noise v_{RMS} for the old and new generation of boards. From the error bars of the first and last channels, we can observe that these are generally the most problematic ones.*

Once all the noises were measured and the dead channels were fixed, we proceeded to assemble the packages, connecting all the cables that go from the hybrid boards to the boxes' flanges and feedthroughs. However, no clean v_{RMS} measurement could be performed.

As a matter of fact, powering up all the detectors together, we started to observe major oscillation in the diamonds' noise. Increasing the low voltage up to the standard values we triggered some periodical patterns with much greater amplitudes than the expected RMS noise ($\approx$ hundreds of mV).

Suspecting there might be an issue with the grounding system, we started to look for ground loops[1]. In the meanwhile, we started to screen the detectors to prevent possible external induction.

Since no significant improvement was achieved using these expedients, we came out with the idea that the detectors were inducing signals on the contiguous boards, cross-talking between the layers. Even dismantling the packages again and keeping the boards close to each other without connecting them to the same ground, we observed the same oscillations. Moreover, one of the detector packages presented

[1]Namely, when a signal got more than one path to flow to ground, which could produce some stray current in the conductor due to its connection to points at different potentials.

the same problem once introduced inside the roman pot mounted at the test beam area.

An empirical solution was reached screening the single detector layers:

- a metallic mask was screwed on the boards, in order to cover the amplification stadiums.
- every board was equipped with electromagnetic field suppressor sheets [2] on its back, commonly used for telecommunication purposes.
- we changed the boards' position, switching the first two layers back-to-back with the other two.

The three methods are shown in fig. 4.7.

However, the problem was not entirely solved yet and the collaborators from the University of West Bohemia,Pilsen (CZ)[3] are still at this moment testing the boards with a vector analyzer, in order to properly understand the problem and design a solution for the next prototypes.

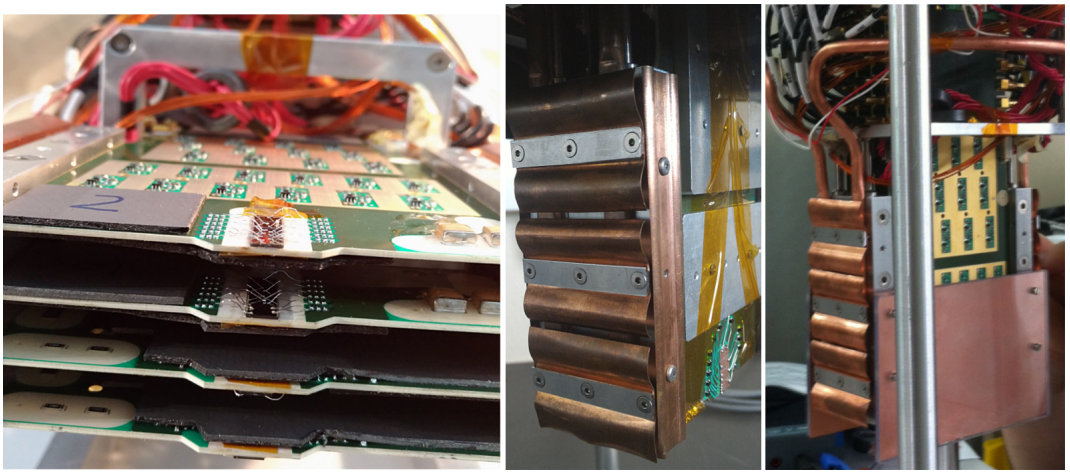

FIGURE 4.7: *In the picture: the three ideas implemented to remove the oscillations from the diamonds' signals.*

4.3 Tests with the CAEN TDC

In order to fully understand the functioning of the NINO discrimination chip as well as its efficiency, we tested it using a CAEN V775 32 Channel Multievent

[2] KEMET Electronics' Flex Suppressor sheets for EMI and RFI noise suppression, [6]
[3] https://www.zcu.cz/en/

TDC. The device boasts by a 12-bit resolution and fast clear time (600 ns); it accepts the NINO boards output differential flat connectors as inputs. A detailed description of the boards is given in section 3.3. In this case we worked with the CAEN TDC as a place holder of the HPTDC chip which is used in the CT-PPS standard front-end board.

Using both the oscilloscope and the TDC, we performed a relative efficiency measurement, comparing the number of events recorded by the two devices. fig. 4.8 shows the whole electronic chain used to fan-out the diamonds' signals and send them to the TDC using nuclear instrumentation modules (**NIM**).

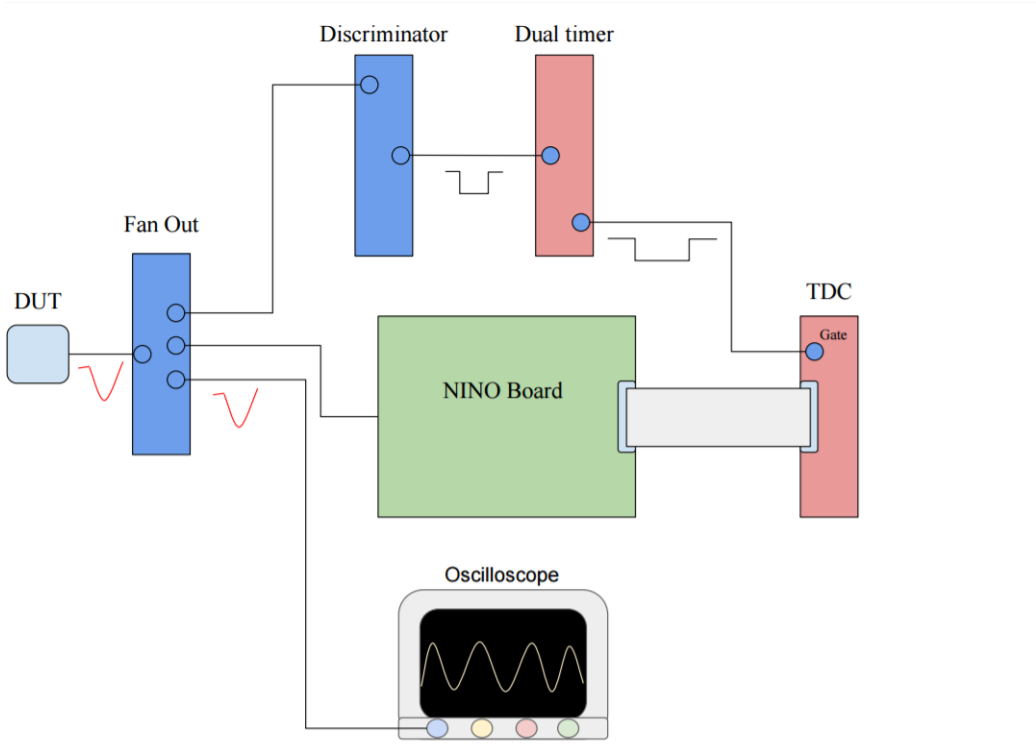

FIGURE 4.8: *Electronic chain used during the relative efficiency of diamond detectors, using a CAEN TDC.*

The diamonds' signals were sent to a Fan-out whose outputs were directed to the oscilloscope and NINO board. Another line was sent to a discriminator. After being discriminated, the logic pulse provided the starting signal for a timing unit, while another provided the stop. The two, connected together, generated a square pulse wide enough to be sent to the TDC as a trigger. Furthermore, the TDC read the NINO boards output and counted the events, reconstructing the leading and trailing edge couples. The software used in the reconstruction was provided by the CT-PPS group.

In order to prepare the boards to be installed inside the roman pots in the LHC beam line, we scanned all the NINO channels, finding some of them to be dead and

we proceeded to substitute those. Using the working channels and comparing the events counted by the TDC with the segments acquired with the oscilloscope we managed to get a clear picture of their relative efficiencies. An example is shown in fig. 4.9, which represent the tests performed on one of the NINO board, before it was modified and its chips fixed.

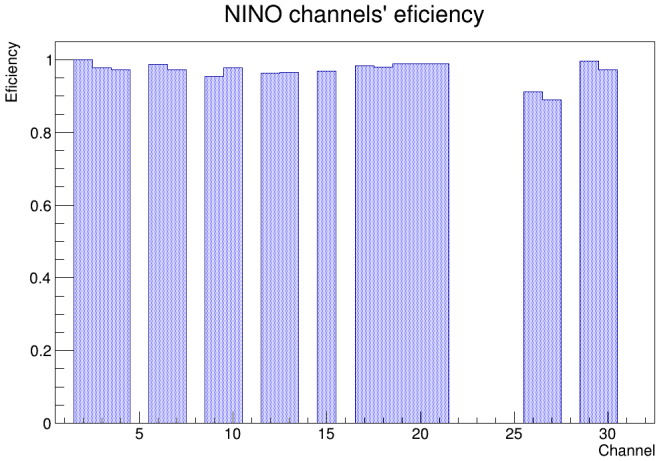

FIGURE 4.9: *Plot of the relative efficiencies of the NINO chips' channels. The blank spots represent the dead channels.*

Once new working NINO chips were bonded on the boards, we verified their functioning again, labeled and prepared them for the installation.

The connections between the two detector packages (one for each CT-PPS arm) and the boards' inputs were mapped to simplify the installation and the matching of the TDC channels with their respective diamonds' strips during the analysis. Table 4.1 shows the final mapping of the discrimination boards: the two detector packages' cable mapping on the NINO boards input. The first row indicates the channels' number; the second refers to the hybrids board channels, labeling them with a letter, to indicate the corresponding layer inside the package, and a number from 1 to 12. The red square represent the dead channels.

Detector Package 1

Nino 1	**1**	**2**	**3**	**4**	**5**	**6**	**7**	**8**	**9**	**10**	**11**	**12**	**13**	**14**	**15**	**16**	**17**	**18**	**19**	**20**	**21**	**22**	**23**	**24**	**25**	**26**	**27**	**28**	**29**	**30**	**31**	**32**
Boards Channel	D12	B12	C12	A1	B1	C1	A11		B11	C11	A2	B2	C2	A3	B3		C3	A10	B10	C10	A4	B4	C4		A9	B9	C9	A5	B5	C5	D8	
Cable# (A series)	37	21	29	4	12	38	14		20	30	2	16	34	3	17		33	7	10	31	10	24	26		6	18	32	9	23	27	45	

Detector Package 2

Nino 3	**1**	**2**	**3**	**4**	**5**	**6**	**7**	**8**	**9**	**10**	**11**	**12**	**13**	**14**	**15**	**16**	**17**	**18**	**19**	**20**	**21**	**22**	**23**	**24**	**25**	**26**	**27**	**28**	**29**	**30**	**31**	**32**
Board Channel	A12	B12	C12	A1	B1	C1	A11		B11	C11	A2	B2	C2	A3	B3		C3	A10	B10	C10	A4	B4	C4		A9	B9	C9	A5	B5	C5	D8	
Cable# (B series)	13	21	29	4	12	38	14		20	30	2	16	34	3	17		33	7	10	31	10	24	26		6	18	32	9	23	27	45	

TABLE 4.1: *Final mapping for the NINO boards installed in the LHC. The red squares indicates the board's dead channels.*

4.3.1 Threshold characterization

The NINO chips need a threshold level to work (3.3). These boards have four different manual potentiometer ($V_{th} \leq 3000$ mV), each one of them taking care of one chip. Additionally, an I^{2}C controller allows the setting of the second threshold value 3.3, to be subtracted from the one previously set.

In fig. 4.10 we can see a detail of the potentiometer on one of the board.

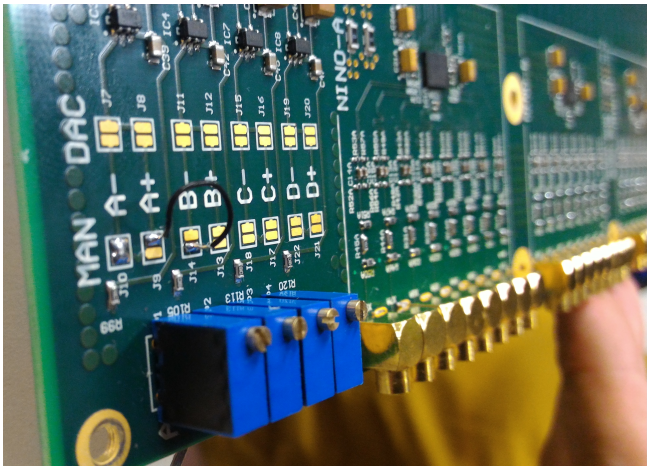

FIGURE 4.10: *Detail of one of the NINO board. In the bottom left we can observe the four potentiometers, one for each NINO chip.*

We scanned the voltages, changing the potentiometer's value and adjusting the threshold using a Python script developed to interface with the I^{2}C controller via a USB - I^{2}C connector. The proportionality between the DAQ steps and the V_{th} was known to be:

$$V_{th}[mV] = \frac{3000}{255} \cdot step_{DAQ} \tag{4.2}$$

The efficiency for each channel is plotted in graph 4.11.

4.4 The installation inside IP5

The installation was performed during one of the LHC technical stop and it took more than 50 hours. My job was to ensure the detector packages were operating correctly.

Once the packages were transported from the Test Beam area to the IP5 site, we accessed the tunnel to start the installation in the two CT-PPS arm, namely 4-5

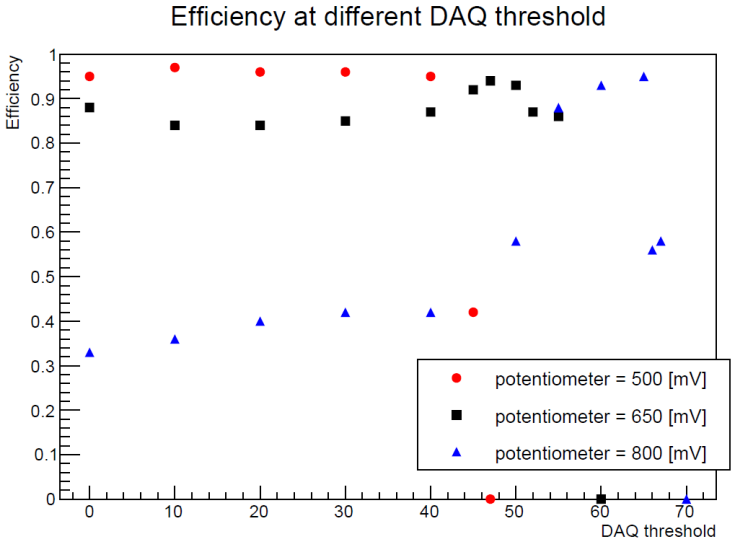

FIGURE 4.11: *Plot of the relative efficiencies of the NINO chips' channels.*

and 5-6 sectors (upstream and downstream with respect to CMS central barrel). The four layers of hybrid boards were then installed in the roman pot vessels and, after setting the correct pressure and temperature (detectors were cooled down to $\leq 40°$), we turned on the boards' amplifiers.

Even if the RMS noises were comparable with the ones already observed during the test beam (4.2), plugging the four layers of detectors, we ran into the same oscillations already detected during the package assemblage. This effect is described in section 4.2.1. Disconnecting one of the layers we achieved a lower time precision than expected, but we completely removed the noise oscillations affecting some of the diamonds' strips.

The pairs of NINO boards and digitizer boards were mounted on their support, kept well above the beam line to reduce the radiation dose collected from the read-out electronics. Once powered, we plugged the signal's cables to the NINO inputs following the mapping already discussed in section 4.3. The fully plugged NINO boards of the 5-6 section are shown in fig. 4.13. The NINO chips v_{th} were then characterized using the I^2C cable, connected to the laptop's USB input.

A bias test at high voltage was performed on the diamonds using the roman pots Detector Quality Control (**DQC**) system. The roman step motors were activated to ensure that the connections were not impeding the vessels movement.

Finally, the time available during the LHC technical stop was enough to properly install the detectors and monitor their correct functioning. The characterization of the low voltages values, the NINO thresholds and diamonds' v_{RMS} noise was performed on site.

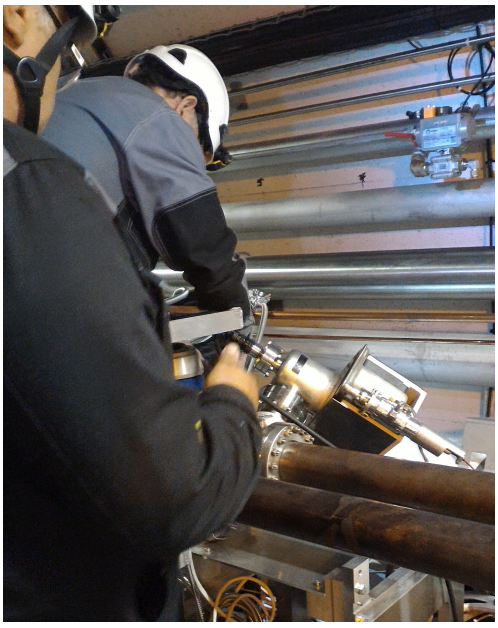

FIGURE 4.12: *Installing the packages in the CT-PPS horizontal roman pots, in the 4-5 sector.*

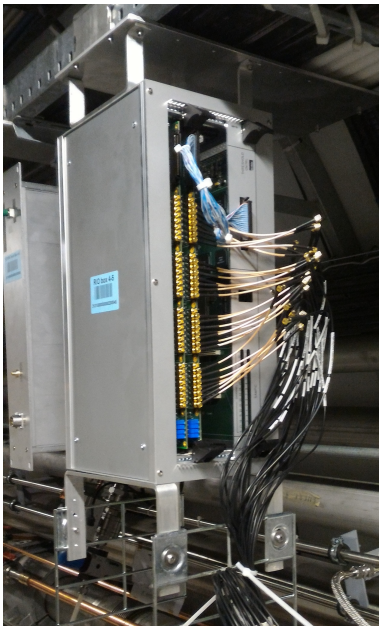

FIGURE 4.13: *The NINO boards of the 5-6 sector fully plugged.*

4.5 Tests after LHC

During the period May 2016 - January 2017 the detectors were kept in "garage position"[4] since no reconstruction firmware were completely developed yet. The

[4]Meaning the position in which the detectors are completely retracted and the sensors are out of the beam line, shielded by the roman pot vessel.

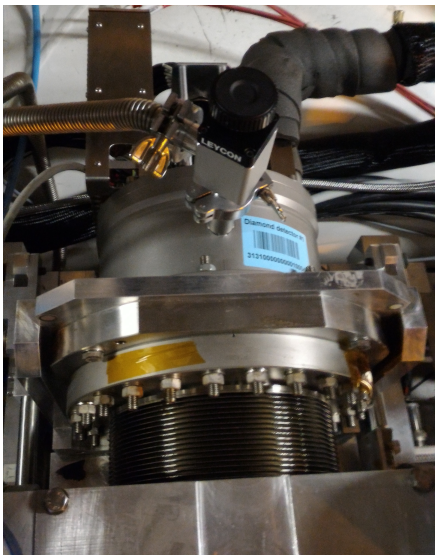

FIGURE 4.14: *Horizontal roman pots with the detector package installed. The vacuum bellow is plugged in and its valve can be observed in the middle of the picture.*

current absorbed from the diamond were monitored, trying to observe effects related to the high radiation rate.

After being extracted from the LHC, the detector packages needed some tests to fully understand some of the phenomenons observed with the DQM as well as to check if the diamond and electronic performance matched the ones before the installation.

4.5.1 Discharges effects

During the period inside the LHC, we had some issues in powering up the detectors with the standard CT-PPS timing diamonds ($\approx 700 \div 800$ V) bias voltage. Peaks in the absorbed current were detected, leading us to assume we were witnessing some discharge phenomenons on the hybrid boards or in the connections.

Once extracted from the roman pots, we started a detailed study in order to observe the high voltage weak spots, where the sparks would occur more likely. The RD51 group[5] contributed with their 8 KeV Cu X-ray gun set-up during the performing of the first tests. The nominal rate provided was $\approx$ MHz/mm^2.

The set-up, shown in fig. 4.15, consisted of the whole detectors package hermetically sealed inside a Plexiglas cylinder which functioned as a vacuum chamber. The set-up included a camera taking clear pictures through the transparent support.

[5] http://rd51-public.web.cern.ch/rd51-public/

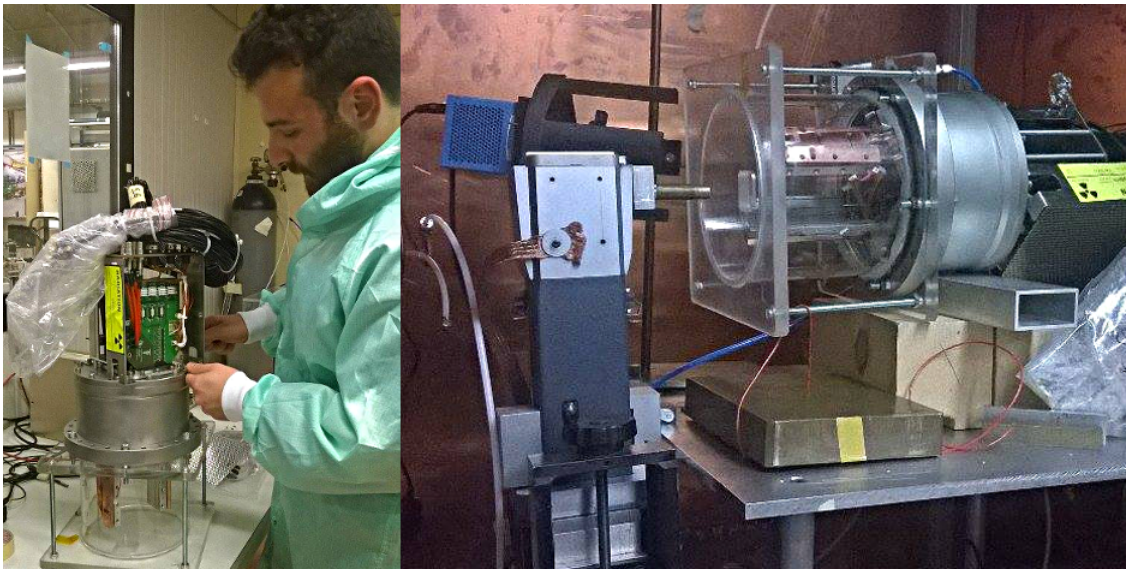

FIGURE 4.15: *On the left: assemblage of the support. On the right: set-up used during the tests at RD51.*

The idea behind the test was to ignite the sparks effect altering the vacuum inside the Plexiglass box and focusing the X-ray gun on different parts of the feed-through and hybrid boards.

The high voltages were provided with a Keithley 24100 SourceMeter. The Sourcemeter also monitored the absorbed currents. The communication with the PC was implemented with a GPIB connector (set-up already described in section 2.2.2) and the data were analyzed using the same C++ code as in the IRRAD tests, later described in this thesis (chapter 6).

During the first tests we studied the discharge effects on the hybrid boards, using a fully connected 4-layers package. As fig. 4.16 shows, the sparks seemed to be more frequent when firing the X-ray cannon at the bottom of the boards, where both the diamond sensors and the HV connections were placed. Moreover we found that the current values had an exponential dependence from the pressure and highly depends on the HV.

In the second part of the test we studied the two feedthroughs. The X-ray gun was focused on the HV connectors pad while we were performing a pressure and voltage scan. No effects were discovered before we reached the combination of 800 V and 40 mbar when, turning off and on the X-ray beam, we started to observe the current charging up ($\sim$ 100 nA) and consequently sparking. We observed that once ignited, these high currents persist with the X-ray beam Off.

Lowering the pressure to 20 mbar and the tension to 700 V, the discharges started to occur more frequently, resulting in an almost continuous series of sparks. fig. 4.17 shows the data collected and the pictures taken.

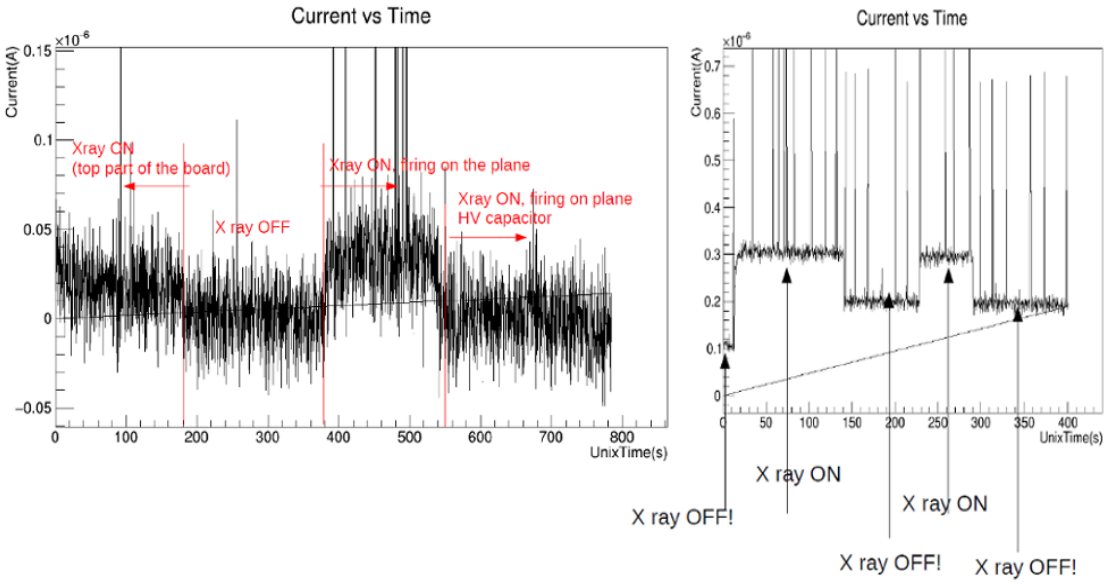

FIGURE 4.16: *On the left: data obtained with 600V and 25 mbar; the labels show where the X-ray gun were aiming. On the right: plot of the currents read at 650V and 15 mbar, aiming at the HV connector on the board.*

The weak spots discovered are shown in fig. 4.18.

After the RD51 tests, the detector packages were brought to the CMS buffer zone in order to be dismantled and checked piece by piece. Scanning the high voltage and inner pressure values, we spotted all the weak spots to be shielded from the sparks. All these areas, however, were already covered with a layer of conformal coating, selected to have the highest resistivity possible.

Studying the resistive material with a microscope, we discovered the layers to be non-homogeneous and therefore prone to accumulation of air and humidity which could explain the sparks detected. With the help of the University of Helsinki, Finland[6] we proceeded with the conformal coating removal to apply a new, more homogeneous, layer.

The steps we followed in this procedure are the sequent:

- we removed all the non-homogeneous conformal coating from the boards using a solvent.
- using an infrared lamp we heated up the hybrid boards, in order to remove the residual humidity on the PCB surface.
- in the meanwhile, a sample of the new liquid coating was placed in a vacuum in order to eliminate the air.

[6] https://www.helsinki.fi

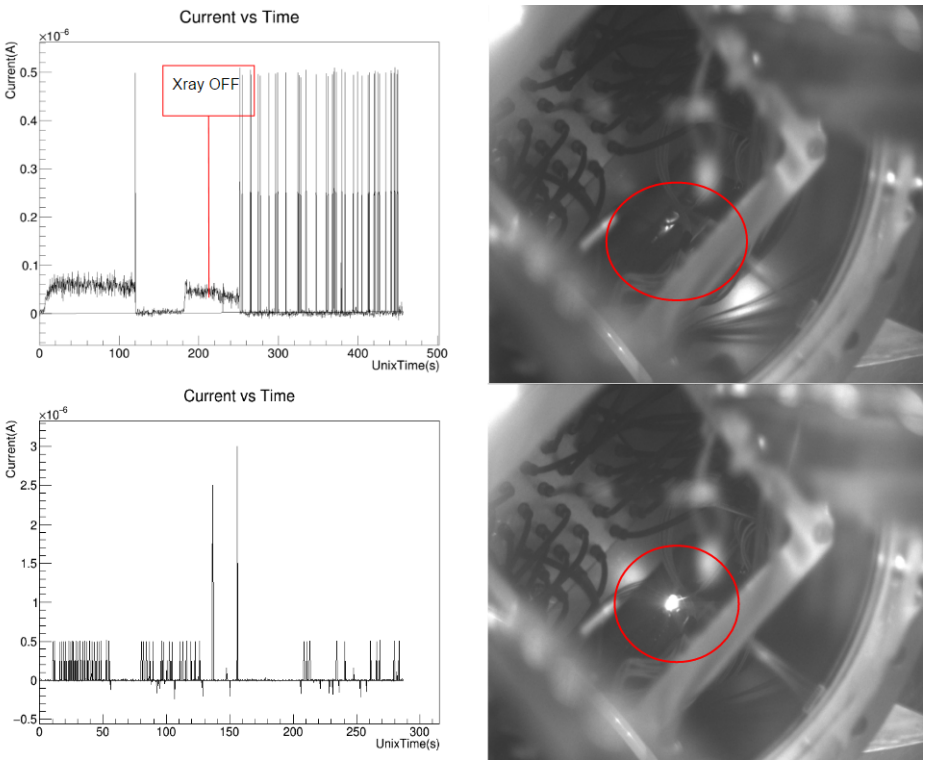

FIGURE 4.17: *On the upper row, on the left the plot the trend of the current studied at 800V and 40 mbar; it is possible to observe the effects of the charging up, generating the bumps and the consequent discharges. On the bottom row, the feedthrough has no time to charge up when we apply 700V and 20 mbar. Respectively on the top and bottom left, the pictures of the feedthrough.*

- a thin layer of new coating was applied on every weak spot.
- the boards were tested again.

In fig. 4.19 we can observe the bubbles found under the former layers of coating.

Some sparks were still occurring despite the new conformal coating. The University of Helsinki is trying to improve the deposing technique and solve this issue. Table 4.2 lists some of the effects observed during the tests performed inside CMS buffer zone, without the X-ray gun.

Feed-through	HV connector	not - coated	sparks @ 900V - 10 mbar
Hybrid board	HV connector	not - coated	sparks @ 850V - 30 mbar
Hybrid board	HV capacitance	coated	sparks @ 850V - 30 mbar

TABLE 4.2: *The table lists the information obtained scanning the pressure and voltages values during the tests performed in the CMS buffer zone. Unfortunately, the red box represents a spot in the board with the new coating applied which still presented sparks occurrence*

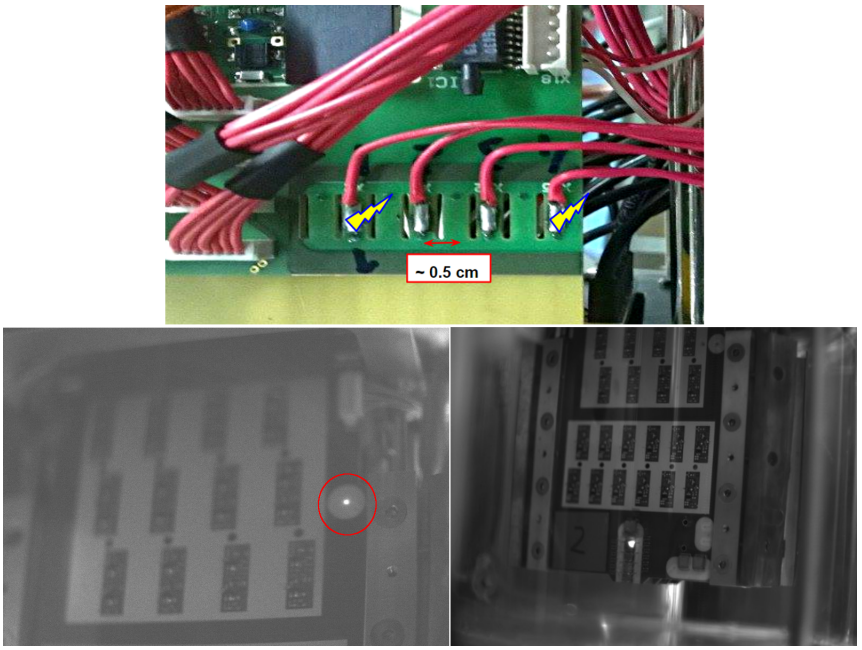

FIGURE 4.18: *In the picture the HV weak spots found during RD51 tests. In the top figure, the lightning symbols on the feedthrough represent the path of the sparks observed: from the HV pads to the ground's via on the pcb. The picture on the bottom shows two discharge effects: the first on the HV connector, the second in one of the HV pads, just under a diamond sensor.*

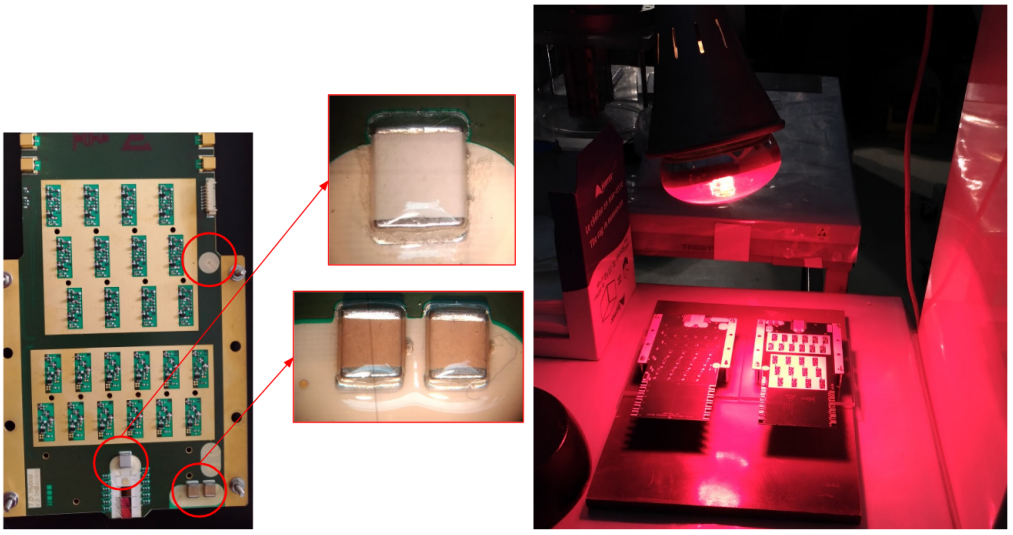

FIGURE 4.19: *The boards before the treatment (on the left) present air bubbles beneath the coating surface. On the right, the hybrids are heated to remove all the residual humidity.*

4.5.2 Noise measurement

The hybrid boards RMS noises were checked again after being extracted from the LHC. The radiation collected might have damaged the discrete electronic components, decreasing the SNR or even ruined some of the channels. Furthermore, during the extraction from the roman pots and the transportation, the boards might have been damaged. The set-up is shown in fig. 4.20).

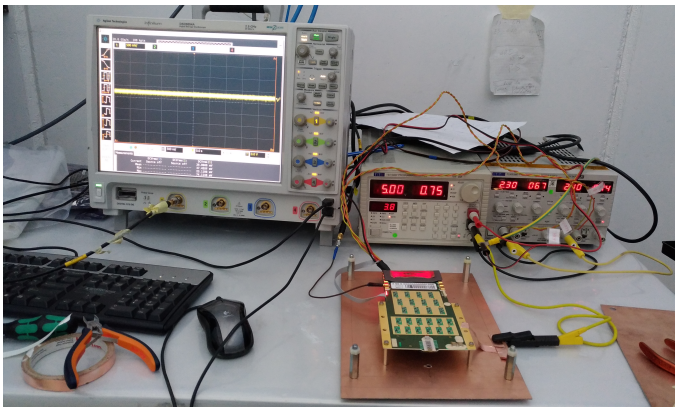

FIGURE 4.20: *Set-up for the noise measurement inside CMS buffer zone.*

fig. 4.21 shows the noise trend for all the boards checked, comparing the measurements performed before and after the LHC installation.

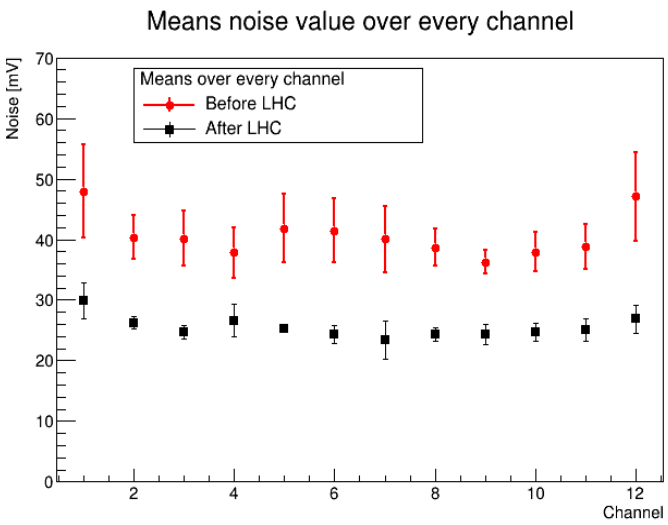

FIGURE 4.21: *RMS noise measured on the board extracted from the LHC.*

The noise values differences between the two plots are expected to be caused by the difference in the grounding system reference of the two set-ups.

Chapter 5

Double layer diamond detectors

Several double layer diamond detectors prototypes were tested before the one described in this thesis [23]. In 2004 H. Pernegger [53] designed a configuration which allowed the passage of charge particles through two layers of diamond sensors read out by the same amplification chain in order to enhance the charge collection on pcCVD detectors. Later also Benardzick [19] and Cardarelli [28] developed similar prototypes.

The same idea can be applied for timing purposes. Adding together signals collected by two different sensors it is possible to double the signal amplitude without increasing its rise time 5.1. Therefore this configuration maintains the benefits of a thicker detector, without any of the drawbacks of a longer carriers' drift time.

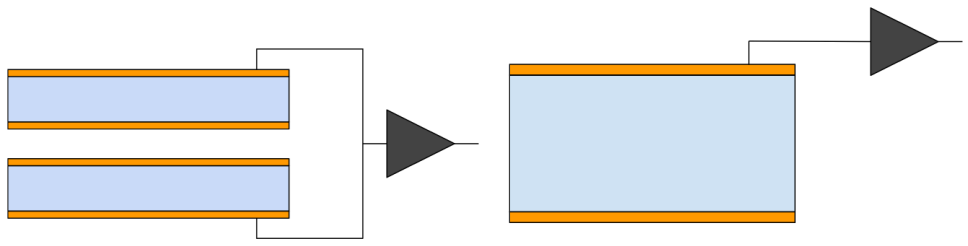

FIGURE 5.1: *Comparison between a double diamond layer configuration and a thicker sensor. Doubling the sensor's thickness we obtained twice the charge generation by incident particles. However a larger drift zone increases the signal's induction time and consequently rise time.*

As a matter of fact, it is worth noting that a thicker sensor would double the drift time of the charges created inside the diamond. Bonding more than one sensor in parallel to the same preamplifier should improve time precision by a factor greater than $\sqrt{N}$ which is the expected precision for n pixels independently read.

This configuration would reduce the number of detectors with a more compact structure, while using the same amount of sensors and improving their performance. Using less channels to read out, the heat dissipated from the package would drop as well.

In the next sections I will describe the R&D project granted by the INFN that led to timing performance tests on a double layer diamond detector, designed to employ the hybrid boards already used for the CT-PPS timing stations 1.6.

5.1 The prototypes

As already stated in the chapter's introduction, a multiple diamond layer configuration has been designed to enhance the timing performance of the already existing diamond detectors. Two 4.5 mm^2 and 500 μm thick scCVD 5-strips diamonds have been glued on the front and back of a spare CT-PPS hybrid board, ensuring the best alignment possible between the electrodes. A 4-strips detector was placed on the board's front, glued to the overhead HV pad, in order to provide a comparison between a single and a double layer detector. The 4-strips and 5-strips detectors' pixels used during the tests were selected to have similar capacitance 5.2.

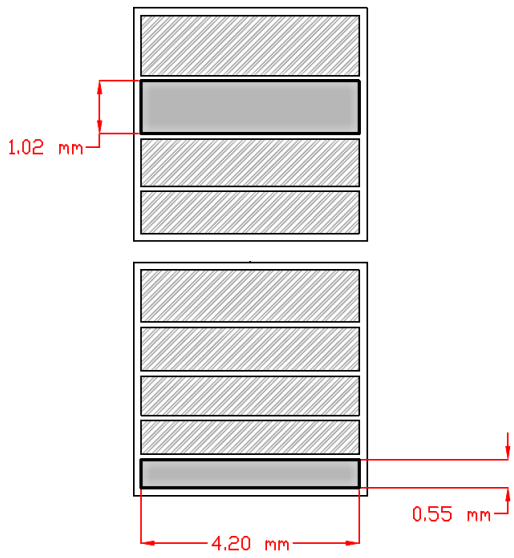

FIGURE 5.2: *Sketch of the configuration used in the double layer prototype. The highlighted strips are the ones used during the tests: the highlighted 4-strip (on the top) was chosen to have similar capacitance to the one used in the double diamond.*

Once glued, the smallest 5-strips diamonds pixels were connected to the same preAmp. The sensor in the front was bonded directly to the transistor input pin (3.1) and the wire attached to the diamond on the back had to pass through a via in the PCB (fig. 5.3).

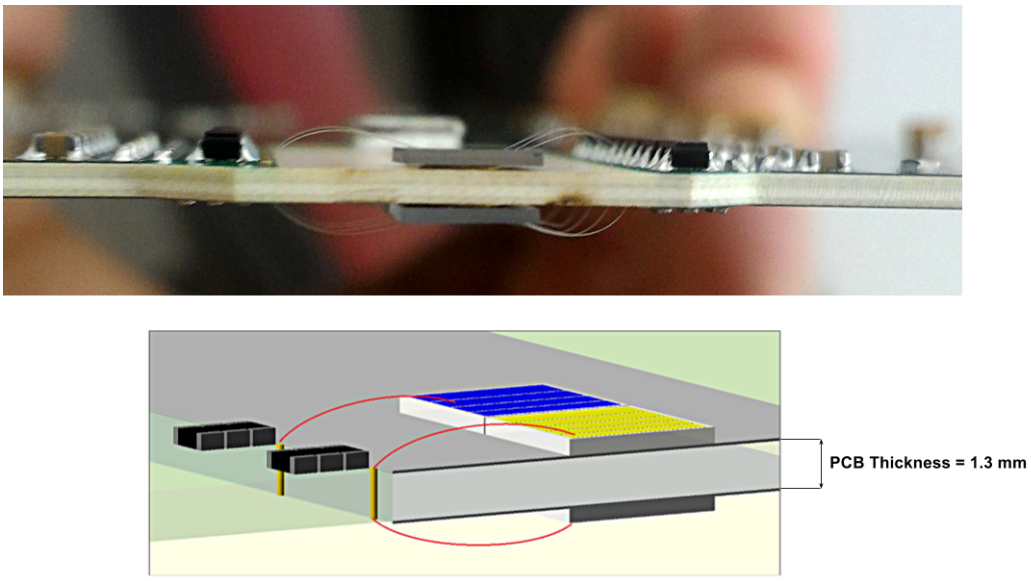

FIGURE 5.3: *In the top picture a cross section of the prototype is shown. In the bottom, a sketch of the PCB with the detector's layout. The diamond in blue is the 4-strips sensor used as a comparison.*

Bonding more than one diamond in parallel to the same pre-amplifier is made possible by the intrinsic characteristics of the sensor: due to its low dielectric constant 2.1, the dominant capacitance will be represented by the first amplification stadium input. As a result, the capacitance for a pixel with an area of 1 - 2 mm^2 is only $\sim$ 0.2 pF, while the input capacitance of the preAmp is about 0.4 pF 3.1.1, leading to a difference of about 10%.

As already stated in section 2.2.2, the typical dark current for a state of the art scCVD diamond don't rise beyond tens of pA. The noise introduced by the sensors will hence be negligible with respect to the electronic noise 3.1.

Several issues were considered during the tests:

- an incorrect mechanical alignment between the pixels could lead to a loss of time resolution with respect to the one predicted. Considering an alignment precision of 100 - 200 μm (in both X and Y directions), we expected to collect a fraction ($\sim$ 20%) of the signals generated from particles passing through only one of the two diamonds.

- the largest amplitude signals ($\sim$ 5%) brought to the saturation of the amplification chain and therefore they could not be used for the timing performance analysis.

- path differences in between the signals generated from back and front detectors could have led to an incoherent sum of the two peaks. However, since the via, which has to be crossed by the signals from the back diamond in order to be collected from the read-out, had a negligible impedance (being R = 2 mΩ and L = 0.3 nH), its resulting arrival time delay is also negligible. These effects have been studied with a numerical simulation, assuming a 1.3 mm path difference of the signals due to the board thickness, a permittivity of the board's material (Roger fiberglass) of 3.5 and a signal speed of $1.3 \cdot 10^8$ m/s. The resulting delay between the two signals is $\sim$ 10 ps, completely negligible with respect to the expected rise time ($\sim$ 1.7 ns as shown in section 4.2). The same conclusions were achieved supposing a wire bond length difference of 1 mm.

5.2 Test beam at the North Area

The first prototype was set up in the Prevessin North Area, described in section 4.1, to be tested with a 180 GeV/c Pion beam. The detector was mounted inside a mechanical support, placed in the H8c area and aligned with the beam line. After the alignment, the pion flux collected amounted to about 1 KHz/mm^2 per spill.

5.2.1 Set-up

The double layer detector, attached to an external support fixed to the moving table, was placed about a meter in front of the MCP detector whose performance are described in section 4.3, used as a time reference for the system. fig. 5.4 is a sketch of the set-up.

The board was powered using the same set-up already described in section 3.2. However, since they were not optimized to process such large signals (as the ones collected by the double diamond layout), the low voltage values used to power the amplifiers were lower than the one used with standard CT-PPS diamond detectors. The power supply used are reminded in the list below.

- **Low Voltages** $\Longrightarrow$ Aim-TTi TSX1820 Programmable 1 channel DC 21 Power Supply, PL30QMD-P Quad mode dual Power Supply.

- **High Voltages** $\Longrightarrow$ Keithley 2410 Source Meter

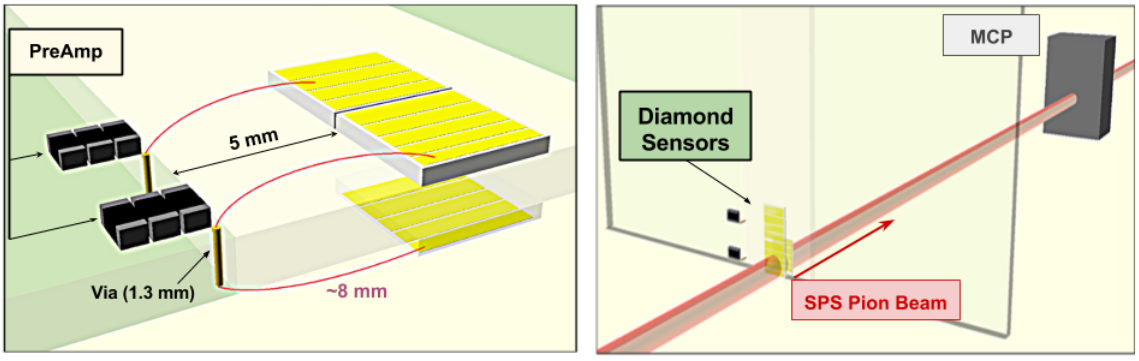

FIGURE 5.4: *Left: Sketch of the PCB board with the 4-strip single diamond and the 5-strip double one. The drawing includes the representation of the connections and the actual scale. Right: MCP diamonds board's arrangement in the test beam area. The SPS pion beam, drawn in red, cross the detector such that the particles hit the diamond connected through the via first . This expedient minimizes the collection's delay time.*

Only two of the twelve channels of the hybrid board were used. The Agilent DSO9254A oscilloscope (8 bits, 20 GSa/s) recorded the signals and monitored the MCP correct functioning. An off-line constant-fraction discriminator analysis 2.4.1 was used to process and analyze the time difference between the MCP and the diamond signal.

5.2.2 Measurement and results

Before staring to measure the timing performance, we checked the RMS noise of the V-amplitude. While the single diamond's channel (used for comparison) presented a v_{RMS} of about 24 mV, the double diamond's one was at $\sim$ 22 mV. Table 5.1 lists the RMS noise values for the two configurations. The channels mapping is shown in fig. 5.5.

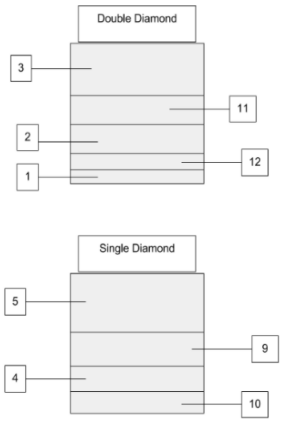

FIGURE 5.5: *Channels mapping for the two diamond sensors.*

Channel	Diamond	Noise [mV]
1	double	22
2	double	25
3	double	26
4	single	25
5	single	29
9	single	25
10	single	25
11	double	22
12	double	Broken channel

TABLE 5.1: *Table of the RMS noise voltage in the single and double layer configurations.*

This difference is compatible with the values already discussed in section 3.1.1 and is mainly due to the tolerances of the discrete components' value used in the amplification chain. The Fourier transforms of the single and double layer diamond detectors are compared in fig. 5.6.

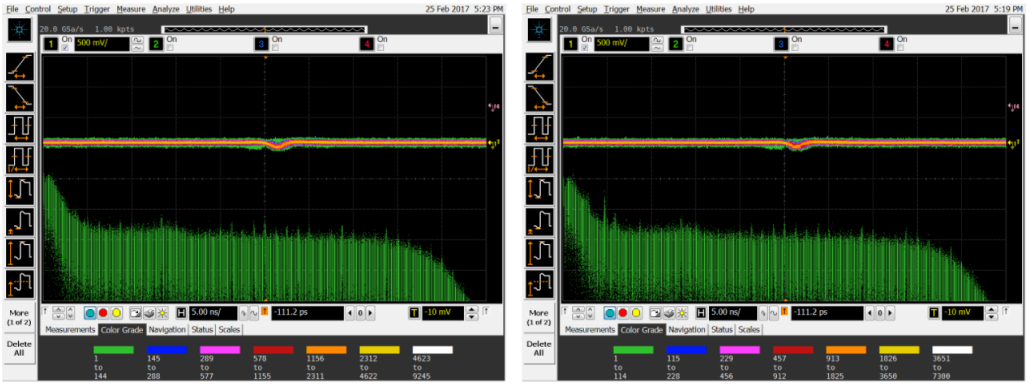

FIGURE 5.6: *Fourier transforms for the noise of the single (on the left) and double diamond (on the right) configurations, obtained using the Fast Fourier Transform (**FFT**) oscilloscope's feature.*

Plotting the pulse-height distributions, we can compare the two configurations' (single and double) response. As shown in fig. 5.7, the average values are 0.67 V for the single diamond and 1.03 V for the double.

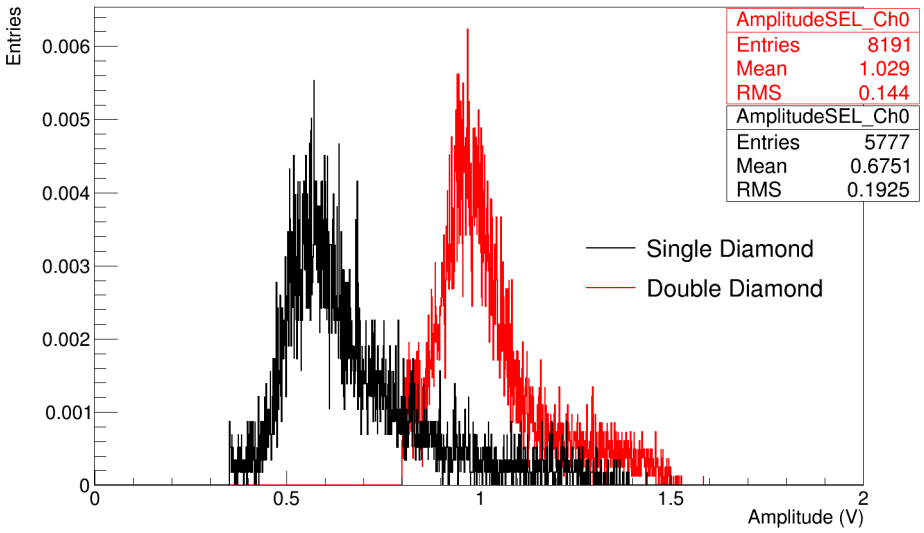

FIGURE 5.7: *Pulse height comparison: single and double diamond layout. The average values are 0.67 V for the single diamond and 1.03 for the double.*

With a quick calculation we can compute the Equivalent Noise Charge (**ENC**) for both the channels:

$$ENC = \frac{v_{noise}}{v_{signal}} \cdot n \left(\frac{C_{mip}}{e}\right) \tag{5.1}$$

Where:

- v_{noise} and v_{signal} are respectively the noise and signal amplitude expressed in volts.
- n is the number of sensors connected in parallel.
- C_{mip} is the charge generated by the passage of a MIP through the detector. As explained in section 2.2.3, this value is $C_{mip} \approx 2.9$ fC.
- e is the electron elementary charge $e \approx 1.6021 \times 10^{-19}$ C.

Using the measured values we find:

$$ENC_{single} = 650\, e^- \qquad ENC_{double} = 770\, e^- \tag{5.2}$$

Finally, we can analyze the time arrival differences' distribution between the double diamond and the MCP. Assuming an MCP time precision of $\approx$ 40 ps and computing the formula $\sigma_t(dd) = \sqrt{\sigma_t^2(tot) - \sigma_t^2(mcp)}$ using the $\sigma_t(tot)$ obtained from Plot 5.8.

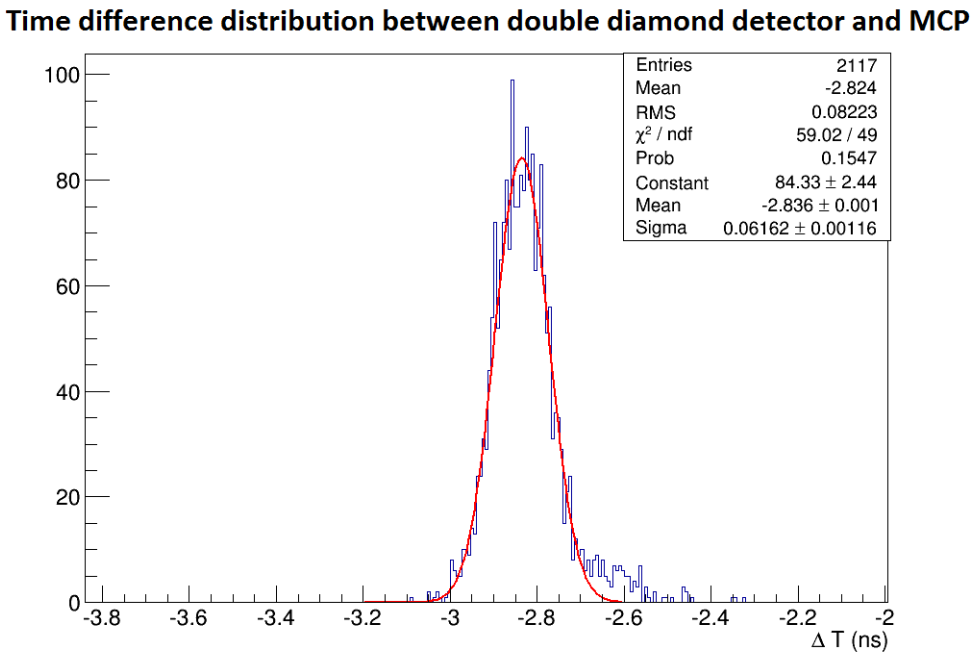

FIGURE 5.8: *Plot of the time difference measured between the MCP and the double diamond detector. The small non-Gaussian tail at larger ΔT values contains 5% of the events in the plot.*

We found the double diamond configuration to have a time precision of $\sigma_t(dd) <$ 50 ps, therefore an improvement of the time precision of about 1.6-1.7 is obtained with respect to the single diamond. Table 5.2 shows a comparisons between the values obtained with the two layouts.

	Single diamond	**Double Diamond**
Pulse Height [V]	0.67	1.03
Rise Time [ns]	1.7	1.5
Timing Precision [ps]	< 90	< 50

TABLE 5.2: *Table of comparison between the values measured in the single and double configuration.*

The tests showed a timing resolution not exactly doubled with respect to the one of single diamonds detectors. One of the reasons may be an imperfect alignment of the sensors on the two sides of the board. A more detailed study and further improvements on the manufacturing of the double diamond configuration are required. The results obtained show a considerable improvement in time resolution relative to the standard CT-PPS and TOTEM configurations.

Chapter 6

Radiation damage on diamond detectors

Several tests [18, 41] have been performed to study the effects of radiation damage on scCVD and pcCVD diamonds. As explained in section 2.1, high rate of incident charge particles could modify the crystals' structure, generating defects and imperfections in the lattice.

Two main issues were found during testing:

- ***increase of leakage currents***
  As explained in 2.2.2, the presence of a large (> 5 eV) band gap limits the diamonds' dark currents to negligible values ($\sim$ tens of pA) with respect to the signals' output (not considering the front-end electronics). However, dislocations of the lattice's atoms can generate new energy states in the forbidden band. Once thermally excited, the electrons (holes) in these levels can jump up to the conduction (valence) band, working as local currents generators.

- ***decrease of the signal amplitude***
  The production of trapping centers induced by radiation seems to be the most notable effect, resulting in a decrease of the carriers' lifetime and concurrently a decrease of charge collection distance.

Both effects lead to a drop of the SNR and of the charge collection efficiency. However, while the first phenomenon seems to cause permanent damage to the sensor, trap-defects are a reversible effect. Some empirical solutions have therefore been studied: the inversion and the increase of the detector's bias voltage seems to remove trap excess, restoring the signal amplitude.

In the next sections I will report the observation of the known effects and the study performed on a TOTEM - CT-PPS hybrid board inside IRRAD CERN facility.

6.1 IRRAD facility at CERN

After being extracted from the PS, some of the proton bunches with 24 GeV/c momentum are sent to the CERN East Hall, where two irradiation facilities share the area: IRRAD and CHARM 6.1. IRRAD facility provides CERN *users* with the possibility to schedule tests for material irradiation.

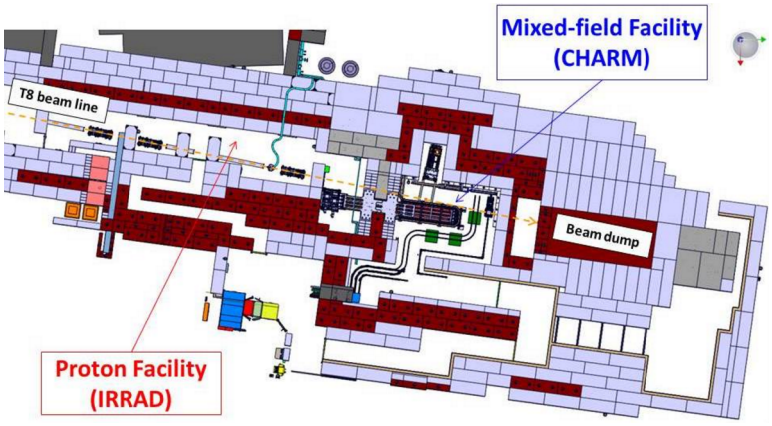

FIGURE 6.1: *IRRAD and CHARM facilities inside the Cern East Hall. The proton bunches are extracted from the PS and sent through the T8 beam line inside the area [8].*

The samples under investigation can be placed in three different areas divided by 80 cm thick concrete walls to reduce the background radiation. Sections of vacuum beam-pipes are installed to introduce the protons in the irradiation area, reducing the beam's interaction with air.

The beams' intensity depends on the number of spills for PS cycle (super-cycle) and it can reach a maximum proton population of 5×10^{11} protons/bunch. The optics configuration proprieties are listed in table 6.1:

Parameter	**Value**
Beam Energy [Gev/c]	24
Maximum # particles/beam per PS spill	$\sim 5 \times 10^{11}$
Spill's duration [ms]	~ 400
Maximum # of spills per super-cycle	6
Maximum # of particles per second	6.7×10^{10}
Super-cycle lenght [sec]	45.6
Maximum # of days per years	200

TABLE 6.1: *Details for the IRRAD runs.*

Depending on their size the samples can be installed on remote-control moving tables with movement precisions of ± 0.1 mm transversally relatively to the beam axis. This expedient allows the alignment between the object and the nearest

Beam Position Monitor (**BPM**) which provides the beam X-Y coordinates for every spill. Patch panels connect the irradiation area with the control room, keeping the whole read-out chain outside the controlled zone.

6.2 Test at IRRAD

The need to test the diamond detectors inside an irradiation facility was driven by the new luminosity reached by the LHC: even if table 6.2 shows that no significant effects were observed during the RD42 tests [18], the fluence[1] expected on the CT-PPS diamond timing detectors is much higher.

	A	B
Detector Area [cm^3]	0.42	0.62
Electrode Area [cm^3]	0.12	0.20
Detector thickness [μm]	260	430
Fluence [$\times$ 10^{13} pions cm^2]	1.3	4.3
Initial leakage current (nA at 100V)	< 0.01	< 0.01
Final leakage current (nA at 100V)	0.0014	< 0.01
Initial I_{ind} (nA at 100V)	72	110
Final I_{ind} (nA at 100V)	72	110

TABLE 6.2: *Results from RD42 tests performed on diamond detectors [18]. A and B are two different samples and are subjected to a different fluence. I_{ind} is the current monitored with a high impedance electrometer.*

As discussed in chapter 1.6, CT-PPS diamond detector will have to operate in high radiation condition. The rate foreseen by the simulation is $\sim$ tens of MHz on a single sensor and the energies of the CD non-dissociated protons to be detected are up to $\sim$ TeV. We decided to schedule a week of irradiation tests (2/11/16 - 9/11/16), using a 2-strips diamond glued to a TOTEM hybrid. Only one of the two electrodes were bonded to the pre-amplification stadium.

The board was fixed to a Plexiglas[2] support and mounted on the remote-controlled table inside Zone 2 of IRRAD facility [56]. An iron plate was placed on the hybrid's back, in correspondence of the diamond. It worked as a counting detector, reading the current generated by the passage of the particles and helping the alignment of the sensor to the nearest BPM. On the plate, a 5 mm^2 and 100 μm thick aluminum foil was used to record the dose absorbed by the detector. fig. 6.2 shows the preparation of the hybrid board, before the installation.

[1]Defined as the number dN of particles incident on a sphere of cross-sectional area da. For the rest of this thesis I will use it to indicate the number of particle n_{eq} passing through the surface of the diamond detector under test (4.5 mm $\times$ 4.5 mm).

[2]Non-metallic materials have to be preferred when building the supports in order to reduce the amount of active material after the irradiation. This expedient keeps the background radiation and the dose absorbed from the staff and the users as low as possible.

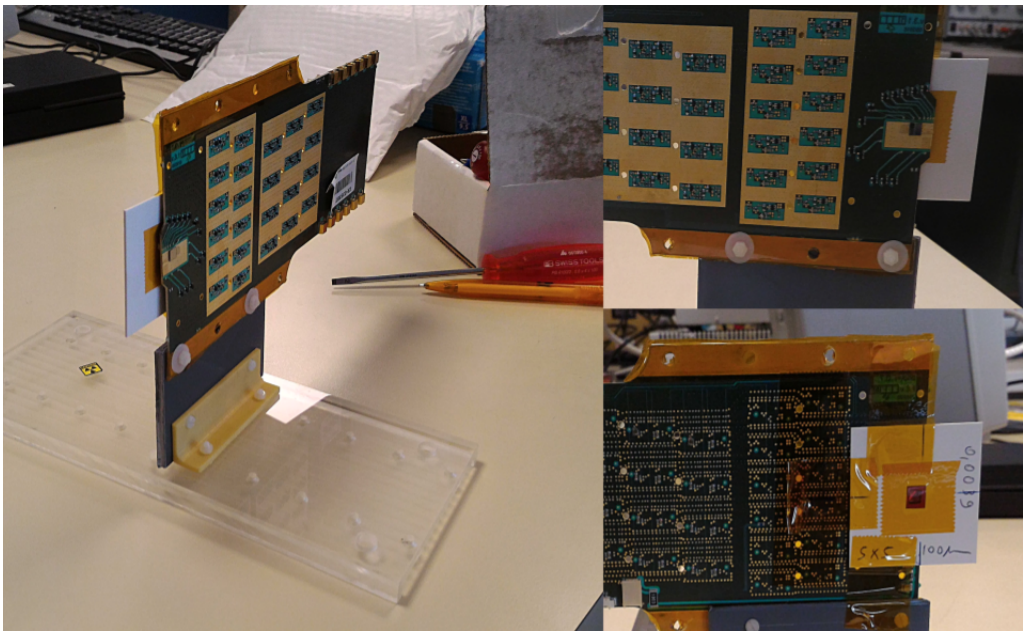

FIGURE 6.2: *Preparation of the hybrid before the installation on the moving support in IRRAD Zone 2. On the top right a detail of the board's front side; on the bottom right the picture shows the aluminum dose sensor.*

Both the signal cables and the power cables were connected to the patch panels inside the area and in the control room. A Keithley 24100 SourceMeter [5] provided the bias voltage and read the current absorbed from the diamond.
The Waveform analysis was performed with an Agilent Infiniium DSO9254A Oscilloscope. The set-up is shown in fig. 6.3.

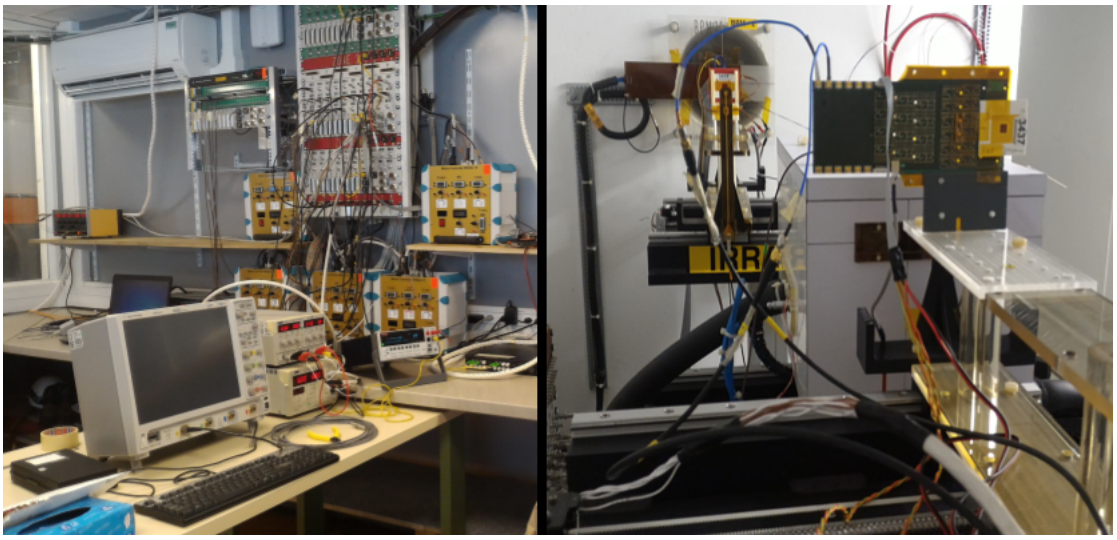

FIGURE 6.3: *On the left the set-up inside the control room. The power cables (two LV generators and the Keithley used for the HV) and the SMA connectors are plugged in the patch panel. On the right the detector is mounted on the moving support, inside the irradiation area.*

6.2.1 Acquisition of the currents

The Keithley 24100 SourceMeter had two purposes: ramp up the sensor's bias high voltage and read the absorbed current. We developed a C script to interface with the device via a pc through GPIB-to-USB connection. The currents' readings were stored in buffers and saved in text files. A C++ code with a ROOT framework decoded the input files headers and plotted the current-time graphs. Monitoring the currents' trend daily we discovered some interesting effects 6.4:

- A steep decrease ($\sim 1/3$ of $I_{initial}$) occurred during the first night, with the diamond absorbing a fluence higher than 10^{14} n_{eq}.
- A short run with reverse (negative) bias voltage was performed, to overcome possible issues related to the formations of electron-holes trap 6.
- No such variations were observed afterwards: the current values seemed to stabilize and reach a plateau.

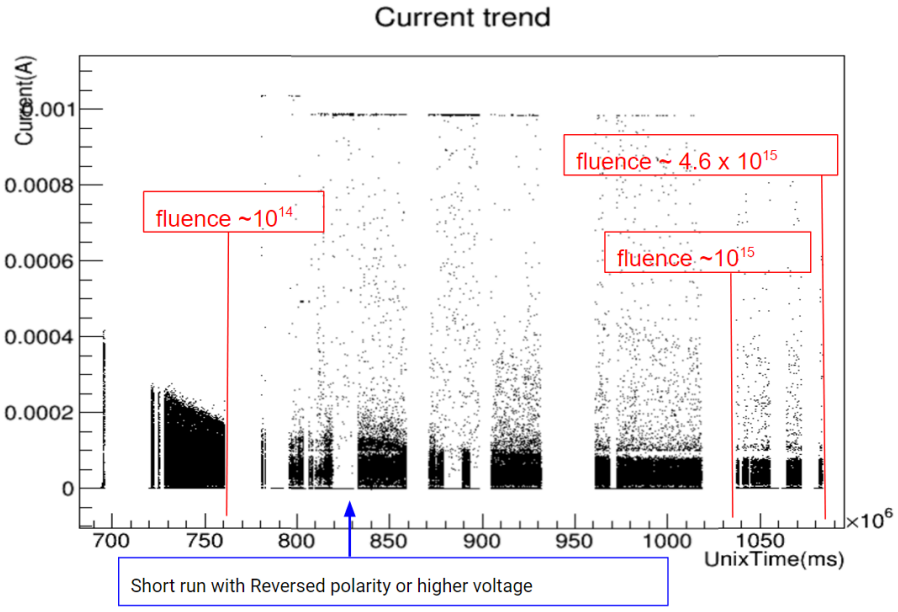

FIGURE 6.4: *The plot shows the trend of the current absorbed from the diamond during the irradiation tests. All the fluences are labeled in the graph. During the whole test, the bias voltage was kept to 500 V.*

During the next days the system responded to the IRRAD spills' passage with increasingly frequent *over currents* of the Keithley 24100 SourceMeter device. The value absorbed from the diamond started to reach the current limiter (1 mA) of the device. Comparing our data with the one collected from the nearest BPM 6.5, we observed that the machine spill intensities did not change during the week and the distribution of the amplitude remained approximately constant.

Zooming in two different zones of plot 6.5, we can study the spill profiles. fig. 6.6 shows the differences of the diamond's response between the end of the first day of data acquisition (fluence $< 10^{13}$ n_{eq}) and after an absorbed fluence of $> 10^{14}$ n_{eq}.

We can notice that zooming on an area where the Keithley 24100 SourceMeter reached the current limit, the signals were not following the spill profile anymore. We supposed them to be discharge effects due to the diamond *breakdown*.

Due to the high radiation background ($\sim$ 80 μSv/h after the area was closed for $\sim$ 6 h) and the absence of a trigger (which would have allowed us to perform the acquisition only during the spill's occurrence), no clean pulse height distribution could be acquired an more studies were necessary to observe possible SNR alterations. Moreover, more tests will have to be performed to discriminate between the damage sustained by the read-out electronics and by the diamond sensor itself.

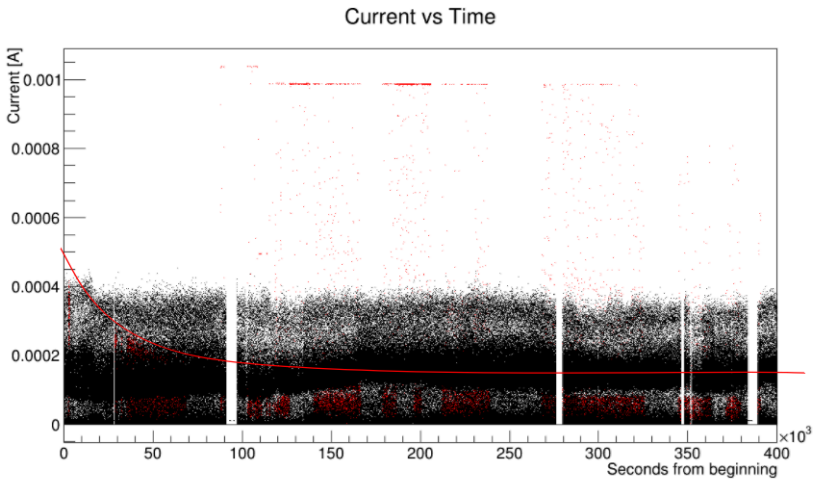

FIGURE 6.5: *Superimposition of the data collected from the diamond (in red) already shown in plot 6.4 and the BPM counts (in black). The IRRAD spill profiles are reconstructed using the derivative of the signal increase (integral) on the central pad of BPM2, units of measurement are therefore arbitrary. The red line helps to highlight the trend of the current absorbed by the diamond, already shown in picture 6.4.*

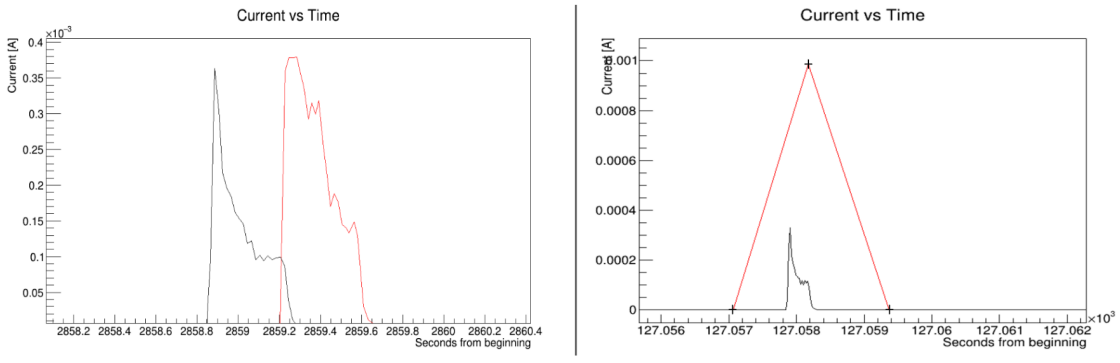

FIGURE 6.6: *Comparison between the spill profiles acquired during different days. The red line represents the current absorbed by the diamond, the black one the BPM counts.*

6.3 Test with a pion beam

After being subjected to a fluence of $\sim 4.6 \times 10^{15}$ n_{eq}, the detector under investigation was brought to the CERN north area to be tested on a "pure" Pion beam.

The high dose the hybrid board received caused the activation of the PCB metallic components. CERN Radio Protection certified the board to have a radiation

net value of: 360 μSv/h contact, 28 μSv/h at 10 cm, 2.5 μSv/h at 40 cm.. Once transferred to the Prevessin test beam area, powered and plugged to the oscilloscope, the channel bonded to the diamond presented a $\sim$ 100 Hz background caused by the PCB activation. We used the MCP detector 4.3 as a trigger and a time reference during the tests. Its 1$\times$1 cm^2 active area, covering the whole strip under analysis, was placed $\sim$ 1 m far from the diamond detector. Only two of the Agilent Infiniium DSO9254A Oscilloscope channels were used: the first one to analyze the diamond strip, the second to read the MCP signals.

In order to verify the amplification stages' proper functioning, the pulse height distributions were acquired with different values of low voltage, observing a correct displacement of the signal and noise peaks position 6.7.

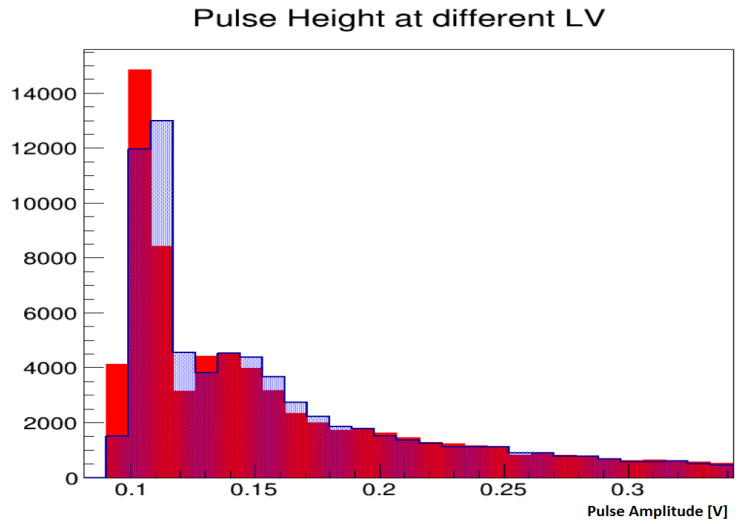

FIGURE 6.7: *Pulse height acquired using the H8 pion beam passing through the irradiated board. The two distributions are acquired with different low voltage values.*
Red : PreAmp = Booster = 2V ; Blue : PreAmp = 2.1 V, Booster = 2.3 V.

Using other samples previously acquired during the diamonds' timing performance tests, we compared the irradiated detector pulse amplitude distributions with the ones from a non-irradiated diamond. The plot obtained 6.8 shows a peak displacement from $\sim$ 0.53 V to $\sim$ 0.16 V, with a correspondent SNR drop from $\sim$ 35 to $\sim$ 10 (considering a typical electronic noise of $\sim$ 15 mV 3.1.1).

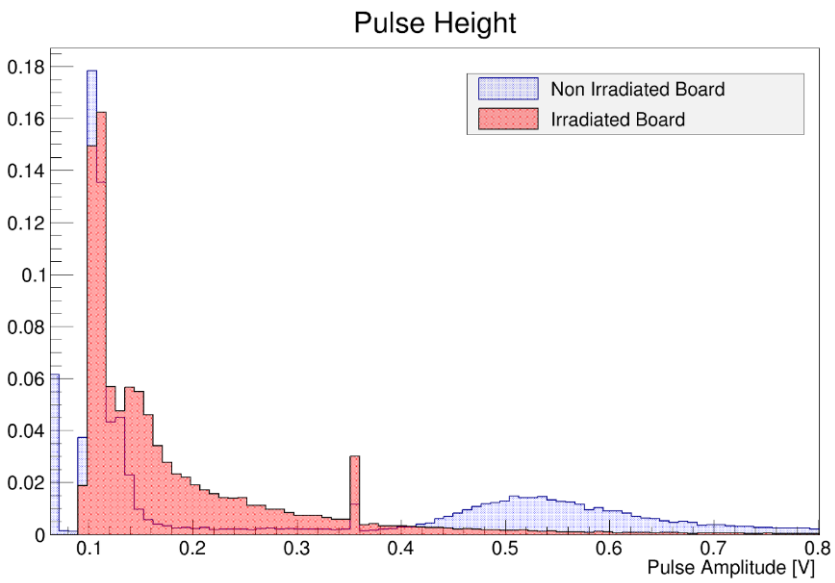

FIGURE 6.8: *Comparison between irradiated and non-irradiated diamond pulse amplitude distributions. Both the data sets were acquired with a bias high voltage of 500V and the same low voltage values.*

6.4 Test with a β^- source

The same pulse height measurements were performed again after 4 months (from November 2016 till February 2017) to work with lower radiation values on the board. The value updates on February 2017 were: 31 μSv/h contact, 2 μSv/h at 10 cm, 0.7 μSv/h at 40 cm, causing a radiation backgroud rate of $\sim$ 25 Hz. To obtain the most accurate comparison possible, we used a spare CT-PPS board to glue a brand new 2-strips diamond and bond the correspondent strips to a working channel.

Due to the LHC technical stop (scheduled from November 2016 till May 2017), no beams were available to test the detectors, and therefore we chose to use a Sr^{90} β^- radioactive source, already described in section 2.2.2. Using the source, the event rate increased from 25 Hz (due to the radiation background) to 2500 Hz and the signals' amplitude results to be comparable with the one of the peaks generated by the background radiation.

However the SNR of the irradiated diamond detectors resulted too low to outline the Landau curve of the pulse height distribution without the aid of an external reference. The measurement could be improved using a scintillator; nevertheless, the material budget of the PCB and diamond sensor (and a few cm of air) was too high for the β particles emitted by the Sr^{90} source to go through both

detectors. The measurements done using only the diamond detector and the radioactive source, shown in fig. 6.9, are therefore inconclusive and other tests on the irradiated board have to be performed using particles with larger momentum.

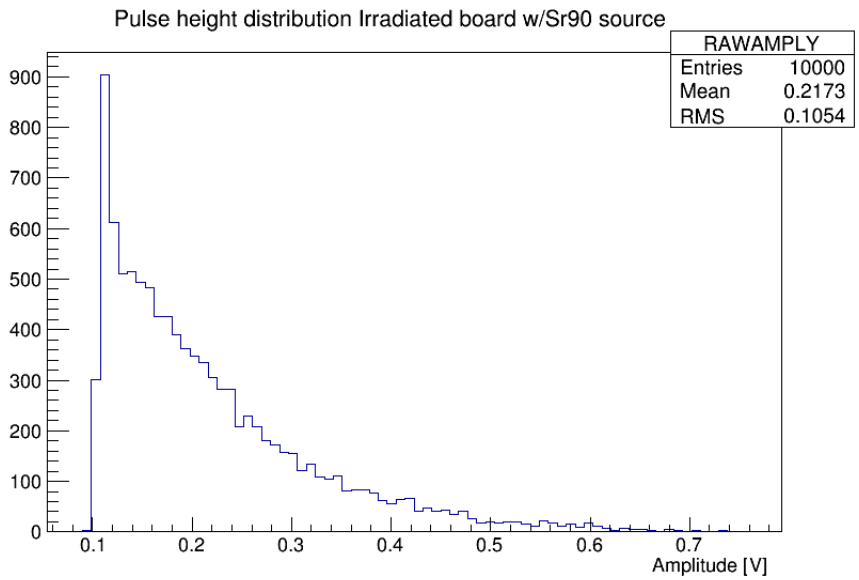

FIGURE 6.9: *Pulse height distribution acquired using the Sr^{90} source and the irradiated board. Due to the absence of a trigger system and the reduced SNR, the expected Landau distribution is not visible.*

$$\sigma_t = \frac{\sigma_{(tot)}}{\sqrt{2}} \approx 97\,ps \tag{6.1}$$

Bibliography

[1] Advanced european infrastructures for detectors at accelerators. https://aida2020.web.cern.ch/aida2020/node/272.html.

[2] Agilent ininiium 9000 series oscilloscopes. http://cp.literature.agilent.com/litweb/pdf/5990-3746EN.pdf.

[3] The CERN accelerator complex. https://cds.cern.ch/images/.

[4] Elementsix™. https://www.e6.com/en/Home.

[5] Keithley 24100 sourcemeter. http://www.tek.com/keithley-source-measure-units/keithley-smu-2400-series-sourcemeter.

[6] Kemet. https://www.digikey.com/en/product-highlight/k/kemet/flex-suppressor-sheets.

[7] Prism. http://www.princeton.edu/prism/.

[8] Ps-irrad proton facility. https://ps-irrad.web.cern.ch/ps-irrad.

[9] *The CMS muon project: Technical Design Report*. Technical Design Report CMS. CERN, Geneva, 1997.

[10] Addendum to the TOTEM TDR: Timing Measurements in the Vertical Roman Pots of the TOTEM Experiment LHCC document CERN-LHCC-2014-020 including questions/answers from/to the referees. Technical Report CERN-LHCC-2014-024. TOTEM-TDR-002-ADD-1, Nov 2014.

[11] Timing Measurements in the Vertical Roman Pots of the TOTEM Experiment. Technical Report CERN-LHCC-2014-020. TOTEM-TDR-002, Sep 2014.

[12] A. Akindinov, A. Alici, A. Agostinelli, P. Antonioli, S. Arcelli, M. Basile, F. Bellini, G. Cara Romeo, L. Cifarelli, F. Cindolo, M. Colocci, A. De Caro, D. De Gruttola, S. De Pasquale, K. Doroud, M. Fusco Girard, B. Guerzoni, D. Hatzifotiadou, D. W. Kim, J. S. Kim, S. Kiselev, S. C. Lee, D. Malkevich, A. Margotti, R. Nania, A. Nedosekin, F. Noferini, P. Pagano, A. Pesci, O. Pinazza, R. Preghenella, E. Scapparone, G. Scioli, K. Voloshin, M. C. S.

Williams, C. Zampolli, and A. Zichichi. Performance of the alice time-of-flight detector at the lhc. *The European Physical Journal Plus*, 128(4):44, 2013.

[13] M Albrow, M Arneodo, V Avati, J Baechler, N Cartiglia, M Deile, M Gallinaro, J Hollar, M Lo Vetere, K Oesterberg, N Turini, J Varela, D Wright, and Collaboration CMS-TOTEM. CMS-TOTEM Precision Proton Spectrometer. Technical Report CERN-LHCC-2014-021. TOTEM-TDR-003. CMS-TDR-13, Sep 2014.

[14] M G Albrow, Heejong Kim, S Los, M Mazzillo, E Ramberg, A Ronzhin, V Samoylenko, H Wenzel, and A Zatserklyaniy. Quartz cherenkov counters for fast timing: Quartic. *Journal of Instrumentation*, 7(10):P10027, 2012.

[15] G. Antchev, P. Aspell, I. Atanassov, V. Avati, J. Baechler, V. Berardi, M. Berretti, E. Bossini, U. Bottigli, M. Bozzo, P. Broulím, A. Buzzo, F.S. Cafagna, M.G. Catanesi, M. Csanád, T. Csörgő, M. Deile, F. De Leonardis, A. D'Orazio, M. Doubek, K. Eggert, V. Eremin, F. Ferro, A. Fiergolski, F. Garcia, V. Georgiev, S. Giani, L. Grzanka, C. Guaragnella, J. Hammerbauer, J. Heino, A. Karev, J. Kašpar, J. Kopal, V. Kundrát, S. Lami, G. Latino, R. Lauhakangas, R. Linhart, M.V. Lokajíček, L. Losurdo, M. Lo Vetere, F. Lucas Rodríguez, D. Lucsanyi, M. Macrí, A. Mercadante, N. Minafra, S. Minutoli, T. Naaranoja, F. Nemes, H. Niewiadomski, T. Novak, E. Oliveri, F. Oljemark, M. Oriunno, K. Österberg, P. Palazzi, L. Paločko, V. Passaro, Z. Peroutka, V. Petruzzelli, T. Politi, J. Procházka, F. Prudenzano, M. Quinto, E. Radermacher, E. Radicioni, F. Ravotti, E. Robutti, C. Royon, G. Ruggiero, H. Saarikko, A. Scribano, J. Smajek, W. Snoeys, J. Sziklai, C. Taylor, N. Turini, V. Vacek, J. Welti, P. Wyszkowski, and K. Zielinski. Diamond detectors for the TOTEM timing upgrade. *Journal of Instrumentation*, 12(03):P03007–P03007, mar 2017.

[16] G. Antchev, P. Aspell, I. Atanassov, V. Avati, J. Baechler, V. Berardi, M. Berretti, E. Bossini, U. Bottigli, M. Bozzo, P. Broulím, A. Buzzo, F.S. Cafagna, M.G. Catanesi, M. Csanád, T. Csörgő, M. Deile, F. De Leonardis, A. D'Orazio, M. Doubek, K. Eggert, V. Eremin, F. Ferro, A. Fiergolski, F. Garcia, V. Georgiev, S. Giani, L. Grzanka, C. Guaragnella, J. Hammerbauer, J. Heino, A. Karev, J. Kašpar, J. Kopal, V. Kundrát, S. Lami, G. Latino, R. Lauhakangas, R. Linhart, M.V. Lokajíček, L. Losurdo, M. Lo Vetere, F. Lucas Rodríguez, D. Lucsanyi, M. Macrí, A. Mercadante, N. Minafra, S. Minutoli, T. Naaranoja, F. Nemes, H. Niewiadomski, T. Novak, E. Oliveri, F. Oljemark, M. Oriunno, K. Österberg, P. Palazzi, L. Paločko, V. Passaro, Z. Peroutka, V. Petruzzelli, T. Politi, J. Procházka, F. Prudenzano, M. Quinto, E. Radermacher, E. Radicioni, F. Ravotti, E. Robutti, C. Royon, G. Ruggiero, H. Saarikko, A. Scribano, J. Smajek, W. Snoeys, J. Sziklai, C. Taylor, N. Turini, V. Vacek, J. Welti, P. Wyszkowski, and

K. Zielinski. Diamond detectors for the totem timing upgrade. *Journal of Instrumentation*, 12(03):P03007, 2017.

[17] R. Arcidiacono, M. Berretti, E. Bossini, M. Bozzo, N. Cartiglia, M. Ferrero, V. Georgiev, T. Isidori, R. Linhart, N. Minafra, M.M. Obertino, V. Sola, and N. Turini. Test of UFSD Silicon Detectors for the TOTEM Upgrade Project. Test of UFSD Silicon Detectors for the TOTEM Upgrade Project. Technical Report arXiv:1702.05180, Feb 2017.

[18] C. Bauer, I. Baumann, C. Colledani, J. Conway, P. Delpierre, F. Djama, W. Dulinski, A. Fallou, K.K. Gan, R.S. Gilmore, E. Grigoriev, G. Hallewell, S. Han, T. Hessing, K. Honscheid, J. Hrubec, D. Husson, R. James, H. Kagan, D. Kania, R. Kass, K.T. Knöpfle, M. Krammer, T.J. Llewellyn, P.F. Manfredi, D. Meier, L.S. Pan, H. Pernegger, M. Pernicka, V. Re, S. Roe, D. Roff, A. Rudge, M. Schaeffer, M. Schieber, S. Schnetzer, S. Somalwar, V. Speziali, R. Stone, R.J. Tapper, R. Tesarek, W. Trischuk, R. Turchetta, G.B. Thomson, R. Wagner, P. Weilhammer, C. White, H.J. Ziock, and M. Zoeller. Recent results from the rd42 diamond detector collaboration. *Nuclear Instruments and Methods in Physics Research Section A: Accelerators, Spectrometers, Detectors and Associated Equipment*, 383(1):64 – 74, 1996.

[19] P. Bednarczyk, E. Berdermann, J. Gerl, M. Gorska, I. Kojouharov, M. Pomorski, M. Rebisz, B. Voss, L. Acosta, R. Berjillos, I. Martel, M. A. G. Alvarez, J. M. Espino, J. L. Flores, I. Mukha, and R. Wolski. Application of Diamond Detectors in Tracking of Heavy Ion Slowed Down Radioactive Beams. *Acta Physica Polonica B*, 38:1293, April 2007.

[20] V. Berardi et al. TOTEM: Technical design report. Total cross section, elastic scattering and diffraction dissociation at the Large Hadron Collider at CERN. 2004.

[21] M Berretti. Performance studies of the Roman Pot timing detectors in the forward region of the IP5 at LHC. Aug 2014.

[22] M. Berretti, R. Arcidiacono, E. Bossini, M. Bozzo, N. Cartiglia, M. Ferrero, V. Georgiev, T. Isidori, R. Linhart, N. Minafra, M.M. Obertino, V. Sola, and N. Turini. Test of ultra fast silicon detectors for the totem upgrade project. *Journal of Instrumentation*, 12(03):P03024, 2017.

[23] M. Berretti, E. Bossini, M. Bozzo, V. Georgiev, T. Isidori, R. Linhart, N. Minafra, and N. Turini. Timing performance of a double layer diamond detector. *Journal of Instrumentation*, 12(03):P03026, 2017.

[24] Mirko Berretti. The diamond time of flight detector of the {TOTEM} experiment. *Nuclear Instruments and Methods in Physics Research Section A: Accelerators, Spectrometers, Detectors and Associated Equipment*, 845:29 – 32, 2017. Proceedings of the Vienna Conference on Instrumentation 2016.

[25] Mirko Berretti, Stefano Lami, and Angelo Scribano. *Measurement of the forward charged particle pseudorapidity density in pp collisions at $\sqrt{s} = 7$ TeV with the TOTEM experiment.* PhD thesis, Siena U., Sep 2012. Presented 27 Nov 2012.

[26] Edoardo Bossini and Nicola Turini. *Development of a Time Of Flight diamond detector and readout system for the TOTEM experiment at CERN.* PhD thesis, Siena U., Jun 2016. Presented 18 Jul 2016.

[27] Oliver Sim Brüning, Paul Collier, P Lebrun, Stephen Myers, Ranko Ostojic, John Poole, and Paul Proudlock. *LHC Design Report.* CERN Yellow Reports: Monographs. CERN, Geneva, 2004.

[28] R. Cardarelli, A. Di Ciaccio, and L. Paolozzi. Development of multi-layer crystal detector and related front end electronics. *Nuclear Instruments and Methods in Physics Research Section A: Accelerators, Spectrometers, Detectors and Associated Equipment*, 745:82 – 87, 2014.

[29] N Cartiglia, M Baselga, G Dellacasa, S Ely, V Fadeyev, Z Galloway, S Garbolino, F Marchetto, S Martoiu, G Mazza, J Ngo, M Obertino, C Parker, A Rivetti, D Shumacher, H F-W Sadrozinski, A Seiden, and A Zatserklyaniy. Performance of ultra-fast silicon detectors. *Journal of Instrumentation*, 9(02):C02001, 2014.

[30] Francesca Cenna, N. Cartiglia, M. Friedl, B. Kolbinger, H.F.-W. Sadrozinski, A. Seiden, Andriy Zatserklyaniy, and Anton Zatserklyaniy. Weightfield2: A fast simulator for silicon and diamond solid state detector. *Nuclear Instruments and Methods in Physics Research Section A: Accelerators, Spectrometers, Detectors and Associated Equipment*, 796:149 – 153, 2015. Proceedings of the 10th International Conference on Radiation Effects on Semiconductor Materials Detectors and Devices.

[31] M. Chaichian, P. Hoyer, K. Huitu, V.A. Khoze, and A.D. Pilkington. Searching for the triplet higgs sector via central exclusive production at the lhc. *Journal of High Energy Physics*, 2009(05):011, 2009.

[32] E. Chapon, C. Royon, and O. Kepka. Anomalous quartic W W gamma gamma, Z Z gamma gamma, and trilinear WW gamma couplings in two-photon processes at high luminosity at the LHC. *Phys. Rev.*, D81:074003, 2010.

[33] Serguei Chatrchyan et al. Study of exclusive two-photon production of W^+W^- in pp collisions at $\sqrt{s} = 7$ TeV and constraints on anomalous quartic gauge couplings. *JHEP*, 07:116, 2013.

[34] J Christiansen. HPTDC High Performance Time to Digital Converter. Technical report, CERN, Geneva, 2004. Version 2.2 for HPTDC version 1.3.

[35] P. D. B. Collins. *An Introduction to Regge Theory and High Energy Physics*. Cambridge Monographs on Mathematical Physics. Cambridge University Press, 1977.

[36] D.Luscănyi. Diamond detector development for the TOTEM experiment. Master's thesis, Budapest University of Technology and Economics, 2016.

[37] A Dominguez, D Abbaneo, K Arndt, N Bacchetta, A Ball, E Bartz, W Bertl, G M Bilei, G Bolla, H W K Cheung, M Chertok, S Costa, N Demaria, Daniel Dominguez Vazquez, K Ecklund, W Erdmann, K Gill, G Hall, K Harder, F Hartmann, R Horisberger, W Johns, H C Kaestli, K Klein, D Kotlinski, S Kwan, M Pesaresi, H Postema, T Rohe, C Schäfer, A Starodumov, S Streuli, A Tricomi, P Tropea, J Troska, F Vasey, and W Zeuner. CMS Technical Design Report for the Pixel Detector Upgrade. Technical Report CERN-LHCC-2012-016. CMS-TDR-11, Sep 2012. Additional contacts: Jeffrey Spalding, Fermilab, Jeffrey.Spalding@cern.ch Didier Contardo, Universite Claude Bernard-Lyon I, didier.claude.contardo@cern.ch.

[38] Oscar J. P. Eboli, M. C. Gonzalez-Garcia, S. M. Lietti, and S. F. Novaes. Anomalous quartic gauge boson couplings at hadron colliders. *Phys. Rev.*, D63:075008, 2001.

[39] Elif Ermis and C. Celiktas. Timing applications to improve the energy resolution of nai(tl) scintillation detectors. *International Journal of Instrumentation Science*, 1:54–62, 01 2013.

[40] Sylvain Fichet, Gero von Gersdorff, Bruno Lenzi, Christophe Royon, and Matthias Saimpert. Light-by-light scattering with intact protons at the LHC: from Standard Model to New Physics. *JHEP*, 02:165, 2015.

[41] V. Grilj, N. Skukan, M. Jakšić, W. Kada, and T. Kamiya. Irradiation of thin diamond detectors and radiation hardness tests using mev protons. *Nuclear Instruments and Methods in Physics Research Section B: Beam Interactions with Materials and Atoms*, 306:191 – 194, 2013. 13th International Conference on Microprobe Technology and Applications (ICNMTA2012).

[42] W. Herr, B. J. Holzer, and B. Muratori. 6.4 concept of luminosity: Datasheet from landolt-börnstein - group i elementary particles, nuclei and atoms · volume 21c: "accelerators and colliders" in springermaterials (http://dx.doi.org/10.1007/978-3-642-23053-0_9). Copyright 2013 Springer-Verlag Berlin Heidelberg.

[43] Jan Isberg, Johan Hammersberg, Erik Johansson, Tobias Wikström, Daniel J. Twitchen, Andrew J. Whitehead, Steven E. Coe, and Geoffrey A. Scarsbrook. High carrier mobility in single-crystal plasma-deposited diamond. *Science*, 297(5587):1670–1672, 2002.

[44] Sachie Kamakura, Naoki Sakamoto, Hidemi Ogawa, Hidetsugu Tsuchida, and Mitio Inokuti. Mean excitation energies for the stopping power of atoms and molecules evaluated from oscillator-strength spectra. *Journal of Applied Physics*, 100(6):064905, 2006.

[45] H.C. Kästli. Frontend electronics development for the {CMS} pixel detector upgrade. *Nuclear Instruments and Methods in Physics Research Section A: Accelerators, Spectrometers, Detectors and Associated Equipment*, 731:88 – 91, 2013. {PIXEL} 2012.

[46] W. R. Leo. *Techniques for Nuclear and Particle Physics Experiments: A How to Approach*. 1987.

[47] et al. M. Ciobanu. In-beam diamond start detectors. *EEE Trans. Nucl. Sci.*, 58(4), 2011.

[48] N. Minafra, H. Al Ghoul, R. Arcidiacono, N. Cartiglia, L. Forthomme, R. Mulargia, M. Obertino, and C. Royon. Test of ultra fast silicon detectors for picosecond time measurements with a new multipurpose read-out board. *Nuclear Instruments and Methods in Physics Research Section A: Accelerators, Spectrometers, Detectors and Associated Equipment*, pages –, 2017.

[49] Nicola Minafra, Francesco Saverio Cafagna, Emilio Radicioni, and Joachim Baechler. *Development of a timing detector for the TOTEM experiment at the LHC*. PhD thesis, U. Bari (main), Feb 2016. Presented 14 Mar 2016.

[50] K. A. Olive et al. Review of Particle Physics. *Chin. Phys.*, C38:090001, 2014.

[51] Eraldo Oliveri. *The forward inelastic telescope T2 for the TOTEM experiment at the LHC*. PhD thesis, Siena U., 2010.

[52] G. Pellegrini, M. Lozano, M. Ullan, R. Bates, C. Fleta, and D. Pennicard. First double-sided 3-D detectors fabricated at CNM-IMB. *Nucl. Instrum. Meth.*, A592:38–43, 2008.

[53] H. Pernegger. First test results of a high-speed beam conditions monitor for the atlas experiment. In *IEEE Symposium Conference Record Nuclear Science 2004.*, volume 4, pages 2248–2257 Vol. 4, Oct 2004.

[54] H. Pernegger. High mobility diamonds and particle detectors. *Physica Status Solidi Applied Research*, 203:3299–3314, October 2006.

[55] F. Ravera. The ct-pps tracking system with 3d pixel detectors. *Journal of Instrumentation*, 11(11):C11027, 2016.

[56] F. Ravotti, M. Glaser, and M. Moll. Upgrade scenarios for irradiation lines:: Upgrade of the Proton Irradiation Facility in the CERN PS EAST AREA. Sep 2014.

[57] Fabio Sauli. The gas electron multiplier (gem): Operating principles and applications. *Nuclear Instruments and Methods in Physics Research Section A: Accelerators, Spectrometers, Detectors and Associated Equipment*, 805:2 – 24, 2016. Special Issue in memory of Glenn F. Knoll.

[58] S. Schuwalow. Polarization effects in radiation damaged scCVD diamond detectors. 4th NoRDHia Workshop, Darmstadt (Germany), 9 Jun 2008 - 9 Jun 2008, Jun 2008.

[59] Wikipedia contributors. Constant fraction discriminator — Wikipedia, the free encyclopedia, 2020.

[60] A. Zoboli, M. Boscardin, L. Bosisio, G. F. Dalla Betta, C. Piemonte, S. Ronchin, and N. Zorzi. Double-sided, double-type-column 3-d detectors: Design, fabrication, and technology evaluation. *IEEE Transactions on Nuclear Science*, 55(5):2775–2784, Oct 2008.